Title
Dynamic response analysis of a 900 kW wind turbine subject to ground excitation

Author
Caudillo, Adrian Felix

Publication Date
2012

UNIVERSITY OF CALIFORNIA, SAN DIEGO

Dynamic Response Analysis of a 900 kW Wind Turbine Subject to Ground Excitation

A thesis submitted in partial satisfaction of the
requirements for the degree
Master of Science

in

Structural Engineering

by

Adrian Felix Caudillo

Committee in charge:

Professor Ahmed Elgamal, Chair
Professor J. Enrique Luco
Professor Chia-Ming Uang

2012

The thesis of Adrian Felix Caudillo is approved, and it is acceptable in quality and form for publication on microfilm and electronically:

Chair

University of California, San Diego

2012

DEDICATION

To my parents, who sacrificed so much for me to get here and whose love is ever present

EPIGRAPH

There is no struggle more futile than
the one that is not even attempted.
—Mexican Proverb

Know that much may happen here, . . .
trust in your training. Never doubt what
you have done. All your decisions have
brought you to this point. Now, perhaps,
they shall see what you have become.
—Kreia

TABLE OF CONTENTS

LIST OF FIGURES

LIST OF TABLES

ACKNOWLEDGEMENTS

The contributions of Dr. Ian Prowell were invaluable in the production of this thesis. In addition to his primary efforts in the employed experimentation data, his previous research in the field served as both a solid foundation and launching point to the results of this study. On a more personal level, he also provided the author with an introduction into the field and supplied practical advice in many areas related to this thesis.

Professor J. Enrique Luco should rightfully be credited for the initial consulting about the theoretical subject matter found in Chapter 5, especially regarding the approach involving transfer functions and mesh refinement as it applies to soil-structure interaction problems. Concerning the results found in Chapter 5, a glaring oversight would be made if proper credit were not awarded to Dr. Jinchi Lu. Indeed, the BridgePBEE graphical user interface is his creation, utilizing the OpenSees engine to facilitate the dynamic analysis and simulation of bridge-like structures. He has graciously provided a modified version of the software, adapted for the wind turbine model simulation that was employed in this thesis. Without his efforts, this chapter would not have been possible.

The partial financial support to the author provided by the National Science Foundation (NSF) is gratefully acknowledged (NSF NEESR-II grant No. CMMI 0830422). The experimental work employed in this thesis was conducted with contributions in the form of making the testing site available, guidance, and man-hours from Oak Creek Energy Systems (Hal Romanowitz, J. Edward Duggan, Vaughn Johnson, Michael Burns, and many others)r. Finally, all the related data acquisition phases were supervised by Dr. Robert Nigbor of UCLA with the hard work of the NEES@UCLA team (Ben Ferrero, Steve Kang, Steve Keowen, and Alberto Salamanca).

ABSTRACT OF THE THESIS

Dynamic Response Analysis of a 900 kW Wind Turbine Subject to Ground Excitation

by

Adrian Felix Caudillo

Master of Science in Structural Engineering

University of California, San Diego, 2012

Professor Ahmed Elgamal, Chair

This thesis exhibits the results of a study focused on the seismic behavior of a 900 kW wind turbine. As of the time of this writing, special engineering provisions for such loading events are not adequately defined.

In order to accomplish the research objective, the author relies on available experimental data taken in 2009 from accelerometers attached to a wind turbine base and tower along with an eccentric mass shaker placed on the turbine foundation. On this basis, the dynamic properties of the wind turbine, including tower bending modes and natural frequencies were extracted. An attempt was made to quantify the damping ratios found in these bending modes by applying input shaking simulating the experimental excitation using the finite element program

OpenSees. In this undertaking, possible sources of error are discussed.

The author then describes a numerical study performed on a calibrated wind turbine like structure involving the application of a large range of actual recorded input motions. Adjustments are made to the original fixed-base model, placing the structure on a linearly elastic soil domain by using BridgePBEE, a graphical interface tool that eases simulation and functions as a pre and post processor. Using this code, the numerical study is further extended by varying the supporting ground stiffness. The study then compares the tower maximal shear and moment values for the studied rigid and flexible ground scenarios and explores trends in the lateral force lever-arm of the system.

Chapter 1

Introduction

1.1 Wind Energy and Earthquake Activity

Wind Turbines are becoming increasingly established in the field of renewable energy. With modern incarnations of wind turbines having their roots in the windmills of Western Europe in the 16th and 17th centuries, they evolved with the considerable technological and scientific advances in the 19th and 20th centuries that allowed a more efficient conversion of wind energy into electrical power. By the nineteen nineties "wind farms" sprouted along the United States, especially in California (Hau, 2006). In recent years, with a greater push towards cleaner energy, wind turbines are receiving more attention as a viable option for producing some of the electric power required to feed modern societies' escalating demand for energy. Studies report that the top two countries in 2009 for producing wind energy were the United States and China with 35 and 26 GW, respectively (Wiser et al., 2011). Also notable was the number five spot, India, producing 11 GW according to the data.

However attractive the possibility of a civilization powered by wind energy, wind turbines themselves still require much development and testing. In particular, there exists only limited amount of data (if any) concerning the earthquake response of a large wind turbine. In fact, current design methods do not make special provisions for wind turbine structures (Witcher, 2005; Prowell and Veers, 2009). Because research in this area is still in the developmental stages, the proper design parameters for a wind turbine with anticipated seismic loads, in addition to aerodynamic loads, have yet to be fully established.

1.2 Brief Literature Review

The subject of earthquake loading was addressed in the early recommendations found in Risø (2002). Risø (2002) suggested a single-degree-of-freedom model for simulation. According to Risø (2002), the concentrated top mass should account for the combined weight of the nacelle, rotor, and a quarter of the tower weight. The implementation of a spectral response acceleration from a design response spectrum was advised to guide loading magnitudes. It was further proposed that a uniform acceleration equal to that of the maximal expected earthquake acceleration should dictate tower buckling behavior.

Other research efforts demonstrate the current goals and techniques in the characterization of wind turbine response to earthquakes. A study was performed on a smaller scale (by modern standards) 65 kW wind turbine in which the entire structure was mounted onto a large shake table and subjected to an input motion taken from the measurements of an actual earthquake. The resulting tower response was measured and transformed into the frequency domain to obtain the first two natural frequencies and normal modes of the structure (Prowell et al., 2009b; Prowell, 2010). These results were then compared to a finite element model. Another study also managed to accomplish the identification of the first three natural frequencies and mode shapes for a larger 900 kW wind turbine (Prowell, 2010). Due to the larger size of this turbine, mounting it on a shake table would have been much more difficult, and so this study was performed on site using only ambient vibration data that was transformed once again into the frequency domain. This data was subsequently compared with the predictions of a finite element model as well. Prowell (2010) also conducted harmonic forced-vibration base excitation tests, and the results thereof are studied in this thesis.

The very same mode shapes and natural frequencies from the 900 kW wind turbine in Prowell (2010) were then used again in Prowell et al. (2009a) to compare the experimental results with a finite element model resting atop a discretized soil domain. Due to mostly rigid soil conditions in the experiment, Prowell et al. (2009a) found agreement with the modal properties under very stiff elastic soil moduli in the model. The density and the elastic properties of the soil were subsequently varied in order to demonstrate that the effects of soil-structure interaction could become more pronounced and affect dynamic behavior under certain conditions of soft soil.

1.3 Objectives

This thesis, and the experimentation and the simulation that led up to it, attempt to contribute more information and knowledge to the subject of wind turbine modal properties, simulation, and their dynamics under seismic loading. The results will hopefully ensure that these turbines may be more accurately designed to withstand earthquakes and remain operational in the aftermath. In accomplishing this, the research gravitated in the direction of wind turbine modal identification from forced-harmonic base excitation with concomitant as well as separate inclusion of structure-ground interaction. As the reader progresses through the content of this thesis, the themes become very apparent.

The early chapters together will utilize a combination of experimental data from a 900 kW wind turbine and linear finite-element simulation to identify natural frequencies, mode shapes, and modal damping. To pave the way for perhaps more accurate modal simulation in the future, the rigid-base constraint is then replaced with the premise that the motion at the base is perceptible. As such, it was assumed that a set of linear springs, with stiffnesses varying for each bending mode, could represent constraining forces on the base. The experimental data is used in conjunction with the finite element model to back calculate the stiffness for each of these springs. Such investigations will hopefully promote a better understanding of the dynamic behavior of this particular class of wind turbine subject to acceleration input at the base.

Later in the thesis, a full linear finite-element model complete with a soil domain incorporating distant lateral boundaries is introduced and employed in situations of varying soil stiffness. These pilot analyses are performed with the expectation that a better understanding of the effects of soil-structure interaction on a wind turbine-like structure might be obtained. Any results will hopefully enlighten future researchers on methods to consider in performing these types of simulations (provided the researcher has access to the proper computational tools).

1.4 General Organization

Beginning in Chapter 2, an experiment conducted by (Prowell, 2010) is described involving the application of forced, harmonic vibrations from a shaker at the base of the wind turbine. It was during these vibrations that various accelerometers and data loggers took measurements and synchronized the data. From this data, the first few tower bending modes and associated natural frequencies of the wind turbine were then obtained. Those properties are then displayed as results.

Chapter 3 is a special chapter in that it concerns itself exclusively with providing estimates for the modal viscous damping ratios that correspond to the normal modes of Chapter 2. Making use of a reasonably accurate, linearly elastic finite-element model, the chapter attempts to numerically reproduce the physical situations presented to the wind turbine in the experimental case so as to appraise the required amount of damping for each of the modes. Due to the fact that only partial success was achieved, some of the results merited further explanation. A discussion on the half-power method applied to the experimental findings is also provided.

Chapter 4 also enlists the aid of the very same finite-element model of Chapter 3. In order to establish a more realistic model for turbine dynamics, this chapter provides numerical results, calibrated by experiments, for an approximate model of soil-structure interaction by using a set of springs at the base of the wind turbine instead of the conventional fixed-base assumption found in previous chapters. All interactions with the model base and the supports were assumed to behave like linear springs, associating a new set of spring constants with each bending mode. The chapter then describes the way in which the spring constants were determined. A set of spring constants were also determined for mode shapes obtained from a previous study (Prowell, 2010) involving output-only methods.

A modeling and software change occurs in Chapter 5. A more extensive effort is made to include soil-structure interaction. The finite-element model used is simplified at the structural level, but also enhanced at the support level by the inclusion of a soil domain. The chapter describes the means by which a soil domain was added to the structural model and then proceeds to simulate several earthquake events for the cases of rigid and flexible ground.

Chapter 6 is included to provide a brief overview of the general trends observed in this thesis. It serves as a definitive conclusion and unites many of the ideas presented in the previous chapters.

Appendix A is dedicated to providing details concerning the filtering algorithm used for the data records displayed in Chapter 2. Graphs are also provided in this appendix for comparison with their counterpart plots seen in Chapter 2 as a way to visually check the effectiveness of the filters.

In Appendix B, some further explanation is offered in light of the unexpectedly low first mode damping results shown in Chapter 3. The raw data is displayed and so is the frequency time series of the applied shaker motion records that were eventually chosen as representative of the first fore-aft and the first side-to-side motions. A few other records are introduced in this appendix to offer some more insight into the responses of low frequency bending modes.

A table is provided in Appendix C that offers a brief description of the earthquake events applied to the finite-element model of Chapter 5. This appendix also contains some graphics that display the free-field ground motion observed in Chapter 5 of a few earthquake events. Their inclusion is meant to validate the process of generating the input motion in such a way that the free-field motion is the same, regardless of the stiffness of the soil.

Bibliography

Hau, E. (2006). *Windmills and Windwheels.* Wind Turbines: Fundamentals, Technologies, Application, Economics. Springer, Berlin, Germany, 2nd edition.

Prowell, I. (2010). *An Experimental and Numerical Study of Wind Turbine Seismic Behavior.* PhD thesis, University of California, San Diego.

Prowell, I., Elgamal, A., Lu, J., and Luco, J. E. (2009a). "Modal properties of a modern wind turbine including SSI". In *17th International Conference on Soil Mechanics & Geotechnical Engineering*, Alexandria, Egypt.

Prowell, I. and Veers, P. (2009). "Assessment of Wind Turbine Seismic Risk: Existing Literature and Simple Study of Tower Moment Demand". Technical Report SAND2009-1100, Sandia National Laboratories.

Prowell, I., Veletzos, M., Elgamal, A., and Restrepo, J. (2009b). "Experimental and Numerical Seismic Response of a 65 kW Wind Turbine". *Journal of Earthquake Engineering*, 13(8):1172.

Risø (2002). *Guidelines of Design of Wind Turbines.* Det Norsk Veritas, Copenhagen and Wind Energy Department, Risø National Laboratory, Copenhagen, Denmark.

Wiser, R., Yang, Z., Hohmeyer, O., Infield, D., Jensen, P. H., Nikolaev, V., O'Malley, M., Sinden, G., and Zervos, A. (2011). *"Wind Energy".* IPCC Special Report on Renewable Energy Sources and Climate Change Mitigation. Cambridge University Press, Cambridge, United Kingdom and New York, NY, USA.

Witcher, D. (2005). "Seismic Analysis of Wind Turbines in the Time Domain". *Wind Energy*, 8(1):81–91.

Chapter 2

Dynamic Properties Derived from Experimental Data

This chapter will begin by introducing an in-situ experiment performed on a 900 kW wind turbine in which it was subjected to harmonic motion at the base. The chapter then describes how the obtained accelerometer data was analyzed leading to estimates of the natural frequencies and mode shapes.

2.1 A Note on Similar, Previous Studies

At this point it is prudent to mention that many of the properties observed in this chapter for the same system and utilizing the same instrumentation (described subsequently) are available in a study discussed in Prowell (2010b). In this earlier study the author's intent was to use ambient free-vibration experimentation and algorithms designed to extract dynamic properties from output-only methods. Prowell (2010b) implemented a combination of the Multiple-Reference Natural Excitation Technique (MNExT), which utilized Welch's method to estimate cross power spectra (CPS), and the Eigensystem Realization Algorithm (ERA) to estimate the natural frequencies of the wind turbine in question.

This study is different from that of Prowell (2010b) in that the experimental data used here was obtained while an external agent was imparting force on the wind turbine. That is, this study makes use of forced-harmonic data to obtain the dynamic properties of a wind turbine. Of course, since information concerning the input was known for these data sets, different methods than those of Prowell (2010b) (involving bandpass filtering) were employed in this study.

A reader interested in either this author's study or that of Prowell (2010b) can find some more information and even raw data sets on the NEEShub webpage (`http://nees.org/warehouse/project/661`).

2.2 Details of the Experimentation

2.2.1 System and Data Acquisition

The reader should note that Subsection 2.2.1 is a summary of what is more thoroughly described in Prowell (2010b). The turbine used for the acquisition of this data is a 900 kW, 3-bladed, horizontal-axis wind turbine with a 53.6 meter rotor diameter (see Figure 2.1). Figure 2.2 has also been included for the reader to reference as this thesis points out the different parts of a wind turbine. Furthermore, Table 2.1 is presented to list the important physical properties of the discussed wind turbine. The employed wind turbine was kept in the parked state for this experiment. That is, the rotor was not rotating. Additionally, the foundation is a Patrick-Henderson type design as can be seen in Figure 2.3. It is essentially a hollow cylindrical shell with a 3.5 meter outer diameter and completely embedded into the soil. This shell is composed of concrete sandwiched

Table 2.1: 900-kW Wind Turbine Characteristics (source Prowell, 2010b)

Type	Horizontal axis wind turbine
Nominal power	900-kW
Rotor diameter	53.6 m
Tower height	54 m
Hub Height	55 m
Operational Speed	14/22 RPM
Mass of nacelle	23,000 kg
Mass of rotor	18,300 kg
Mass of tower	68,700 kg

Figure 2.1: Tested wind turbine provided courtesy of Oak Creek Energy Systems (photo courtesy of Prowell, 2010b).

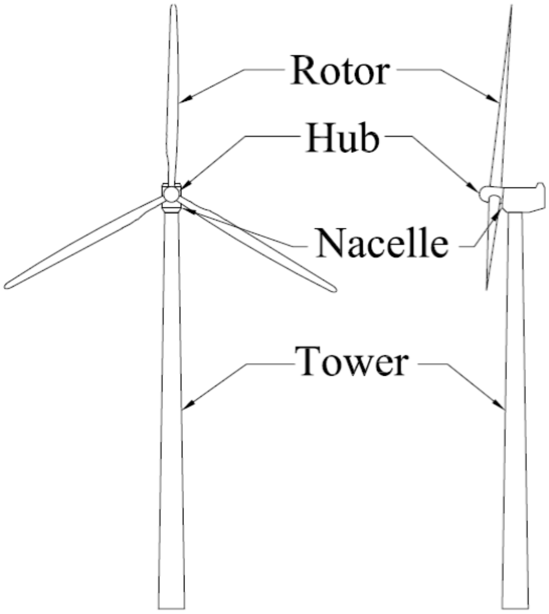

Figure 2.2: Image displaying the most essential features of a wind turbine (courtesy of Prowell, 2010b).

between steel shells spaced 0.3 meters apart. The foundation is attached to the wind turbine through un-bonded post tensioned bars extending to the bottom of the foundation. In the final configuration, the foundation is embedded 9 meters deep into the ground (Prowell et al., 2009).

Also of note, especially as it will relate to the content of Chapters 4 and 5, is the soil profile. From the surface to the depth of 2 meters, the soil is characterized with properties and behavior of sandy materials. Below that the soil is highly compacted, and the behavior of dense, silty, and clayey sands is observed (Prowell et al., 2009).

The measuring instruments were provided by the mobile laboratory of the George E. Brown Jr. Network for Earthquake Engineering Simulation at the University of California, Los Angeles (NEES@UCLA). The actual measurements were taken with EpiSensor accelerometers (from Kinemetrics Inc.) which were placed at varying heights (ground level, 7, 13, 22, 32, 42, and 52 meters) along the 54 meter tall tower of the wind turbine. Several accelerometers per height level were also used and placed in perpendicular orientations in order to measure the response along multiple directions (fore-aft, side-to-side, and vertical motion). The accelerometer data was then captured by Q330 data loggers, which were capable of 24-bit analog to digital conversion and time synchronization across multiple nodes. The resulting data was collected into a single laptop via Ethernet. This is visually displayed in Figure 2.4.

2.2.2 Shaker and Testing Protocol

The source of the forced vibrations was the 4600A portable eccentric mass shaker (for simplicity, it will just be referred to as the shaker) which was provided once again by NEES@UCLA (see Figures 2.5 and 2.6). It functions by spinning a set of counter-rotating weights about two vertical axles, thereby applying centrifugal forces to any member to which it is attached. The force exerted by eccentric mass shakers such as this can be modeled simply using Newton's Second law. For a mass m, a distance from the axis of rotation r, and a circular frequency ω,

$$F_{net} = ma_{centripetal} = mr\omega^2$$

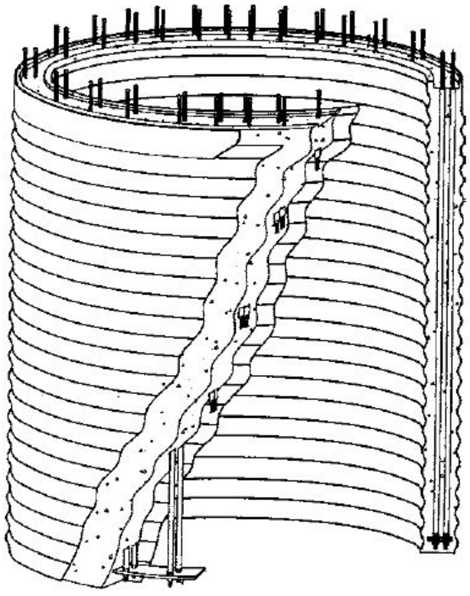

Figure 2.3: Patrick-Henderson foundation (image from `http://www.windfarmbop.com/patrick-henderson-foundation/patrick-henderson-1/`).

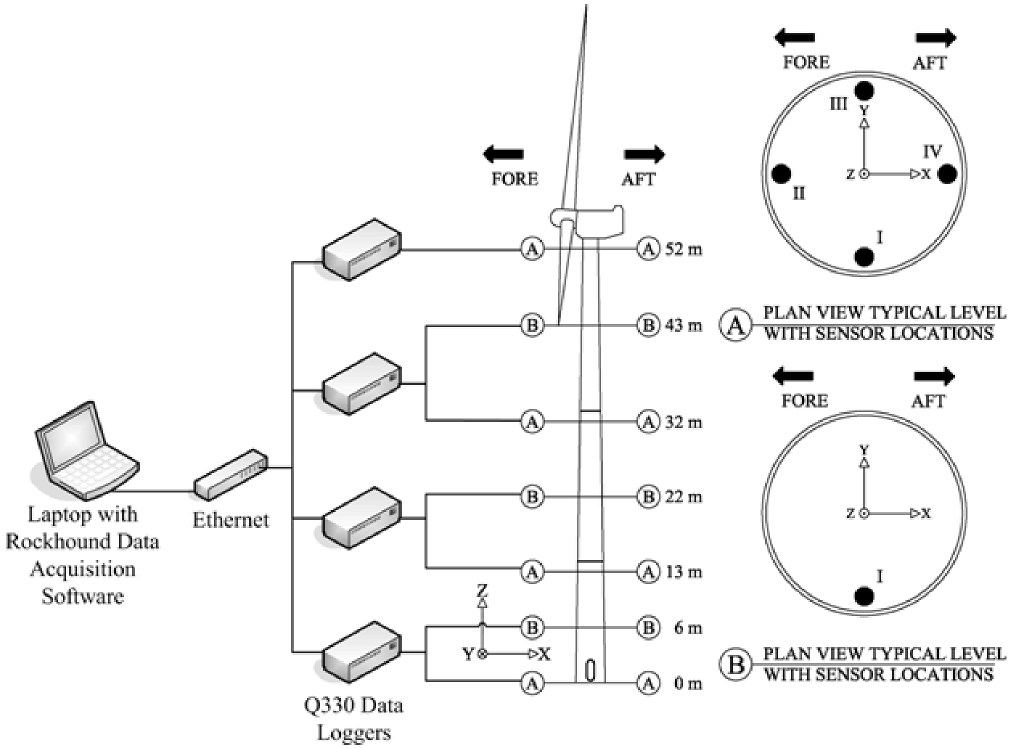

Figure 2.4: Schematic diagram of the data acquisition process (Prowell, 2010b).

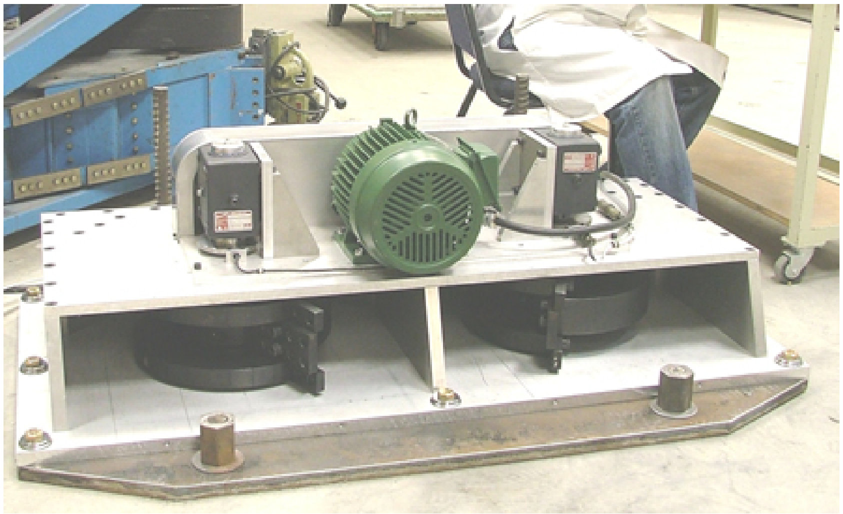

Figure 2.5: 4600A Portable Eccentric Mass Shaker (the attached photo is courtesy of `http://nees.ucla.edu/shakers.html`).

So, for some range of mass, radial distance, and rotational frequency, the shaker force $F \propto \omega^2$. Furthermore, the shaker was rated to have a maximum force output of 20,000 lbs and designed for operation at 0-20 Hz for small masses (980 lb-in or less) and 0-10 Hz for large masses (4,600 lb-in or less). A plot of the shaker force as a function of the linear frequency has been provided so that the reader can have a better grasp of the shaker's impact on the wind turbine (Figure 2.7). Since the subject of this thesis is to approximate the typical low frequencies observed in most earthquakes and examine their effect on wind turbine response, the shaker frequency was restricted to 13 Hz or less and administered to the base of the tower of the wind turbine. Of further interest in Figure 2.7 is the magnitude of the shaker forces at frequencies less than 1 Hz. The graph clearly illustrates that at these low frequencies the shaker is very ineffective at providing excitation. As the reader will see later, this had a detrimental impact on the employed identification process related to the first bending modes, which are reported be at about 0.5 Hz (explained subsequently, please see Chapter 3).

It has been observed from earthquake simulations on wind turbines that while a large amount of seismic energy is associated with the first mode relative to higher modes (as much as 54% of the total tower energy), the higher modes'

Figure 2.6: Shaker being mounted onto the wind turbine base. (Source: Prowell, 2010a)

contribution is not negligible (Prowell and Veers, 2009). It is therefore important to identify several of the turbine tower modes in order to accurately represent the wind turbine dynamics under the conditions of seismic excitation.

During the experiment, two kinds of shaker behavior were repeatedly utilized to obtain information about natural frequencies of the wind turbine. The first is a “sweep” in which the shaker frequency was increased linearly from zero to a certain frequency (13 Hz, for example), and then decreased linearly back to zero. These kind of tests were useful for determining an approximate frequency range for which the wind turbine experienced a large level of response for a given excitation and tend to work best for systems where the natural frequencies are spaced sufficiently far apart. For example, results could be displayed by a transfer function of the turbine given over several elevations along the turbine tower.

Another simple way of doing this would be to create a plot similar to that depicted in Figure 2.8. The base acceleration response is displayed in the top two plots and the frequency in the bottom third. The general behavior is consistent with Figure 2.7 in that acceleration increases with increasing shaker frequency. Notice, however, that at around time $t = 250$ seconds, and again at around time $t =$

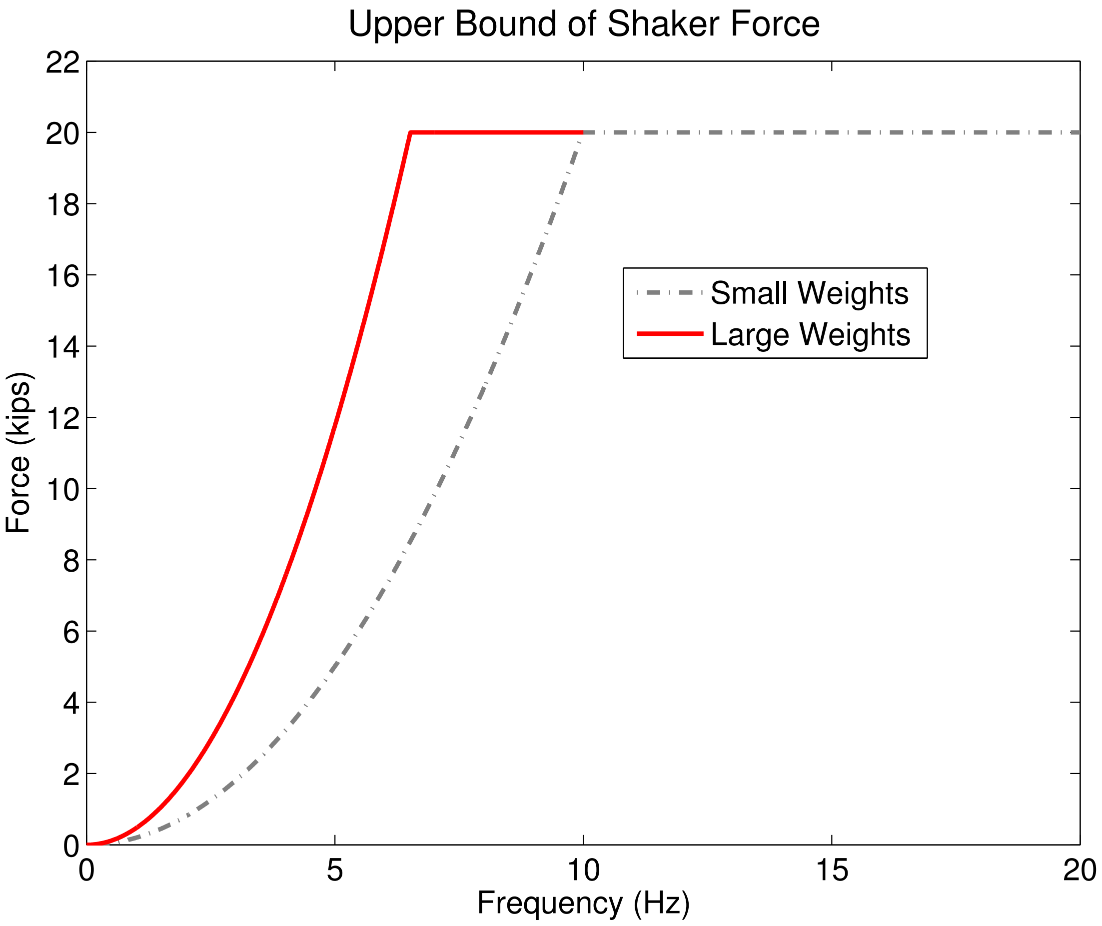

Figure 2.7: Forces exerted by the shaker on the wind turbine as a function of frequency. (Source Prowell, 2010a)

370 seconds, the acceleration in the side-to-side direction sharply diminishes before rising again. It is important to note the crests in close vicinity of this diminished response. In the first half of the record when the frequency is increasing linearly, at around $t = 240$ seconds, the local maximum response just before the signal diminishes corresponds to the time when the shaker was rotating the masses at just shy of 4 Hz. In the second half of the record with decreasing frequency, the closest response local maxima occurs once again when the shaker operating frequency is slightly less than 4 Hz. Even at base level, the wind turbine produces a noticeably different response when forcibly driven at this frequency, thus having all the more potential to propagate further up the turbine tower. For these reasons, sweep

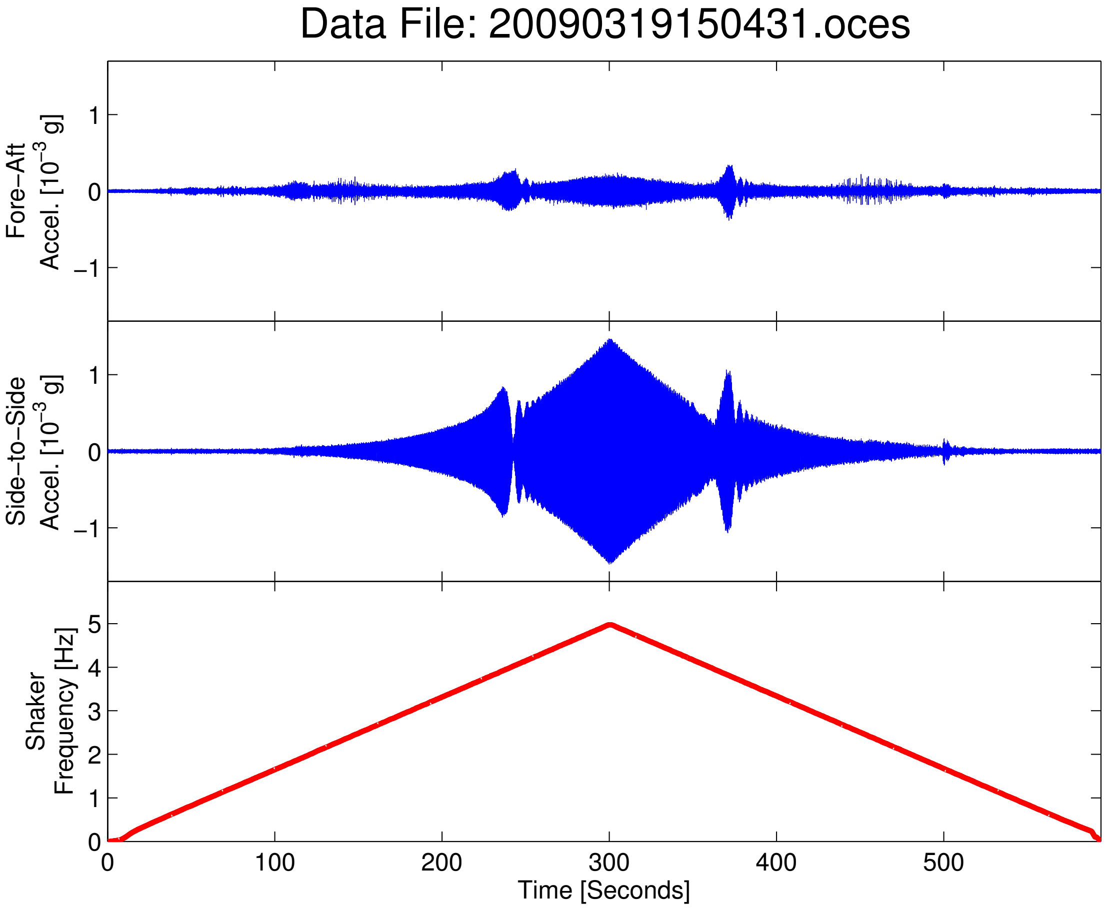

Figure 2.8: Sample horizontal acceleration response directly adjacent to the shaker and incident frequency time series (2$^{\text{nd}}$ side-to-side mode).

records were considered early in obtaining rough estimates of natural frequencies.

Similar behavior can be seen in Figure 2.9 for the fore-aft direction. Once again, the pinching effect is observed when approaching a particular frequency range from both above and below. However, in this figure, the graph suggests that the frequency at which this effect occurs is in the vicinity of 9 Hz.

Once an analysis of those tests are done, the second kind of test, a “dwell” can be performed. In a dwell, a very narrow frequency band is covered during the entire test. Many times, the frequency stays constant for a large amount of time. Operating under the assumption that the shaker driving frequency is sufficiently sensitive and responsive, this kind of test is functional in the sense that the driving frequency can be varied very slowly, the turbine tower response can be observed,

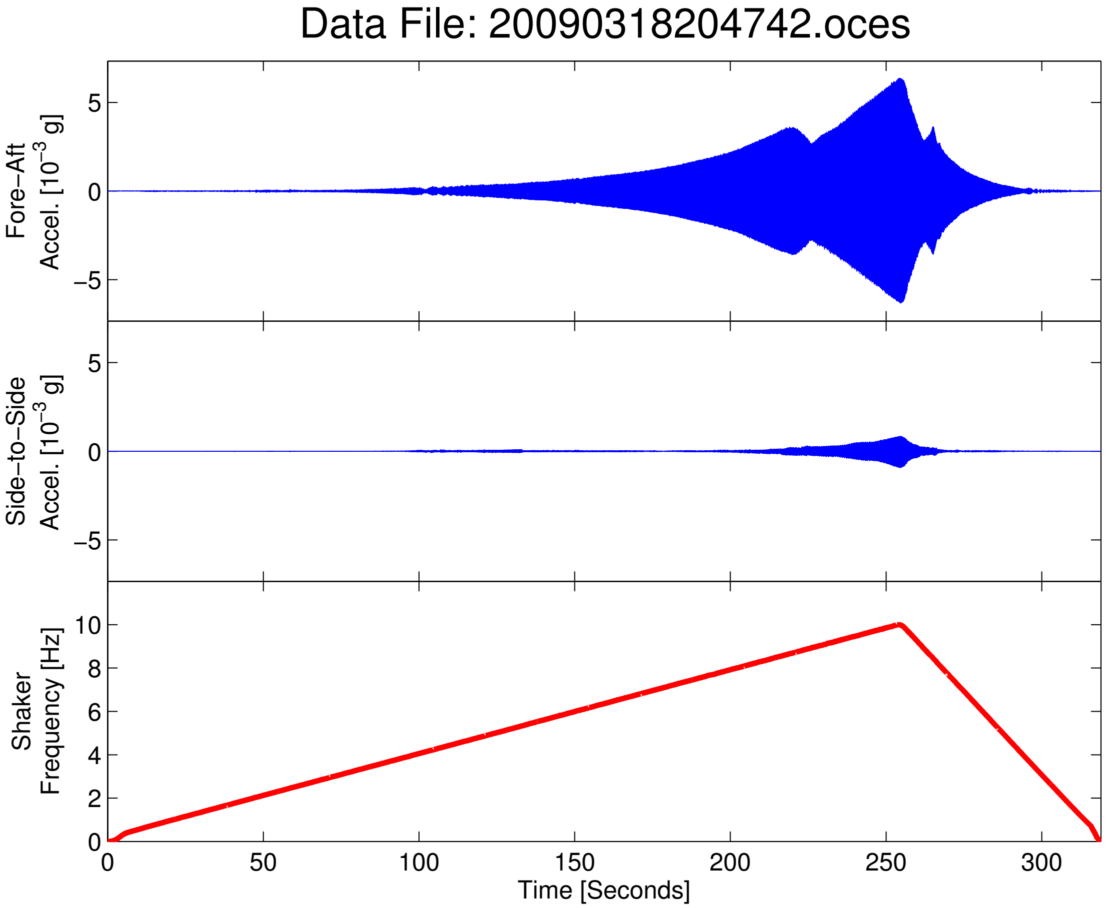

Figure 2.9: Sample horizontal acceleration response directly adjacent to the shaker and incident frequency time series (3^{rd} fore-aft mode).

and a subsequent analysis performed on the resulting time series could determine if a steady state sinusoidal response on the tower was obtained. Such a finding would suggest the identification of a normal mode. Properly documenting the frequency as a function of time, or a measurement of a steady state frequency from the time series analysis would then be the natural frequency.

The expectation was that the turbine mode shapes would be completely three dimensional. For the best results, it was then necessary to change the shaker orientation about the base so as to obtain data with the primary direction of its force acting in two perpendicular directions. The experiment was performed such that the shaker forcing was either in the fore-aft or side-to-side direction for any given test. From these tests, it is believed that the first three fore-aft and the first three side-to-side natural frequencies, and therefore the fore-aft and side-to-side tower mode shapes, were observed.

Before continuing, one important distinction must be made. Although there was no accelerometer placed on the shaker itself, the accelerometer at ground level is considered the response at that height. This is because the base is effectively rigid and the shaker is transmitting force directly onto the base itself.

2.3 Notation

This section is provided for the purposes of facilitating communication of algorithms and procedures performed on the data obtained from the experiment.

As the reader can see in Figure 2.4, sensors (accelerometers) were attached to the wind turbine tower at 7 locations along the height, and even then, multiple accelerometers were oriented in perpendicular directions for the full measurement of 3 dimensional response. For the results obtained in this chapter, the author has used a subset of this data, namely two data sets for each elevation corresponding the measurements of the two perpendicularly oriented accelerometers closest to the shaker. In other words, seven fore-aft data sets and seven side-to-side data sets for a total of fourteen.

From this description, it is evident that the response had variations in each direction (fore-aft and side-to-side, or alternatively, x and y), elevation (0, 6, 13, 22, 32, 43, and 52 meters), and in the time domain. In a description involving a continuum of time, the representation of the full acceleration of the wind turbine might appear as

$$\ddot{\mathbf{U}}(t) = \begin{bmatrix} \ddot{\vec{u}}_0(t) & \ddot{\vec{u}}_6(t) & \dots & \ddot{\vec{u}}_{52}(t) \end{bmatrix} \tag{2.1}$$

where an arrow indicates a vector quantity (in this case, the vectors are composed of one fore-aft and one side-to-side component), and a bold typeset refers to an array that is two dimensional or higher (two-dimensional as in Equation (2.1) above). Dots above a quantity refer to time differentiation and are used here to denote the fact that the quantities are accelerations. The subscripts on the individual vectors also refer to the elevation from which they are taken. The reader should note that

$i = 1, 2 = x, y =$ fore-aft, side-to-side and $j = 0$, 6, 13, 22, 32, 43, 52, which for notational convenience will be referred to as $\{j\}$. This should be read as "the set of j." Once the time domain has been discretized, $t \to t_k$ where $k = 1$, 2, 3, …, n and t_n is the last instant in which a measurement was obtained for this set of data records, then the representation transforms Equation 2.1 from a two dimensional continuum array into a three dimensional discrete array, which will be referred to as $\ddot{U}_{ijk}$. This quantity shall be referred to as the response array.

2.4 Post-Processing, Results, and Analysis

The reader should be aware that there is more information on how filtering was applied to the raw data sets in Appendix A. Additionally, some graphics of the raw data sets are shown in that appendix for the purposes of direct comparison with those displayed later on in this chapter.

The end products of applying the filters to the response array are displayed in Figures 2.10-2.15. Note that while many of these figures do not appear to have much excitation at the turbine base, this is merely because the scaling of these graphs is based on the maximum measured excitation for each data record and it just so happens that the measured accelerations elsewhere on the turbine tower are several orders of magnitude greater than at base level. The reader will also observe that each plot is given a title that appears to be a sequence of numbers followed by a ".oces." These have been left on the graphs as they indicate the name of the data file used to produce this image.

Figures 2.10-2.15 should also be compared to their unfiltered counterparts, Figures A.1-A.6. As expected, a side-by-side comparison of the modes that did not originally have much noise distortion to those same modes after filtering reveals that little change actually took place in these cases. These figures also suggest that filtering is necessary at frequencies of about 0.50 Hz or less and not necessary at frequencies of about 3.90 Hz or greater.

After filtering, the records showed the unobstructed sinusoid that had been expected (at least within a localized amount of time). In hopes of obtaining the best results leading to the mode shapes, the absolute value of each element in the response array was taken. Once this was done, the maximum of all entries was found. A slice in time about where this absolute maximum occurs in the response array is taken and used as the maximal response profile (later used as the bending mode shape).

Stated more formally, the following operation was performed

$$\left|\ddot{U}_{mnp}\right| = \max_{\substack{i=1,2\\ j\in\{j\}\\ 1\leq k\leq n}} \left|\ddot{U}_{ijk}\right| \tag{2.2}$$

where m, n, and p are some indices within the set of all i, j, and k, respectively. Once m, n, and p are obtained, the maximum response profile, $\ddot{\mathbf{U}}^{max}$, can defined as

$$\ddot{U}_{ij}^{max} = \ddot{U}_{ijp} \tag{2.3}$$

where i and j are defined in the same way as in Section 2.3.

This maximum response profile was the primary parameter used in the determination of whether or not a record was close to resonance. As already mentioned, since by now the signal was very close to sinusoidal, it was reasonable to estimate the frequency around $\ddot{U}_{mnp}$ by obtaining approximate values of the two closest zero crossings on either side of this value. This is equivalent to finding half a period, and so the result was multiplied by 2 and then inverted. Table 2.2, wherein all the natural frequencies represented by the graphs are listed (in the middle column), is also provided for convenience. These frequencies are consistent with those reported from the free-vibration study (Prowell, 2010b) and vary only to within three percent (Prowell, 2010b).

The records used in the Figures 2.10-2.15 were carefully selected to include only those instances where the shaker was performing a dwell. This was done to avoid instances of fleeting maxima, which could have resulted from an encounter of the beating phenomena (Vierck, 1979).

For the visualization of the mode shapes in Figures 2.16-2.21, the data points were obtained by imaging the maximum response profile $\ddot{\mathbf{U}}^{max}$. For these figures, all accelerations are exaggerated, but made to scale. Please note that

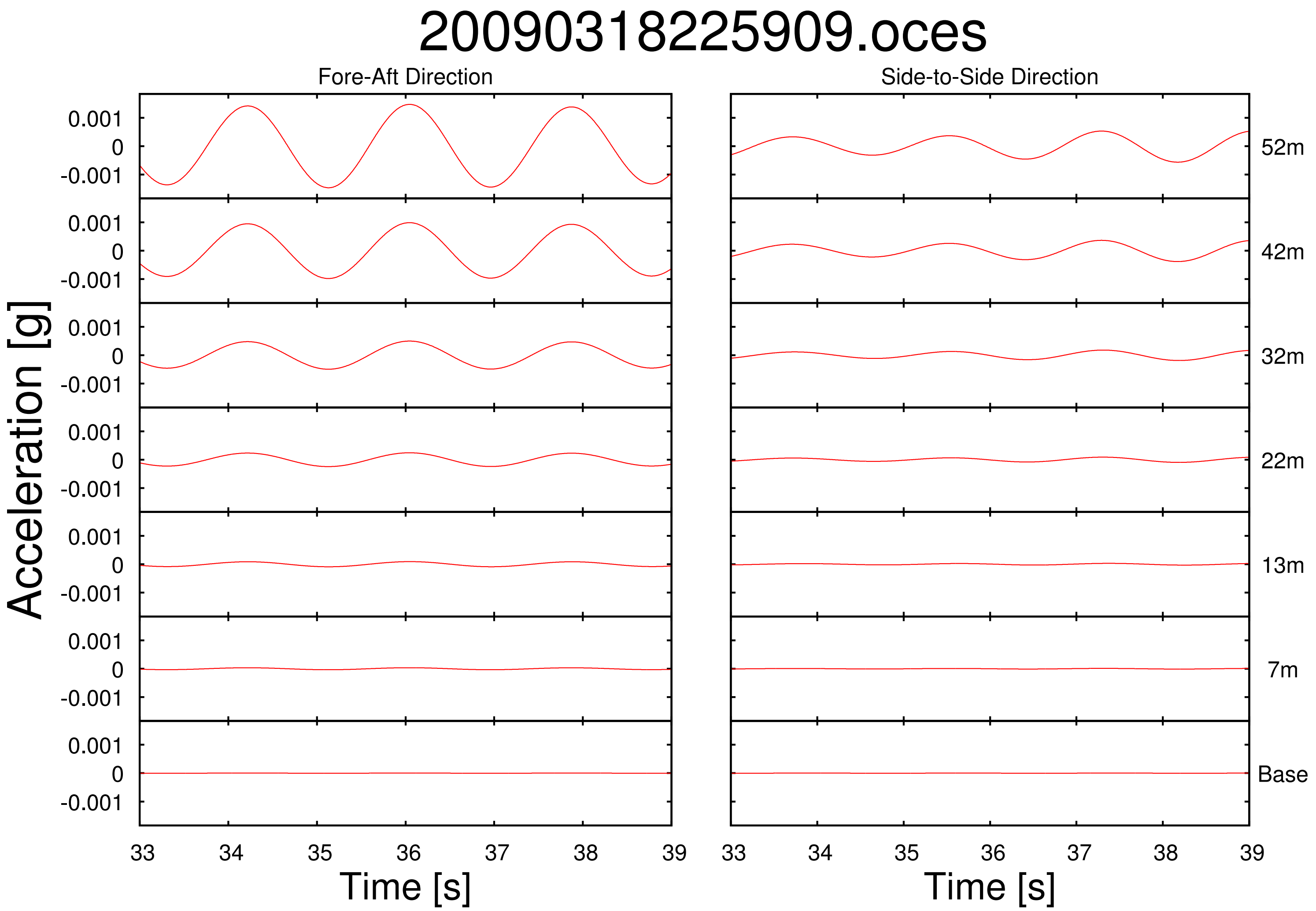

Figure 2.10: First fore-aft, filtered time series. Observed frequency: 0.55 Hz.

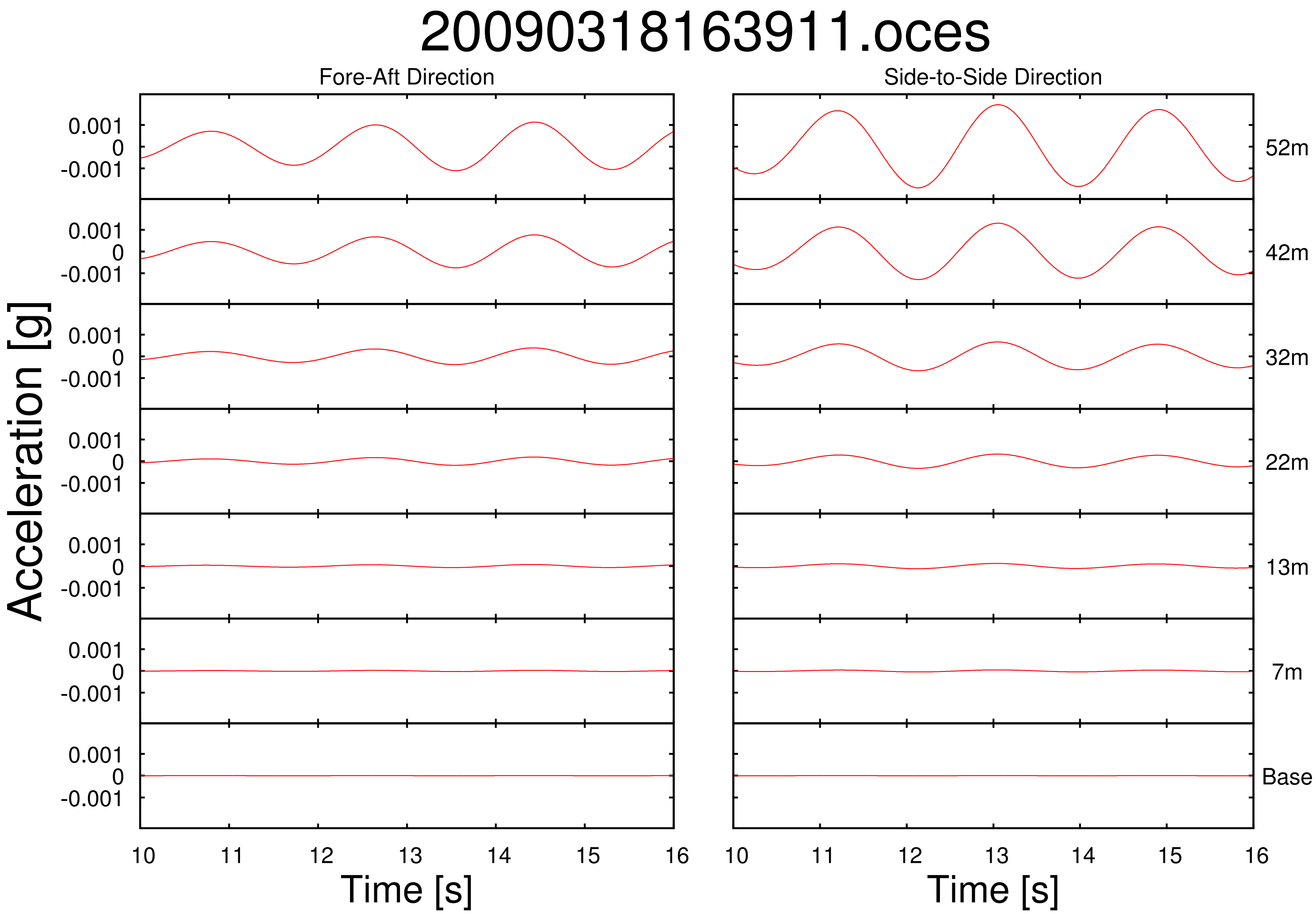

Figure 2.11: First side-to-side, filtered time series. Observed frequency: 0.54 Hz.

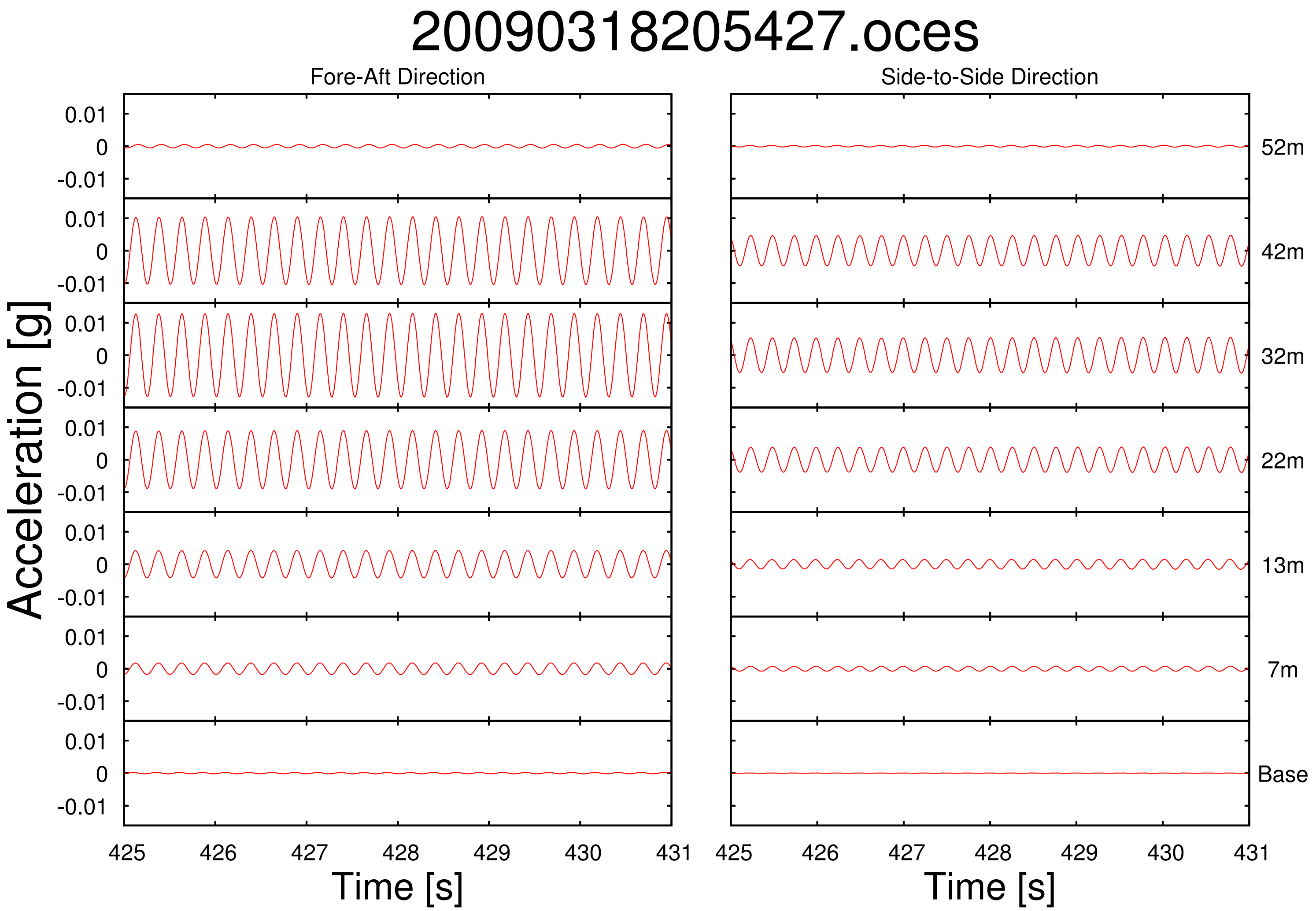

Figure 2.12: Second fore-aft, filtered time series. Observed frequency: 3.95 Hz.

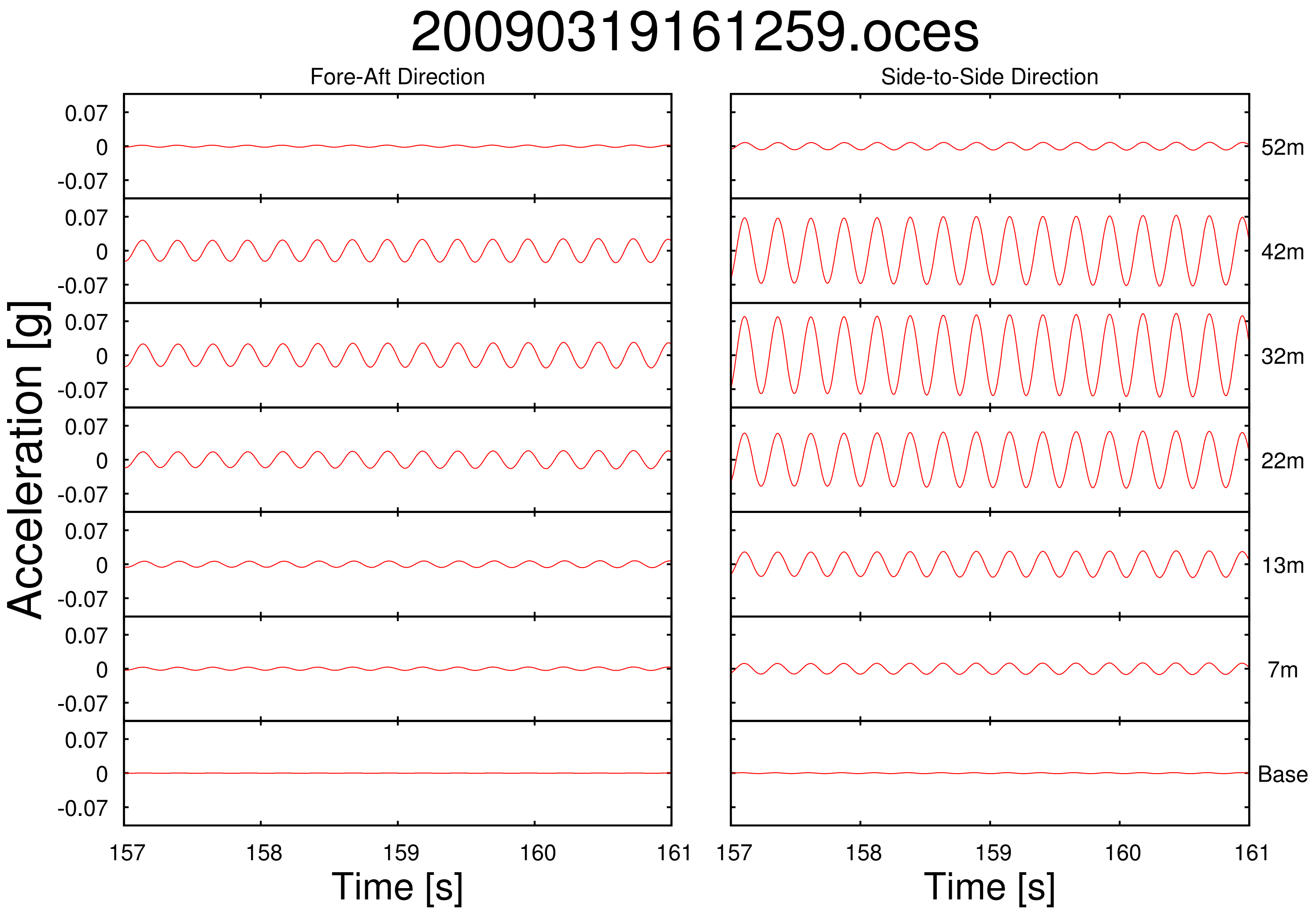

Figure 2.13: Second side-to-side, filtered time series. Observed frequency: 3.90 Hz.

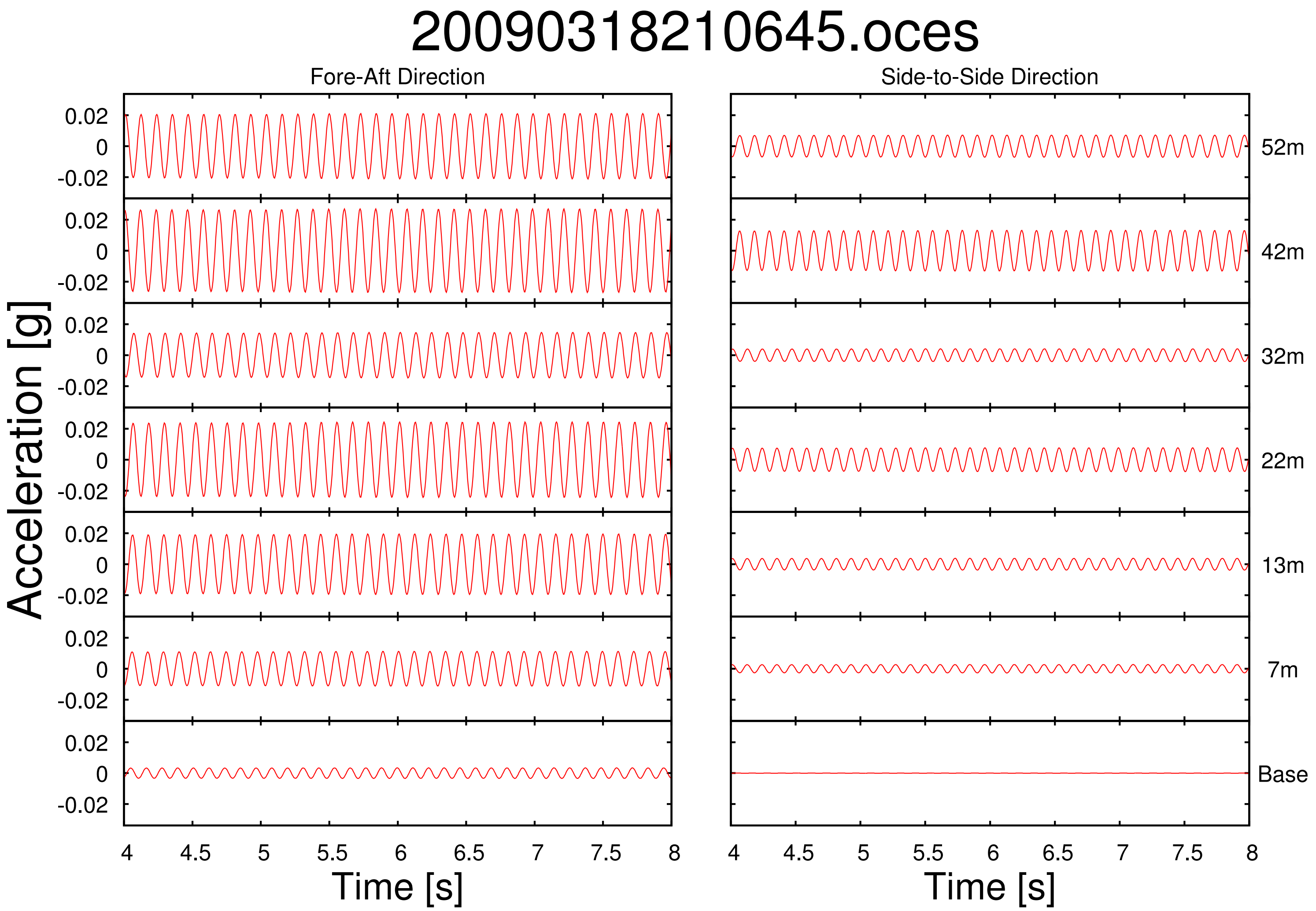

Figure 2.14: Third fore-aft, filtered time series. Observed frequency: 8.73 Hz.

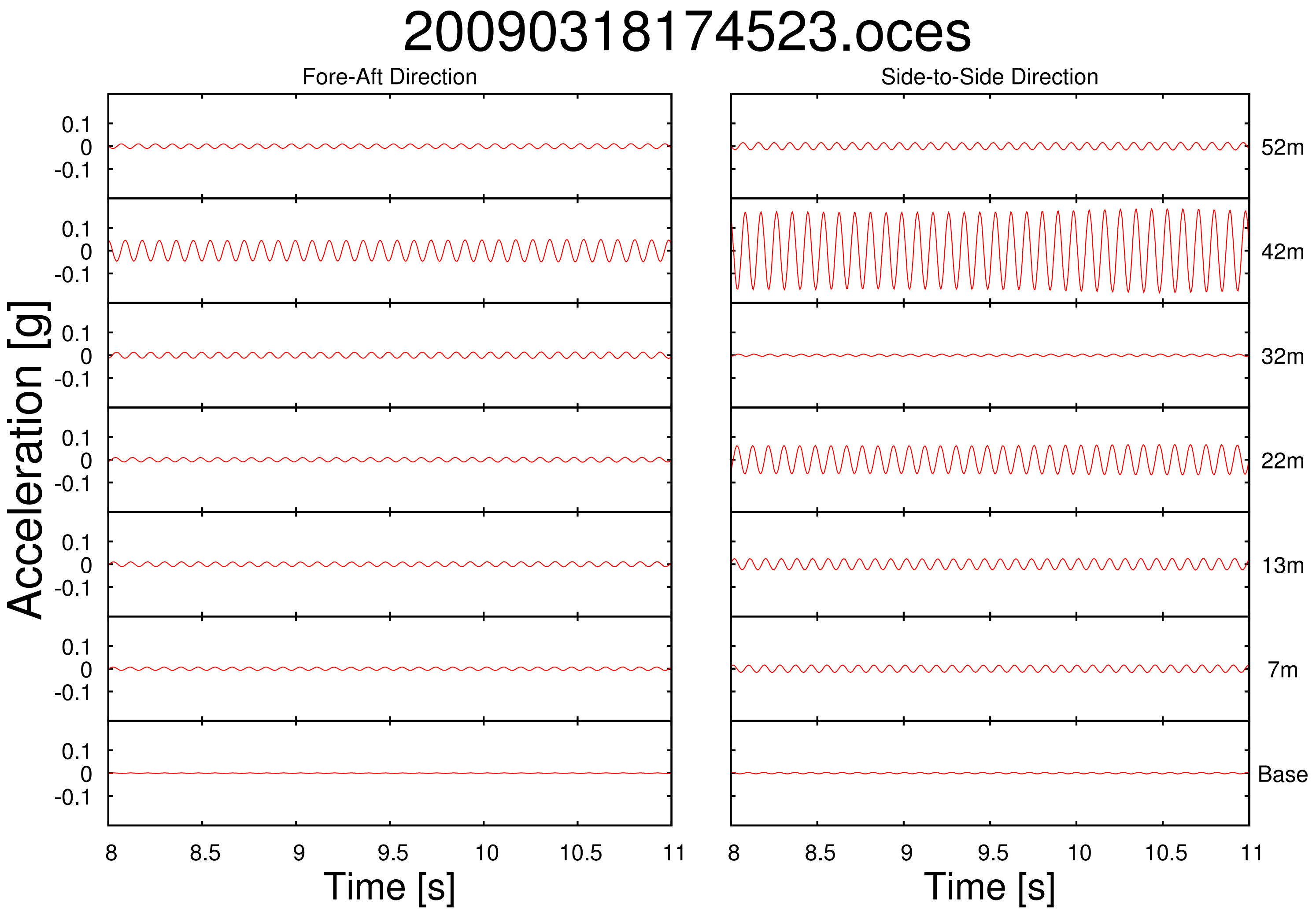

Figure 2.15: Third side-to-side, filtered time series. Observed frequency: 11.05 Hz.

Table 2.2: Comparison between the experimental natural frequencies from this the previous study of Prowell (2010b)

Bending Mode	Forced-Harmonic Frequency [Hz]	Free-Vibration Frequency [Hz] (Prowell, 2010b)
1^{st} Fore-aft	0.55	0.56
1^{st} Side-to-side	0.54	0.54
2^{nd} Fore-aft	3.95	4.00
2^{nd} Side-to-side	3.90	3.94
3^{rd} Fore-aft	8.73	8.86
3^{rd} Side-to-side	11.05	10.90

these mode shapes did not take into account the accelerations of the blades and are strictly meant to represent the relation between accelerations along the turbine tower. These data points were then Spline interpolated for smoothness upon visualization.

When evaluated next to the mode shapes of the free-vibration study (Prowell, 2010b), which have been included in Figures 2.22-2.27, the mode shapes of this report are holistically comparable, though there exists some dissimilarity with the relative phase between the principle direction of bending and the perpendicular direction.

One of the fortunate advantages of the method used in this report is that if a sinusoidal signal is recovered, as in this case, then comparing the acceleration responses for the same temporal period across channels lends itself to discerning the relative phase. For example, an observation of the filtered time series for the third fore-aft mode at the time $t = 7$ seconds reveals that at this moment in time, the top two channels, located at 52 and 42 meters above ground level, respectively, are very close to a sinusoidal crest. The rest of the channels simultaneously behave similarly to asinusoidal trough. It is therefore readily apparent that there is essentially a $180\,^{\circ}$ phase shift between the channel at 42 meters and the channel at 32 meters. For further clarity, the relative phase between two data points can also be seen on the visualized mode shapes as having different sections of the tower deflected in opposite directions (most evident in the third fore-aft and side-to-side mode

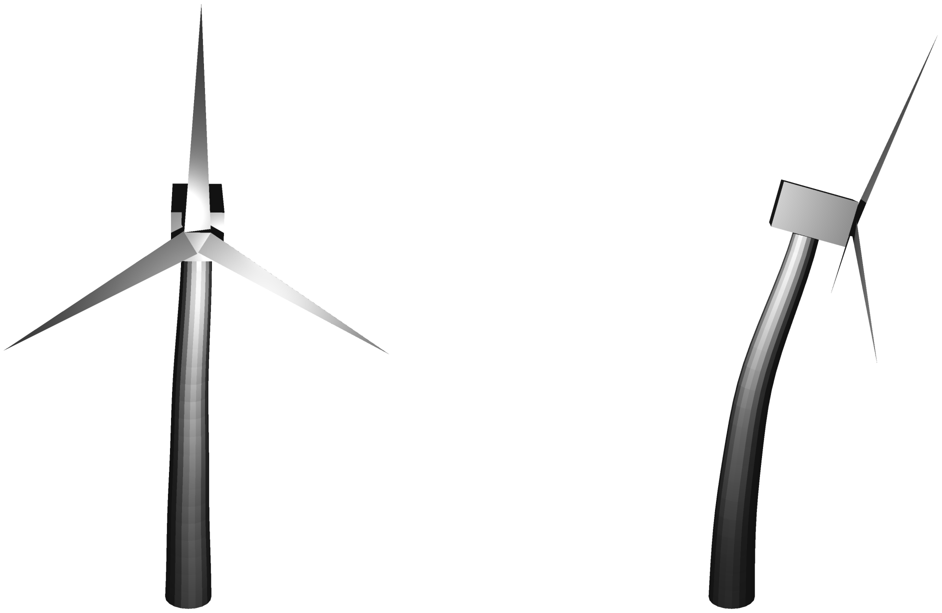

Figure 2.16: Frontal and side views of the 1^{st} fore-aft bending mode at the peak of acceleration response. (forced-harmonic result)

Figure 2.17: Frontal and side views of the 1^{st} side-to-side bending mode at the peak of acceleration response. (forced-harmonic result)

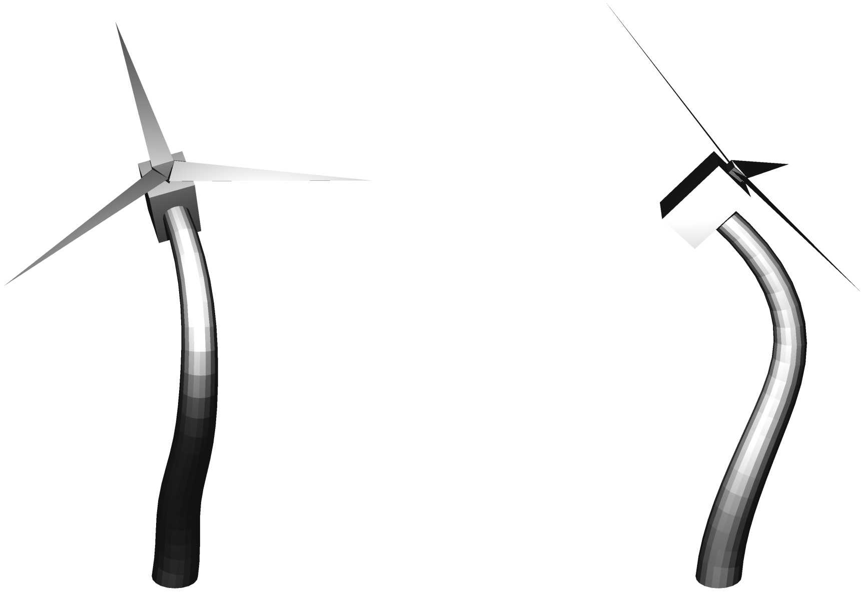

Figure 2.18: Frontal and side views of the 2^{nd} fore-aft bending mode at the peak of acceleration response. (forced-harmonic result)

Figure 2.19: Frontal and side views of the 2^{nd} side-to-side bending mode at the peak of acceleration response. (forced-harmonic result)

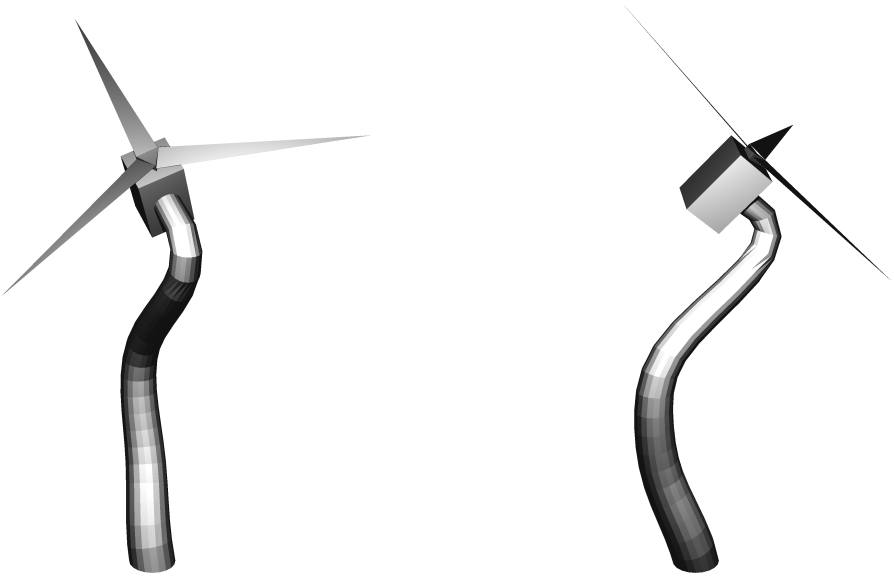

Figure 2.20: Frontal and side views of the 3^{rd} fore-aft bending mode at the peak of acceleration response. (forced-harmonic result)

Figure 2.21: Frontal and side views of the 3^{rd} side-to-side bending mode at the peak of acceleration response. (forced-harmonic result)

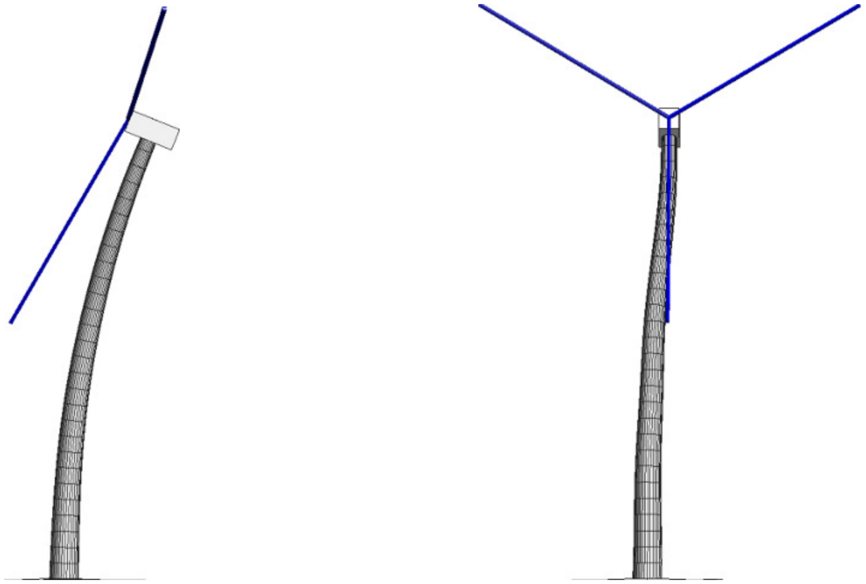

Figure 2.22: Frontal and side views of the 1st fore-aft bending mode from the free-vibration study (Prowell, 2010b).

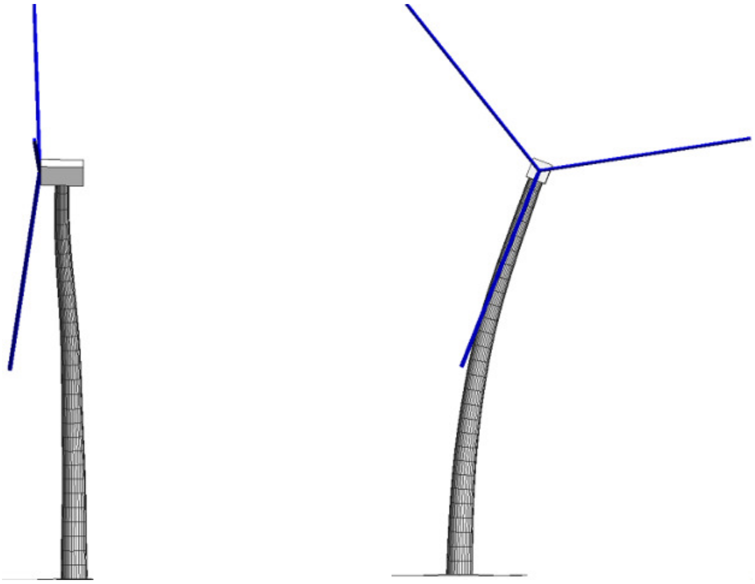

Figure 2.23: Frontal and side views of the 1st side-to-side bending mode from the free-vibration study (Prowell, 2010b).

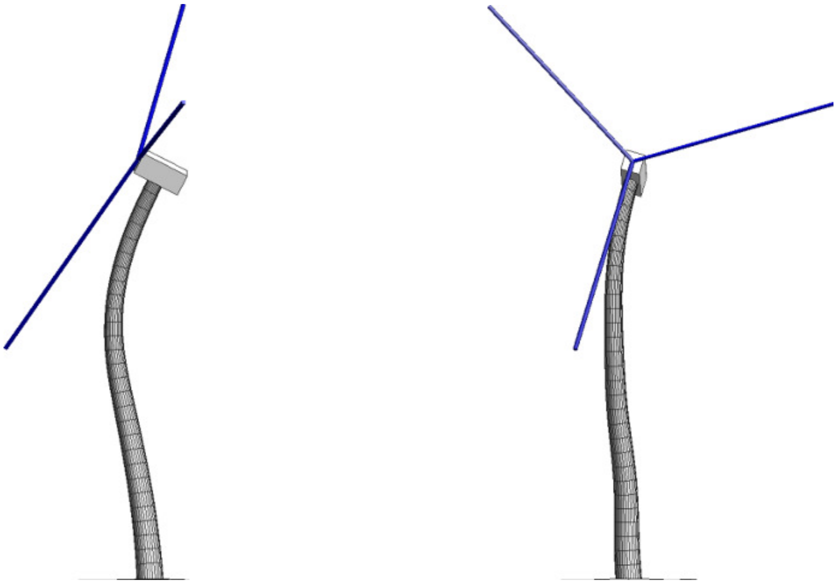

Figure 2.24: Frontal and side views of the 2$^{\text{nd}}$ fore-aft bending mode from the free-vibration study (Prowell, 2010b).

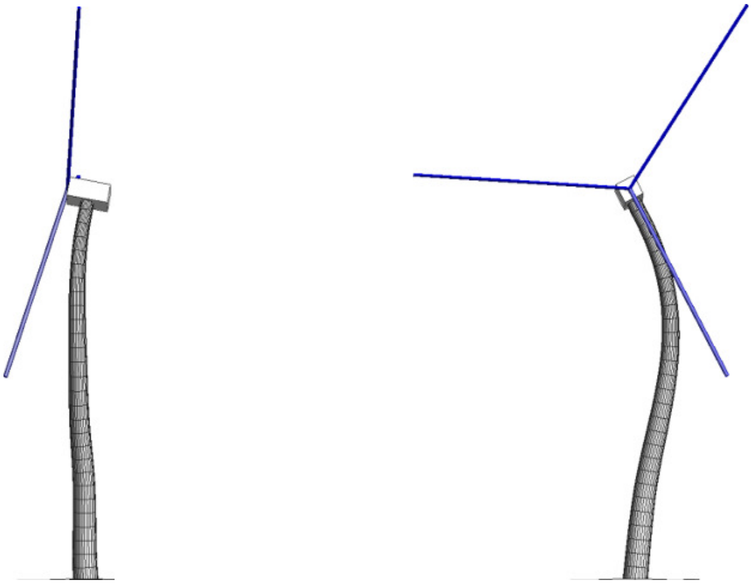

Figure 2.25: Frontal and side views of the 2$^{\text{nd}}$ side-to-side bending mode from the free-vibration study (Prowell, 2010b).

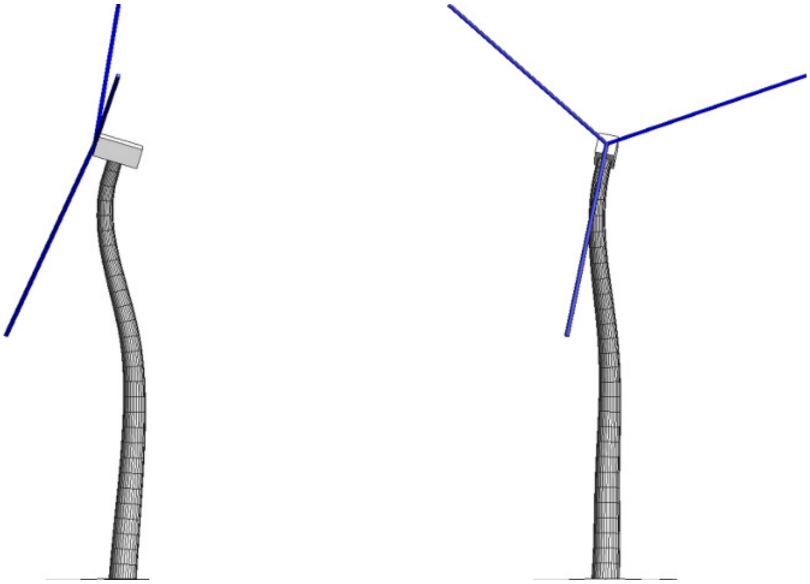

Figure 2.26: Frontal and side views of the 3$^{\text{rd}}$ fore-aft bending mode from the free-vibration study (Prowell, 2010b).

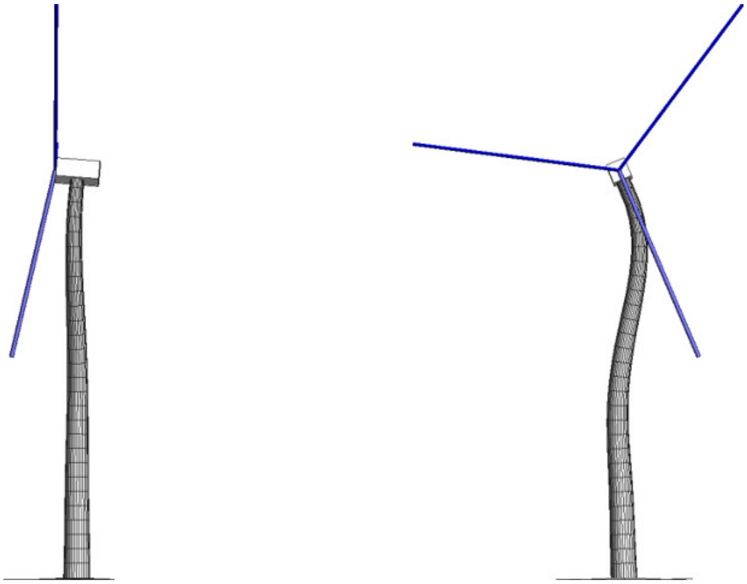

Figure 2.27: Frontal and side views of the 3$^{\text{rd}}$ side-to-side bending mode from the free-vibration study (Prowell, 2010b).

shapes).

Bibliography

Prowell, I. (2010a). Personal Communication.

Prowell, I. (2010b). *An Experimental and Numerical Study of Wind Turbine Seismic Behavior*. PhD thesis, University of California, San Diego.

Prowell, I., Elgamal, A., Lu, J., and Luco, J. E. (2009). "Modal properties of a modern wind turbine including SSI". In *17th International Conference on Soil Mechanics & Geotechnical Engineering*, Alexandria, Egypt.

Prowell, I. and Veers, P. (2009). "Assessment of Wind Turbine Seismic Risk: Existing Literature and Simple Study of Tower Moment Demand". Technical Report SAND2009-1100, Sandia National Laboratories.

Vierck, R. K. (1979). *Harmonically Forced Vibrations for Single-Degree-of-Freedom Systems*, chapter 4, pages 90–147. Vibration Analysis. Harper and Row, New York, N.Y., second edition.

Wolfgang, G. (2010). "NEES@UCLA Earthquake Engineering Mobile Laboratory". `http://nees.ucla.edu/shakers.html`. Accessed December 16, 2010.

Chapter 3

Estimated Modal Damping Based On Numerical Modeling

This chapter presents a finite element model (Prowell, 2010) emulating the wind turbine structure of Chapter 2. Using the recorded base excitation as input, the responses observed for each bending mode from Chapter 2 are then reproduced as faithfully as possible in the finite-element model so as to have a measure of modal damping. The results are then presented and some discussion follows addressing the validity of this method. The half power method is also introduced at this chapter's close.

3.1 Numerical Model

This section attempts to further the knowledge concerning the modeling of a wind turbine by including a numerical component. The model wind turbine geometry is the same as the one created by Prowell (2010). This subsequently described numerical model was implemented in OpenSees, an academic tool and finite element computational environment programmed in the TCL language (Mazzoni et al., 2006). Whereas the geometry of the blades on a wind turbine has, in the past, often been modeled as a lumped mass simply placed at the top of the tower (Bazeos et al., 2002; Risø, 2002), for the purposes of subsequent discussion, the model used in this study was completely three dimensional and constructed using linear elastic beam-column elements to represent the tower, nacelle, and blades (Prowell et al., 2009; Prowell, 2010). That is, the nacelle and the blades are treated more faithfully as a system of distributed masses and stiffnesses. In total, the model contains 118 nodes encompassing 51 tower elements, 3 nacelle elements, and 63 blade elements (21 elements per blade). For this portion of the study, the wind turbine was assumed to have a fixed base. To further elaborate on the numerical wind turbine model, Table 3.1 has been reproduced from Prowell (2010), stating some of the properties of the model. As described in that publication, these numbers were based on engineering drawings and the proper scaling attributes.

Table 3.2, created using information from (Prowell, 2010) is shown as evidence assuring the validity of the model. The numerical model appears to make predictions for most of the natural frequencies accurate to within 7% of those measured from the experiment and the accompanying filtering scheme. The exception occurs, however, in the third fore-aft bending mode, where the error had is more obvious, causing some divergence. This error also seems to have been present in Prowell (2010).

3.2 Modal Damping

For a complete description of the dynamics of a wind turbine, some estimates of damping would have to be made. The method used to approximate damping attempted to combine the results of Chapter 2 with the reproducibility of the computer model. The experiment was simulated in the numerical model by exciting it with a sinusoidal input signal at the base. Since it was desired to observe the behavior of the numerical model at resonance, the frequency of the input signal was chosen to be that of the natural frequencies corresponding to the tower normal modes of the model to machine precision to avoid beating as much as possible. These frequencies are shown and labeled as “Numerical Frequency [Hz]” in Table 3.2. The amplitude of the sinusoid was desired to correspond as much as possible to the experiment. Therefore the root-mean-square (RMS) of the filtered base signal time series as the tower approached the maximum response profile was obtained and then multiplied by $\sqrt{2}$.

Rayleigh damping, represented mathematically by

$$\mathbf{C} = a_0\mathbf{M} + a_1\mathbf{K} \tag{3.1}$$

where $\mathbf{C}$ is the turbine damping matrix, $\mathbf{M}$ is the mass matrix, $\mathbf{K}$ the stiffness matrix, and a_0 and a_1 are coefficients to be determined, was used in the wind turbine model to account for all the dissipative effects. This was done for simplicity and because it would maintain the linearity of the system (Charney, 2008). Here, a good self-checking method was to set the damping parameters to zero. A truly resonant behavior in this situation would yield the amplitude of acceleration at some point on the tower that would grow boundlessly. This was indeed the case for all three tower modes in both directions. Since the applied signal had only one frequency of excitation, it was chosen to further simplify the employed Rayleigh damping model to mass proportional damping only (by setting $a_1 = 0$). For this particular case, then, the observed tower acceleration would only depend on a single parameter, a_0, decreasing simulation time (Charney, 2008). Thus the exercise was reduced to varying the coefficient that multiplies the mass matrix until the numerical model exhibits similar amplitudes to those seen on the experiment. The corresponding damping was then treated as the modal damping associated with the wind turbine.

Table 3.1: Some properties of the tower and blades of a 900 kW wind turbine (source: Prowell, 2010)

Tower Property	Location		
	Bottom	Middle	Top
Average Outside Diameter [m]	3.24	2.66	2.05
Average Wall Thickness [cm]	2.2	1.9	1.25
Average 2nd Moment of Area [m^4]	0.26	0.13	0.04
Average Linear Mass Density [kg/m]	1,800	1,300	650
Blade Property	**Location**		
	Root	Middle	Tip
Average Flap 2nd Moment of Area [m^4]	0.012	1.5×10^{-3}	1.7×10^{-4}
Average Edge 2nd Moment of Area [m^4]	0.023	6.3×10^{-3}	1.2×10^{-4}
Average Linear Mass Density [kg/m]	900	540	195

Table 3.2: Comparison between the experimental natural frequencies and those predicted from the numerical model. (source: Prowell, 2010)

Bending Mode	Experimental Frequency [Hz]	Numerical Frequency [Hz]
1^{st} Fore-aft	0.55	0.57
1^{st} Side-to-side	0.54	0.57
2^{nd} Fore-aft	3.95	3.90
2^{nd} Side-to-side	3.90	3.88
3^{rd} Fore-aft	8.73	10.65
3^{rd} Side-to-side	11.05	11.13

Portions of the response arrays from the numerical model for all the normal modes in question have been plotted in Figures 3.1-3.6 and are meant to demonstrate the agreement with the experimental motion across multiple tower elevations using this method (compare with Figures 2.10-2.15). For the best correspondence, these motions are taken from the finite-element nodes that were closest to locations of the accelerometers in the full-scale experiment. All the simulations were performed using the respective damping listed in Table 3.3.

Notice that fore-aft modes have response mostly in the fore-aft direction and side-to-side modes in the side-to-side direction. Responses in the perpendicular horizontal direction of shaking are negligible in the model to a very high degree (the response here is $< 10^{-10}$). This is simply because the simulation was conducted with one-directional shaking.

Also worthy of mention is that there is some discrepancy between the amplitudes in the third bending modes in the numerical simulation compared to their counterparts from the experiment. This may be the result of some very slight difference in the elevation of a node in the numerical model producing a noticeably different response or that this type of a model might need some further refinement to reproduce the relative ratios associated with the modes more closely.

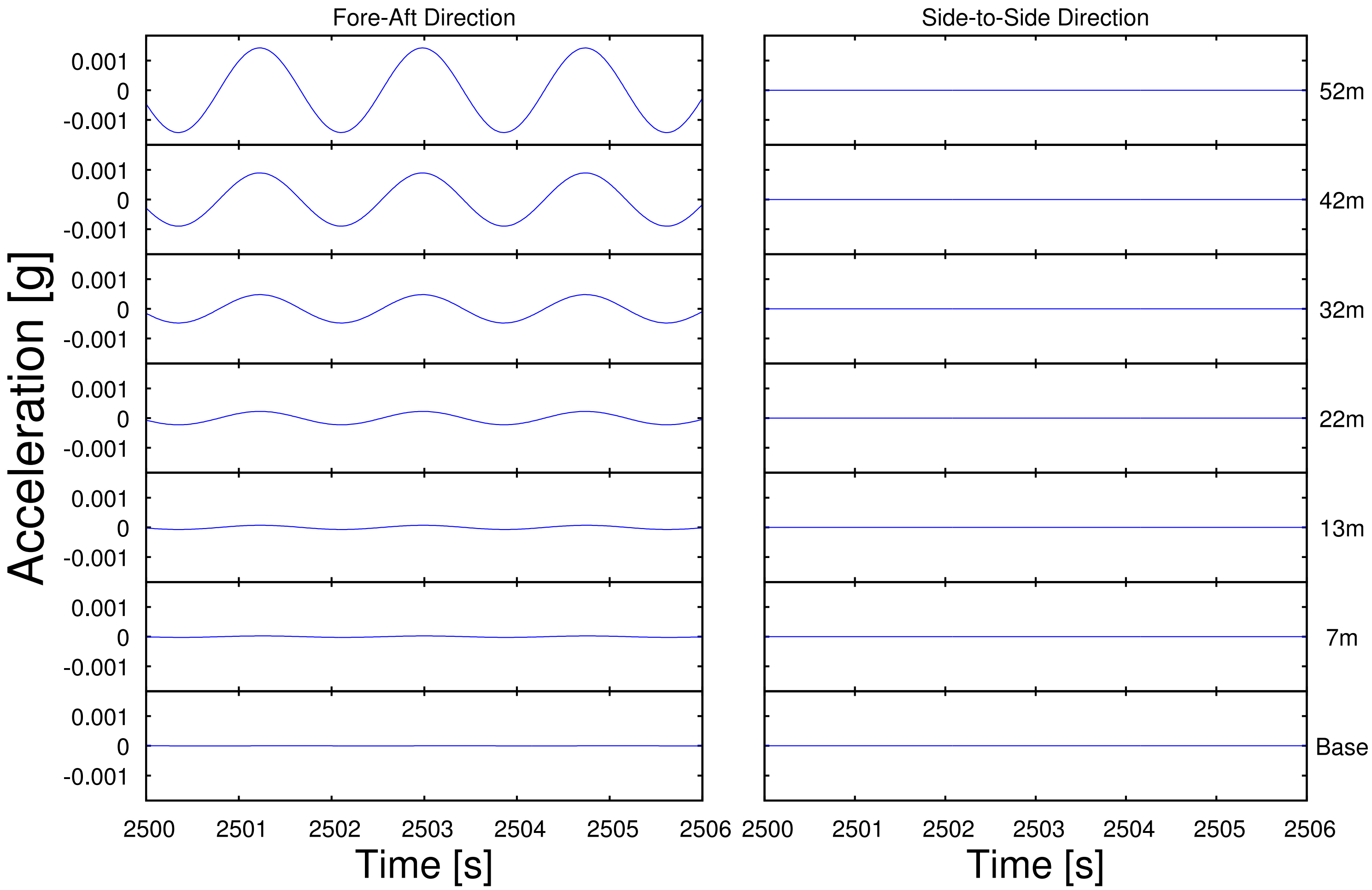

Figure 3.1: Steady-state numerical response for the 1st fore-aft bending mode.

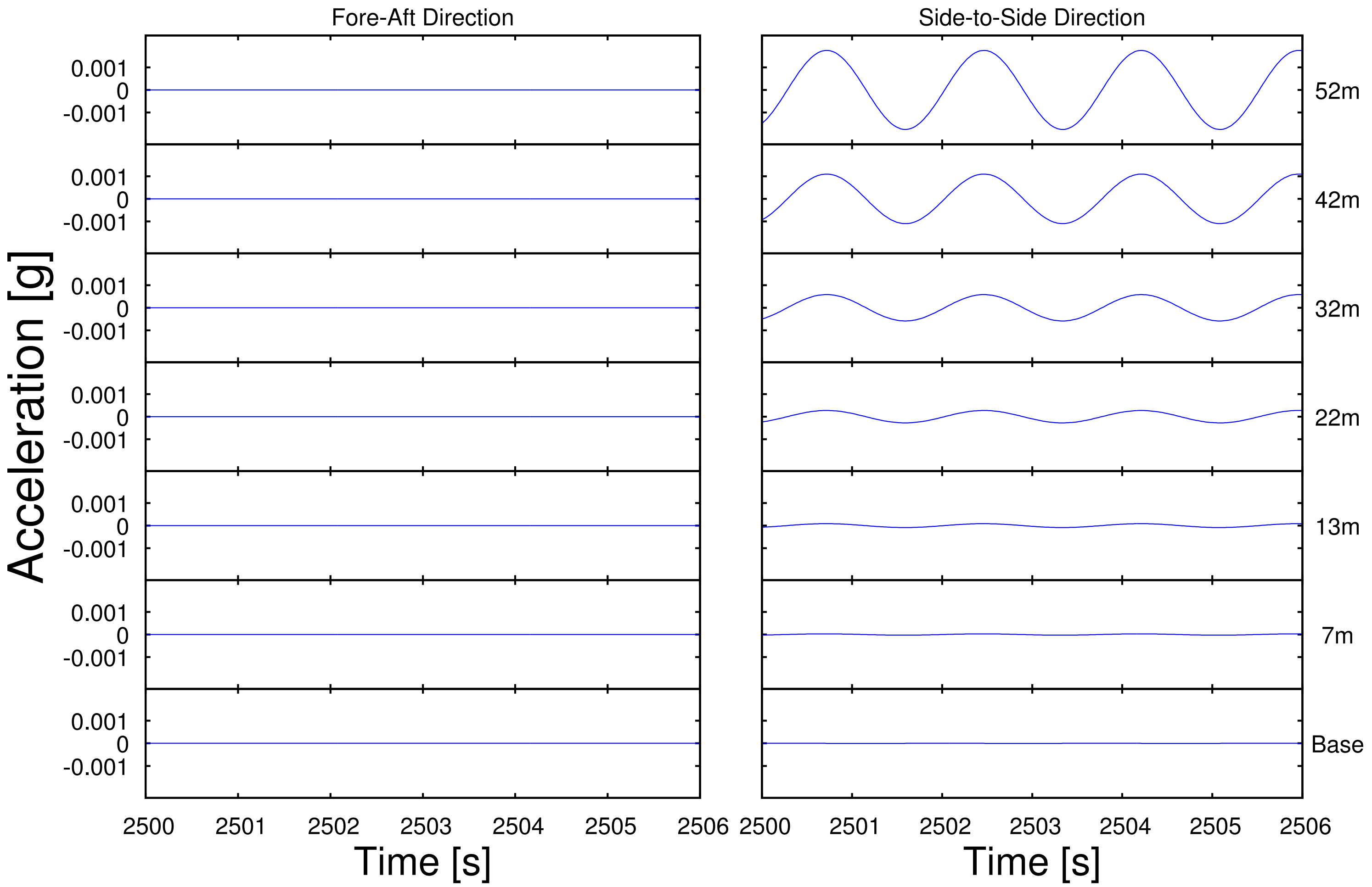

Figure 3.2: Steady-state numerical response for the 1st side-to-side bending mode.

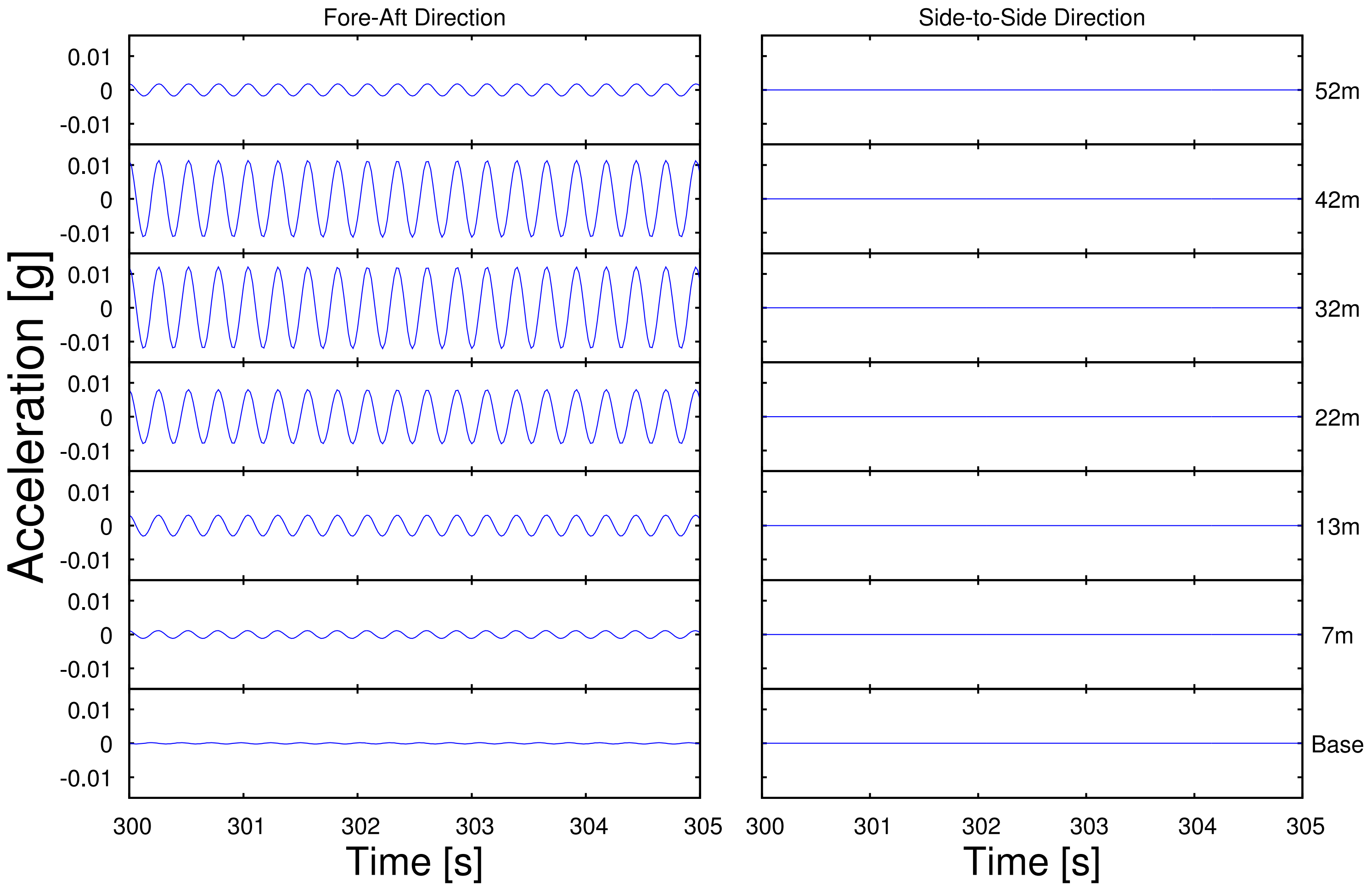

Figure 3.3: Steady-state numerical response for the 2^{nd} fore-aft bending mode.

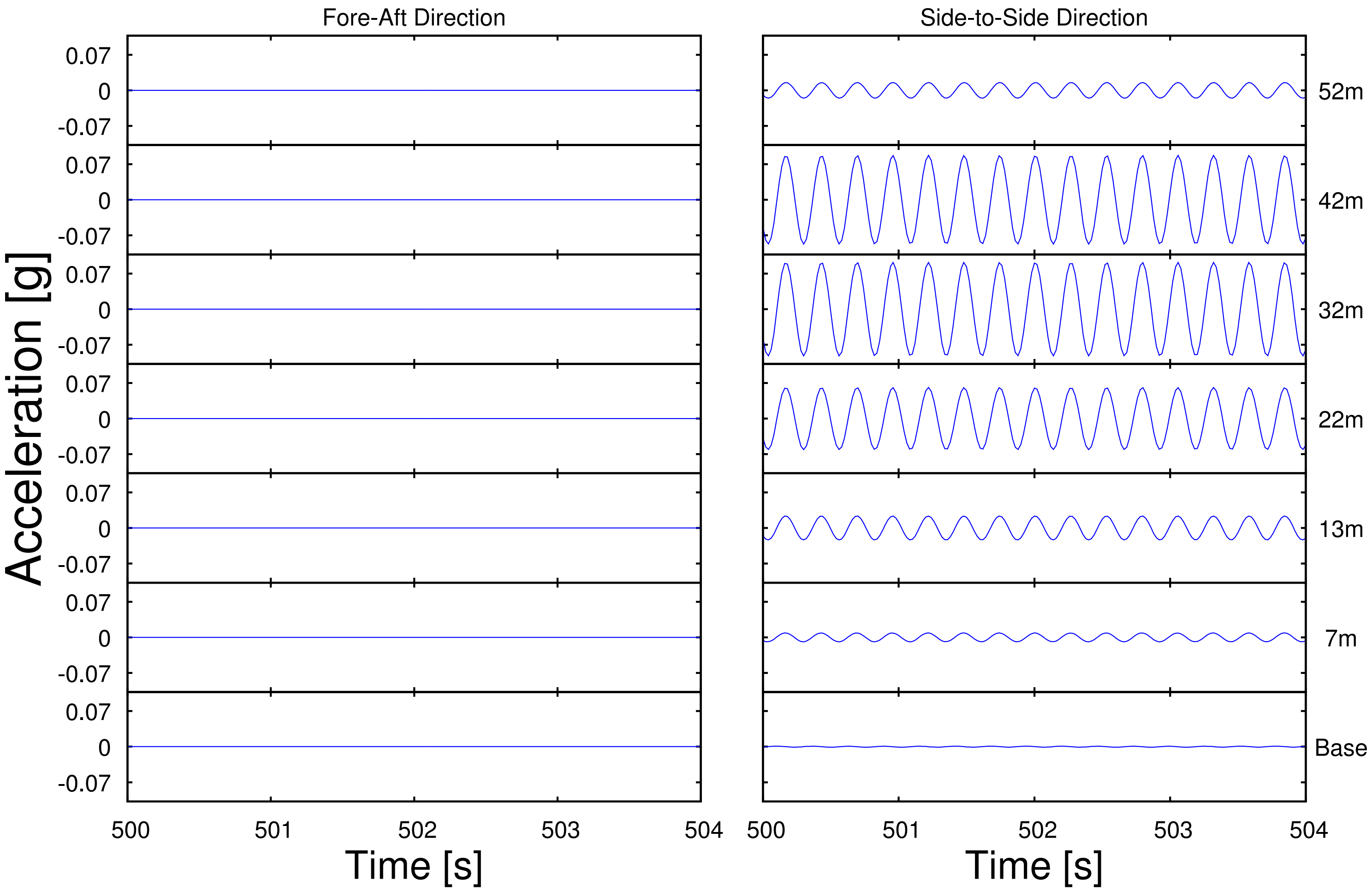

Figure 3.4: Steady-state numerical response for the 2^{nd} side-to-side bending mode.

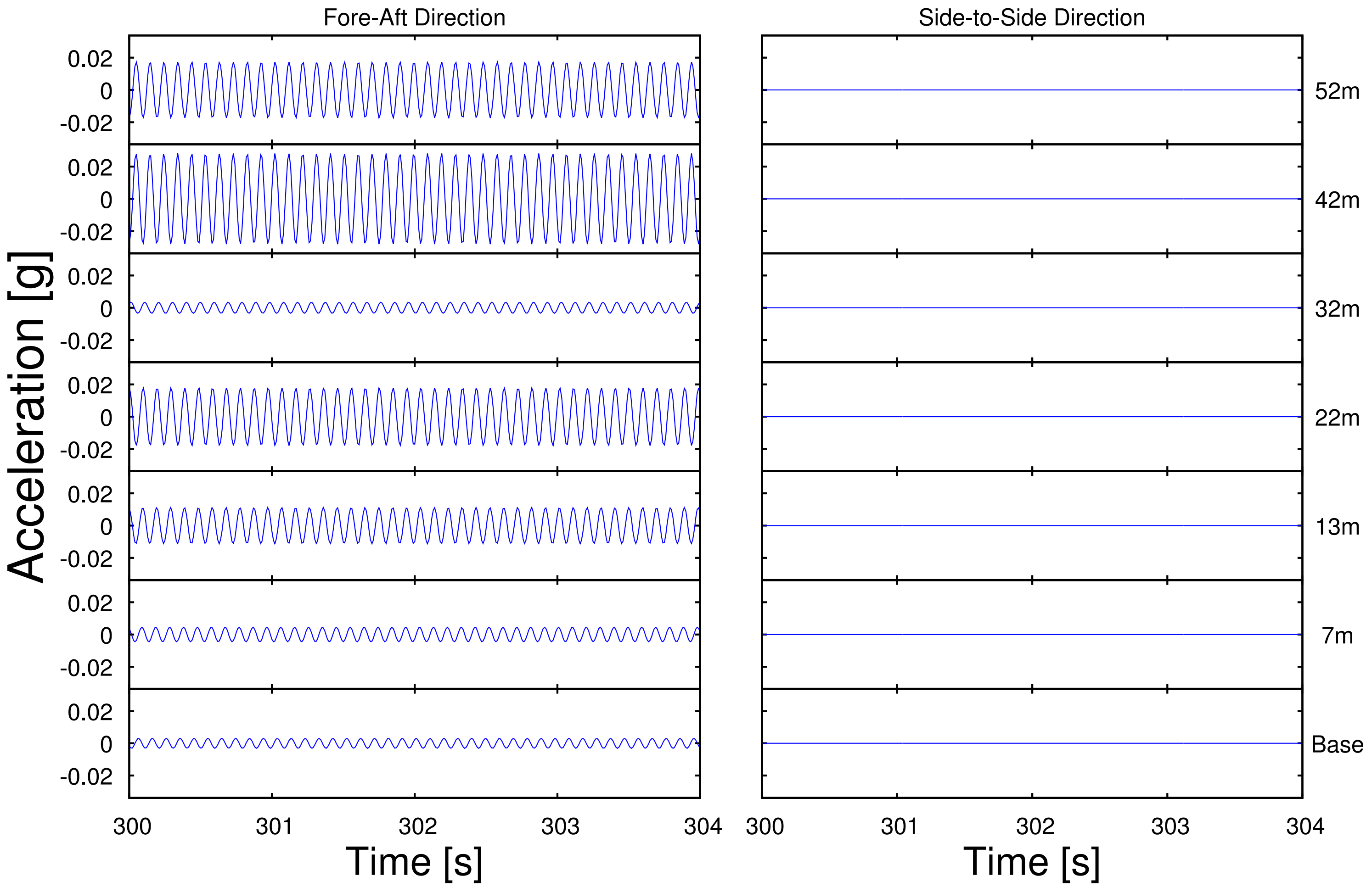

Figure 3.5: Steady-state numerical response for the 3^{rd} fore-aft bending mode.

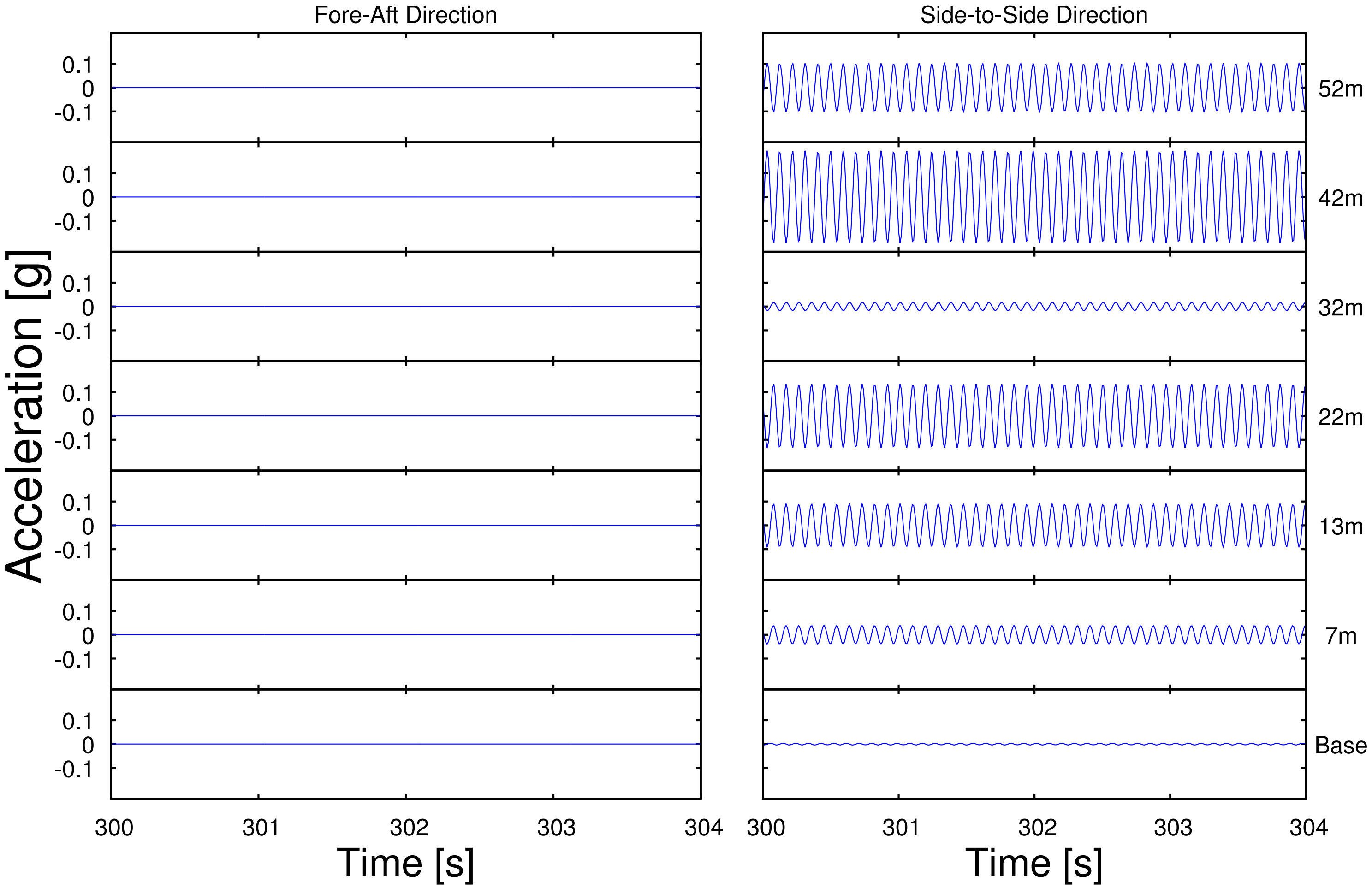

Figure 3.6: Steady-state numerical response for the 3$^{\text{rd}}$ side-to-side bending mode.

3.3 Damping Results and Commentary

Using the above method, the modal damping values in Table 3.3 were obtained. A glaring issue with these results is, however, observed in the first fore-aft and the first side-to-side modes. Although structural damping is typically considered to be on the order of a few percent, these two modes exhibit the damping on the order of 1/100 of this value. An attempt will be made to provide a satisfactory explanation on why the damping estimates for the first bending modes are so poor. Further discussion is provided in Appendix B.

The implementation was straightforward and somewhat simplistic. First, define the maximum base signal as

$$\ddot{U}_{g0} = \max_{\substack{i=1,2 \\ 1 \le k \le n}} \left| \ddot{U}_{i0k} \right| \tag{3.2}$$

(notice that $j = 0$, corresponding to elevation $= 0$, see Chapter 2). Observing some of the filtered time series of Chapter 2 (see Figures 2.10-2.15), the response ratio, R, is formed as

$$R \equiv \frac{\ddot{U}_{mnp}}{\ddot{U}_{g0}} \tag{3.3}$$

where $\ddot{U}_{mnp}$ has the same definition as in Section 2.4. This R factor reached almost as high as 1,000 in some cases, particularly in the first fore-aft and first side-to-side bending modes. This is evidenced by the fact that when they were plotted on the same scale, the input recorded motion is hardly visible compared to the response towards the higher elevations of the tower. In the simple analysis of a single-degree-of-freedom oscillator (SDOF) subject to harmonic excitation it has been analytically shown that the response ratio is also given by

$$R = \frac{1}{\sqrt{(1-\beta^2)^2 + (2\xi\beta)^2}} \tag{3.4}$$

where $\beta \equiv \tilde{\omega}/\omega$, the ratio of the driving frequency of oscillator to that of the natural frequency and ξ is the damping ratio (see Vierck (1979)). Resonant behavior occurs at $\beta \approx 1$, reducing the above formula to

$$R \approx \frac{1}{2\xi}$$

Table 3.3: The estimated modal damping.

	Apparent Damping [%]	
Bending Mode	Fore-aft	Side-to-side
1	0.08	0.06
2	0.6	0.4
3	2.4	0.4

or

$$\xi \propto \frac{1}{R}$$

Hence a (very) rough estimate of the damping at resonance is simply to take the inverse of the response ratio. For a response ratio of 1,000, the expected damping ratio should be about 0.001 (or 0.1%) (Chopra, 1980; Vierck, 1979). Indeed, after running the simulation and taking the response ratio, the simulation that best approximates the filtered experimental measurements is of this order of magnitude.

Given that the analysis of the experimental measurements yielded results that are consistent with the simplified, theoretical approximation, yet distinct from reality, a person might be inclined to question the validity of the experiment itself or in the methodology of the analysis. For those types of inquiries, the author offers an explanation resulting from the nature of the shaker excitation. Recall that Figure 2.7 revealed that for small frequency values, the shaker imparts minuscule forces. In effect, much of the response that is measured at such low frequencies would either be the result of ambient noise (clearly visible in Figures A.1 and A.2) or the response due to effectively ambient vibration (for which Prowell (2010) offers a more rigorous treatment on how to best obtain modal parameters). For interested readers, some further explanation for the error is offered in Appendix B.

In the higher modes, the larger frequency values were, however, able to return more reliable estimates of damping ratios. In support of this claim, the author wishes to return the readers' attention to the ambient vibration study featured in Prowell (2010). Using methods that analyzed output only responses the wind turbine, that study obtained the modal damping values found in Table 3.4. Not surprisingly, the results for the first fore-aft and side-to-side modes contrast

Table 3.4: Modal damping estimates from Prowell (2010).

Mode	Apparent Damping [%]	Standard Deviation [%]
1st Fore-aft Bending	4.0	1.4
1st Side-to-side Bending	3.4	1.2
2nd Fore-aft Bending	0.9	0.4
2nd Side-to-side Bending	1.0	0.5
3rd Fore-aft Bending	1.8	0.7
3rd Side-to-side Bending	0.7	0.4

heavily with those presented here. The same methods used on the higher tower modes do, however, have some agreement. For instance, Prowell (2010) estimates the modal damping for the third fore-aft mode as 1.8%, while this study predicted that this value should be about 2.4%. Being that it is inherently difficult to obtain a measurement of damping accurately, as is reflected in the large standard deviations present in the table, this represents reasonable agreement. The second fore-aft and the third side-to-side bending modes also appear to have modal damping values within reasonable proximity to those measured by Prowell (2010). In effect, it appears that at some frequency between 0.5 and 4.0 Hz, the driving force of the shaker is large enough that any residual noise or ambient vibrations do not seriously affect the measurement of modal damping if conducted in a manner consistent with this approach. In summary, with a good finite element model, a researcher can use experimental data to simulate resonance behavior and thus obtain an estimate of modal damping if the shaker is imparting enough force to overcome ambient vibration and noise.

3.4 Remarks on the Half-Power Method

This section is intended to give the reader a brief overview on the more generally accepted half-power method for finding damping ratios and accompany it with some preliminary results as it concerns the acceleration time histories used. The outcomes are intended to provide a crude estimate using this method and to compare with the previous results.

Given a time history and bounds for a frequency range expected to contain a natural frequency, the employed algorithm created a transfer function using the signal at the base and comparing it to all others at various elevations. It would then find a local maximum $\tilde{\ddot{U}}$ within the upper and lower frequency bounds. The tilde on this quantity is just meant to emphasize that it is the result of an operation that creates the transfer function of $\ddot{U}$. This quantity is also the maximum recorded amplitude of all the accelerometer elevations. The frequency at which $\tilde{\ddot{U}}$ occurs is taken to be the natural frequency f_n. Following this logic, the identified natural frequencies are displayed in the second column on Table 3.5. The half-power frequency band is then found by calculating the quantity $\frac{1}{\sqrt{2}}\tilde{\ddot{U}}$ and finding the two frequencies closest to f_n that correspond tho this value. Their absolute difference is called the frequency band, Δf. Once these quantities are obtained, the damping ratios can be calculated as

$$\xi_n = \frac{\Delta f}{2 f_n} \tag{3.5}$$

for all the natural frequencies (Chopra, 1980). The results of this calculation are shown in the third column of Table 3.5.

Table 3.5 shows that the natural frequencies of the 2nd fore-aft and side-to-side modes as well as the 3rd fore-aft mode reasonably agree with those values previously presented by the author. Additionally the 3rd fore-aft mode experienced a damping ratio similar to that seen in Prowell (2010). The damping ratio measured for the second side-to-side bending mode is slightly larger using the half-power method, but is comparable.

Table 3.5: Natural frequencies and damping ratios found in the half power method.

Mode	Natural Frequency [Hz]	Apparent Damping [%]
1st Fore-aft Bending	0.488	2.47
1st Side-to-side Bending	0.586	-
2nd Fore-aft Bending	4.004	-
2nd Side-to-side Bending	3.942	0.65
3rd Fore-aft Bending	8.752	1.84
3rd Side-to-side Bending	11.230	-

On account of the recorded data characteristics from the employed data sets, the results obtained from the half-power method are limited in their ability to adequately shed light on the modal damping. The 2nd fore-aft and 3rd side-to-side modes had unusually small damping ratios that were therefore discarded. This appears to be the result of spikiness in the transfer functions and a very narrow half-power frequency band. The segments of data at hand were essentially of the "dwell" type, which severely hampered the execution of the half power damping estimation technique. Other segments of the recorded data might contain frequency sweeps at these bands which would permit the estimation of a more representative damping for these modes (please see the NEEShub repository).

In addition, it was decided not to include an estimate in Table 3.5 of the first side-to-side mode using this method. The reason for this is explained by Figure 3.7. There did not seem to be a strong, definite peak in the general area where the natural frequency was expected. Instead, there is just some curvature overshadowed by surrounding spikes. It was felt that applying the half-power method in this situation would not be very meaningful. Part of the problem might have been that the length of the transfer function signal, which is proportional to the length of the original response, was not very large for the amount of sampled frequencies. Hence, the frequency spectrum is very coarse in this record, which limits its accuracy. Secondly, as alluded to earlier, the shaker forcing was made insignificant because most of the measured response was likely due to ambient wind loading.

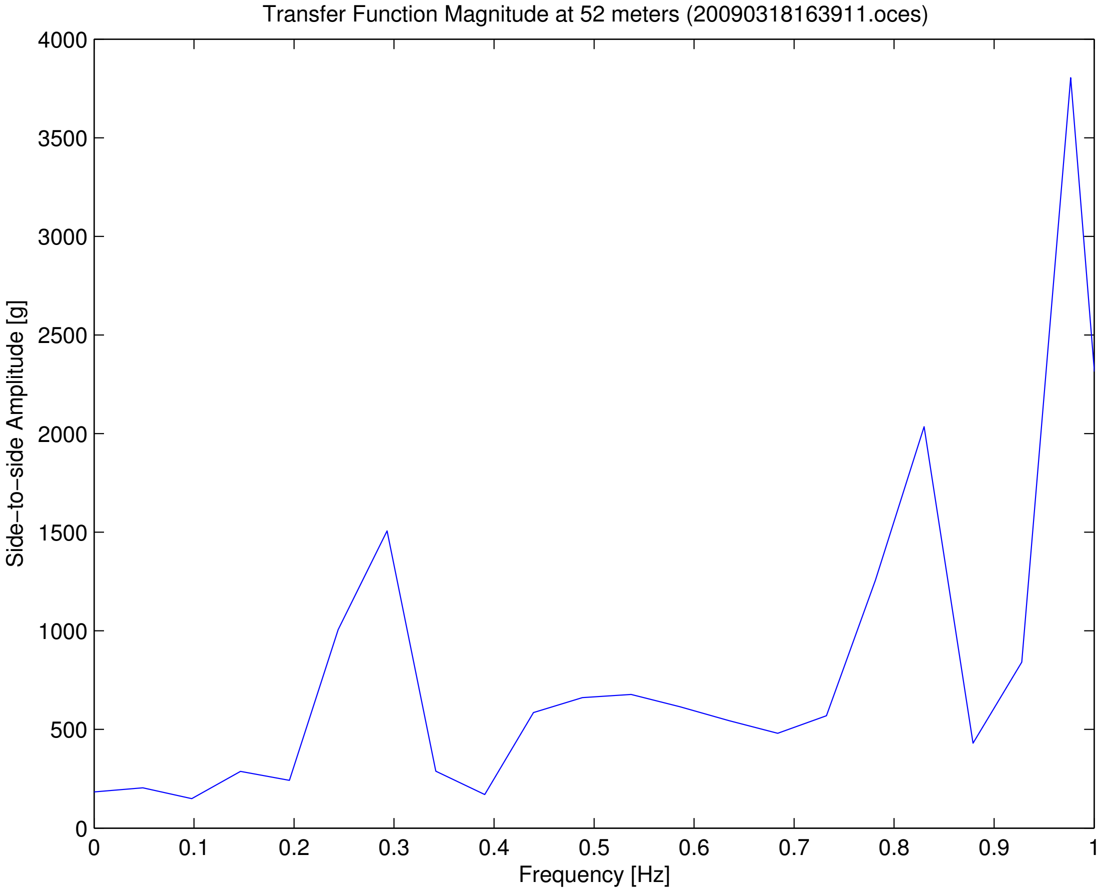

Figure 3.7: Transfer function amplitude in the vicinity of the first natural frequency.

Bibliography

Bazeos, N., Hatzigeorgiou, G. D., Hondros, I. D., Karamaneas, H., Karabalis, D. L., and Beskos, D. E. (2002). "Static, seismic and stability analyses of a prototype wind turbine steel tower". *Engineering Structures*, 24(8):1015–1025.

Charney, F. A. (2008). "Unintended Consequences of Modeling Damping in Structures". *Journal of Structural Engineering, ASCE*, 134(4):581–592.

Chopra, A. K. (1980). *Dynamics of Structures a Primer:*. Earthquake Engineering Research Institute, 2620 Telegraph Avenue, Berkeley, California 94704.

Mazzoni, S., McKenna, F., and Fenves, G. L. (2006). *Open System for Earthquake*

Engineering Simulation User Manual. Pacific Earthquake Engineering Research Center, Berkeley, California, United States.

Prowell, I. (2010). *An Experimental and Numerical Study of Wind Turbine Seismic Behavior.* PhD thesis, University of California, San Diego.

Prowell, I., Veletzos, M., Elgamal, A., and Restrepo, J. (2009). "Experimental and Numerical Seismic Response of a 65 kW Wind Turbine". *Journal of Earthquake Engineering*, 13(8):1172.

Risø (2002). *Guidelines of Design of Wind Turbines.* Det Norsk Veritas, Copenhagen and Wind Energy Department, Risø National Laboratory, Copenhagen, Denmark.

Vierck, R. K. (1979). *Harmonically Forced Vibrations for Single-Degree-of-Freedom Systems*, chapter 4, pages 90–147. Vibration Analysis. Harper and Row, New York, N.Y., second edition.

Chapter 4

Simple Estimates of Soil-Structure Interaction Mechanisms

The finite-element model from Chapter 3 is extended here in Chapter 4 so as to have the base supported by linear springs. The method used by the author to assign a stiffness to the each spring is described and the results are presented and analyzed.

4.1 Motivation

As in Chapter 3, this chapter will make use of the OpenSees numerical model and measured time history data from the experiment to extract relevant information. In the previous analysis intended to identify the natural frequencies and damping ratios, the actual recorded lateral base excitation was applied to the model. In this chapter, however, attention is focused on the recorded base translation and rotation. As an example, the reader is directed to Figure 4.1. These quantities, measured directly at the base using tri-axial accelerometers, are employed to deduce a base translational and rotational spring for each model by matching the observed overall system resonse for each mode.

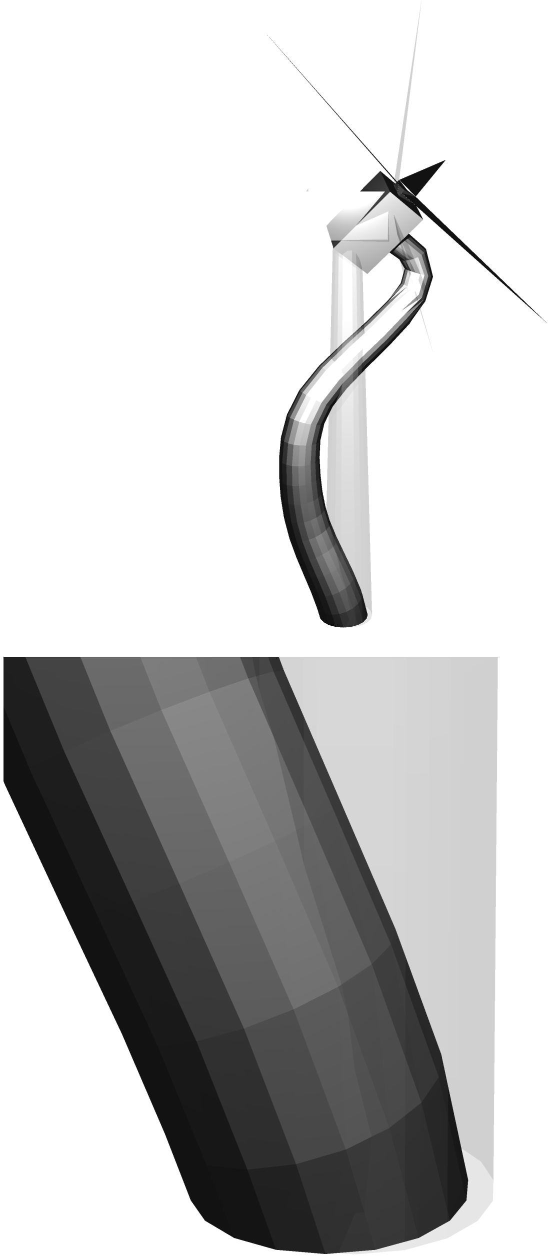

Figure 4.1: Top: 3^{rd} fore-aft mode versus a reference turbine (transparent). Bottom: detail of the base acceleration.

4.2 Influence of Soil-Structure Interaction on the Wind Turbine Model

Accounting for these effects rigorously, however, requires a knowledge of soil-structure interaction formalism, the material properties of the soil, the geometry and mass of the structure's foundation, and usually requires some further numerical methods to estimate the motion, especially if the aforementioned foundation geometry is not simple (Apsel and Luco, 1987; Luco, 1986). Another, conceptually simpler approach, which has been applied to other wind turbine structures, is to use linear springs to encompass any flexibility present in the soil (Bazeos et al., 2002; Zhao and Maißer, 2006). This simpler approach has been adopted by the author for clarity. A further assumption was made that the motion of the base of the wind turbine can be represented accurately by using a coupled horizontal-translation, rocking-rotation model. That is, the effects of rigid-body translation in the vertical direction were neglected.

Bazeos et al. (2002) and Zhao and Maißer (2006) referenced other publications in their works citing formulae which guided them as to how stiff to make their springs. A sample of the magnitudes of the spring constants used in Bazeos et al. (2002) is found in Table 4.1. Those authors used two different foundations designs ($10 \times 10 \times 1.8\,\mathrm{m}^3$ and $12.5 \times 12.5 \times 1.8\,\mathrm{m}^3$ concrete blocks) and thus there are two sets of calculations reported. For this part of the study, the data from the experiment described in Chapter 2 is employed along with a finite element model and used to back calculate values for these springs. The findings presented in that chapter, specifically the mode shapes and the natural frequencies are used to establish the associated base spring stiffness values.

As alluded to earlier, it was desired to make use of the experimental data to determine the spring constants of the soil around the wind turbine for each of the known tower modes. The instrumentation of the experiment had already made available the data of the wind turbine at the four locations of the base in each of the three orthogonal directions. For further clarity, the reader is directed to Figure 2.4. Plan view Ⓐ of that figure shows that at base level, the accelerometers were placed in a cross formation. Every point marked with a roman numeral in that view had an accelerometer measuring motion in all three spatial directions. At this point, it is convenient to adopt an array similar to the response array used in Chapter 2. Let

$$\ddot{\mathbf{B}}(t) = \left[\ddot{\vec{u}}_{\mathrm{I}}(t) \quad \ddot{\vec{u}}_{\mathrm{II}}(t) \quad \ddot{\vec{u}}_{\mathrm{III}}(t) \quad \ddot{\vec{u}}_{\mathrm{IV}}(t) \right]$$

where the roman numeral subscripts refer to the same locations in seen in Figure 2.4 for base level acceleration. In this case, the individual vectors have three components, fore-aft, side-to-side, and vertical. If $r = 1, 2, 3 =$ fore-aft, side-to-side, vertical, $s = \mathrm{I}, \mathrm{II}, \mathrm{III}, \mathrm{IV}$, which for notational convenience will be referred to as $\{s\}$, and the time domain is discretized as before, $t \to t_k$, and the array becomes three dimensional. This array can is represented as

$$\ddot{B}_{rsk} \equiv \ddot{B}_{rs}(t_k) \tag{4.1}$$

For the purposes of communication, the array will be referred to as the base response array.

The base response array was filtered for each direction and location on the base using the same methods that were employed in Chapter 2 to obtain the standard response array. Let p be the index that refers to the time t_p and denotes when the maximum response profile $\ddot{\mathbf{U}}^{max}$ occurs. It is the same index p as that of Equation (2.2). For consistency with the development of the mode shapes, the base acceleration was taken at the same instant of time t_p as that used for imaging the mode shapes in Figures 2.16-2.21. This excitation was used as a “target” acceleration that was sought to be reproduced. In other words, given this index p, the maximum base response profile $\ddot{\mathbf{B}}^{max}$ associated with the maximum response profile $\ddot{\mathbf{U}}^{max}$ is formed with the following entries

$$\ddot{B}^{max}_{rs} = \ddot{B}_{rsp} \tag{4.2}$$

The situation then becomes one of reproducing the maximum response profile and the associated maximum base response profile acceleration in the numerical model. Since in the OpenSees environment it is very easy to specify a displacement, a simple method of implementation can be obtained when realizing that

Table 4.1: Spring constants reported in Bazeos et al. (2002).

	Spring Constant ($10 \times 10\,\mathrm{m}^2$)	Spring Constant ($12.5 \times 12.5\,\mathrm{m}^2$)
Horizontal	$1.41 \times 10^7\,\frac{\mathrm{kN}}{\mathrm{m}}$	$1.76 \times 10^7\,\frac{\mathrm{kN}}{\mathrm{m}}$
Rocking	$3.71 \times 10^5\,\frac{\mathrm{kN}}{\mathrm{m \cdot rad}}$	$7.25 \times 10^5\,\frac{\mathrm{kN}}{\mathrm{m \cdot rad}}$

for a shaker imparting a harmonic motion at a single frequency to the base of a wind turbine, the crudest mathematical model that can be assigned to represent the situation is that of a SDOF oscillator. The associated motion is conveniently represented by (fore widely spaced resonant frequencies similar to the case of this wind turbine)

$$\ddot{u} = -\omega^2 u \tag{4.3}$$

where u is the displacement of the oscillator, $\ddot{u}$ the acceleration, and ω the circular frequency as usual (Vierck, 1979). While this mathematical model may be simple, it may provide some insight by relating the displacement of say the turbine tower as differing from the measured acceleration only by a factor of $-\omega^2$. At worst, information derived on the stiffness of the springs used to represent the soil would give an order of magnitude estimate of the net soil-structure interaction. Hence the following was extrapolated

$$\ddot{\mathbf{U}}^{max} = -\omega^2 \mathbf{U}^{max} \tag{4.4}$$

$$\ddot{\mathbf{B}}^{max} = -\omega^2 \mathbf{B}^{max} \tag{4.5}$$

Note that $\mathbf{B}^{max}$ will frequently be referred to as the orientation of the base. Evidently the response arrays, which were given in terms of acceleration, were then easily converted to displacements by a simple division and then assigned to the positions of the respective accelerometers. The $\mathbf{B}^{max}$ array was the important quantity used as a reference by which the stiffness in the springs would be calibrated (described subsequently).

In order to capture the specific motion measured by the accelerometers in the experiment, the model used in Chapter 3 to estimate modal damping was modified so that the turbine no longer sat on a fixed base (where the input excitation was directly specified), but instead rested on three translational and three rotational linear springs. In OpenSees, this was accomplished by using the `element zeroLength` command with a `uniaxialMaterial Elastic` material tag. In addition, rigid members were added at the base of the numerical model using the `rigidLink` command as a way of connecting the centroid of the model to the outer edge of the radius. They were a useful tool to monitor the base rotation.

With the turbine base free to move as permitted by the linear springs, it was then only a matter of imposing the displacements U_{qj}^{max} on the tower of the turbine model, where $q = 1$ for fore-aft modes and $q = 2$ for side-to-side modes and $j \in \{j\}$, $j \neq 0$. Notice that the tower was only deflected in one direction for any given bending mode and no displacement was specified at the base.

Since the numerical model had a set a four rigid links attached at the base, the most general case would include springs at all six degrees of freedom (fore-aft translation and rocking, side-to-side translation and rocking, vertical translation, and vertical-axis twist). This study will concern itself only with spring values of the coupled horizontal-rocking motion, k_x and k_{θ_y} when for fore-aft motion and k_y and k_{θ_x} when for side-to-side. The rest of the spring constants were kept at very large values so as to be effectively rigid for their respective degrees of freedom. The springs constants associated with coupled horizontal-rocking motion were initially set to very large values and then relaxed until the displacement and slope of the rigid links at the base matched the experimentally measured base orientation in the respective direction. Table 4.2 has been provided summarizing the results using this method. Please note that the directions x, y, θ_x, θ_y refer to the same directions as those used in Ⓐ of Figure 2.4. Figures 4.2-4.7 have been provided for further visual clarity as to how the base was oriented at the conclusion of these tests. Since the goal was to reproduce the translation and rotation of the experimentally measured base in the principle direction of bending only, these plots at instants demonstrate some disagreement in the total vertical direction amplitudes. While this would have been addressed by applying the recorded vertical motion at all employed accelerometer locations, such an effort is beyond the scope of this study. They do match the principle direction of bending, however. This is judged by the fact that ordinates of the edges with eccentricity in the principle direction of bending are approximately the same between the measured experimental values and the simulated numerical values and by the fact that the lines are almost parallel in the principle direction of bending.

The same analysis has also been performed on mode shapes obtained from a set of ambient vibration data on the wind turbine from another study by Prowell (2010). In order to keep some sense of consistency in displaying the base motion data, these modes were rescaled in such a way that the maximum amplitude of deflection was about the same as those used in the shaker driven tests of this thesis. This way, a direct comparison of the results is appropriate. The results for the free-vibration tests are summarized in Table 4.3. Along with this table, the visual representations of the base orientations are provided in Figures 4.8-4.13. These graphs are to be judged in the same manner as their counterparts made fore the forced-harmonic tests. Because the ambient vibration mode amplitudes were provided in normalized form, it was not possible to assess if the difference in deduced spring values observed in Tables 4.2 and 4.3 might be partially due to the corresponding level of deflection. As such, the deduced values in both tables may be representative of ranges for the base spring constants.

4.3 Alternative Equilibrium Approach

It is of interest to pursue another avenue for the estimation of these spring constants for the sake of comparison with Section 4.2. This method would be based on the concept of static equilibrium. Approximating the wind turbine as a

Table 4.2: The approximate soil stiffness constants using the forced-harmonic data.

	Fore-Aft		Side-to-Side	
Bending Mode	k_x $[\frac{\text{kN}}{\text{m}}]$	k_{θ_y} $[\frac{\text{kN}\cdot\text{m}}{\text{rad}}]$	k_y $[\frac{\text{kN}}{\text{m}}]$	k_{θ_x} $[\frac{\text{kN}\cdot\text{m}}{\text{rad}}]$
1	1.20×10^6	1.60×10^8	1.55×10^6	1.48×10^8
2	1.25×10^6	1.24×10^8	2.22×10^6	1.20×10^8
3	1.14×10^6	8.62×10^7	8.50×10^6	2.30×10^8

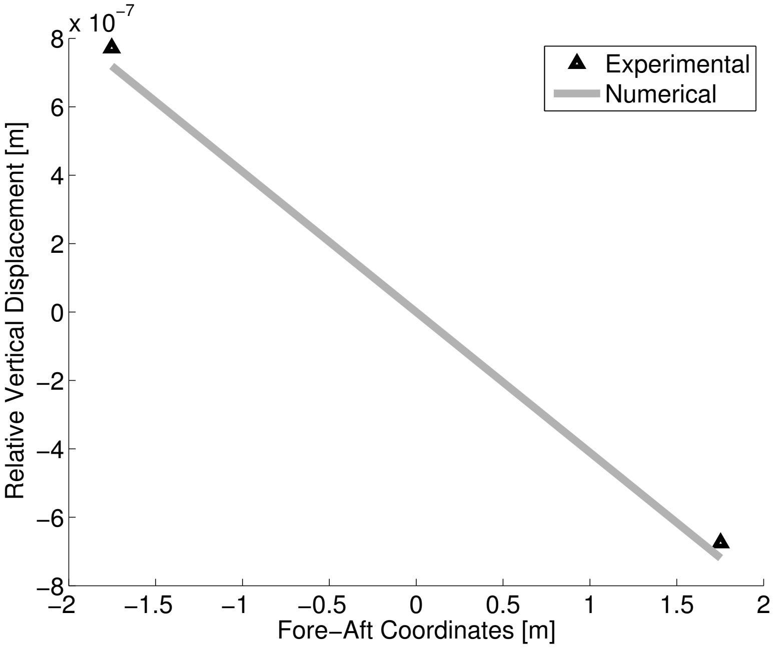

Figure 4.2: Diagram comparing the base orientation for the 1st fore-aft mode (forced-harmonic data set).

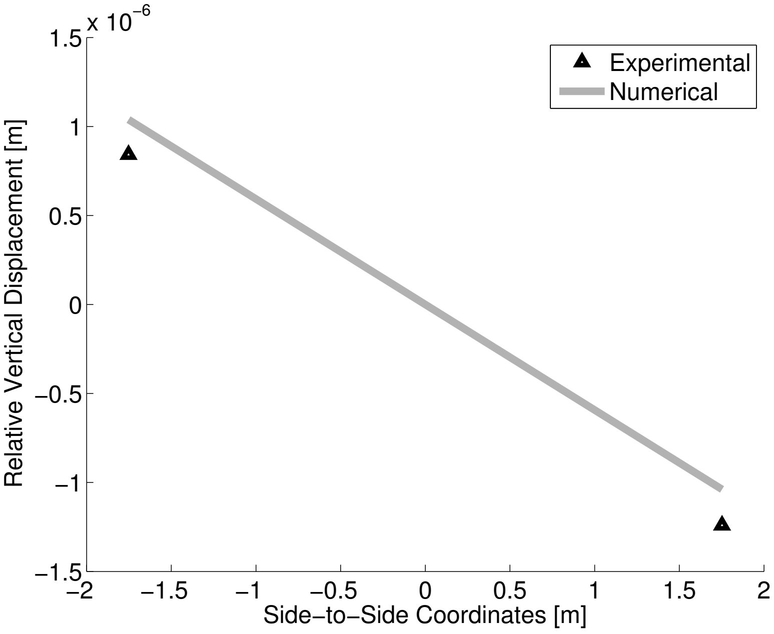

Figure 4.3: Diagram comparing the base orientation for the 1st side-to-side mode (forced-harmonic data set).

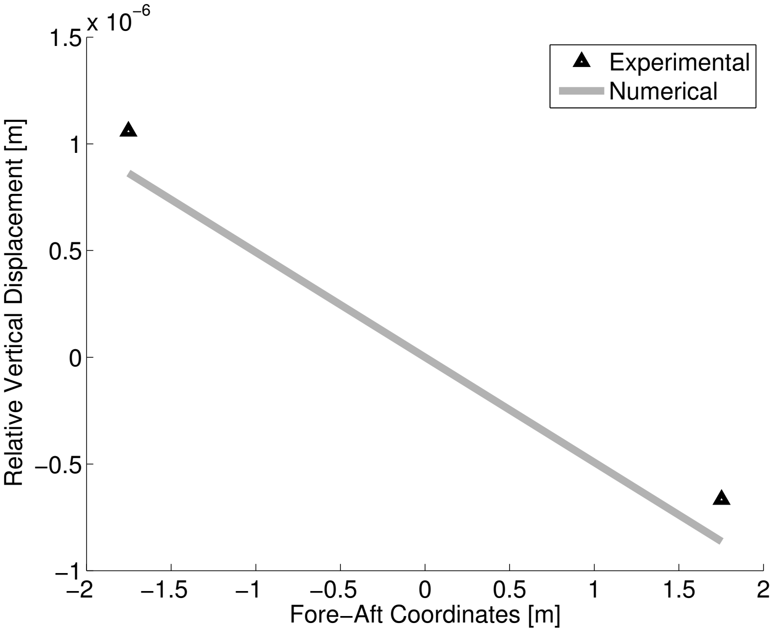

Figure 4.4: Diagram comparing the base orientation for the 2^{nd} fore-aft mode (forced-harmonic data set).

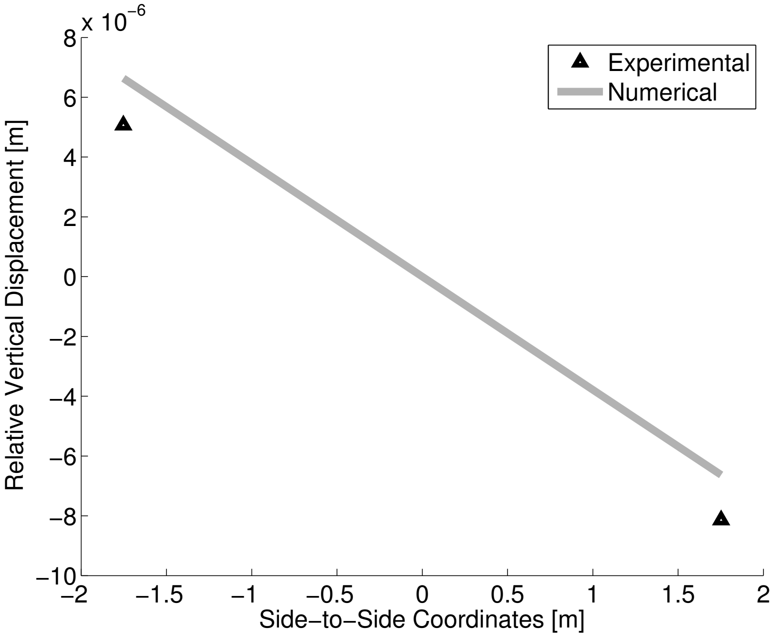

Figure 4.5: Diagram comparing the base orientation for the 2^{nd} side-to-side mode (forced-harmonic data set).

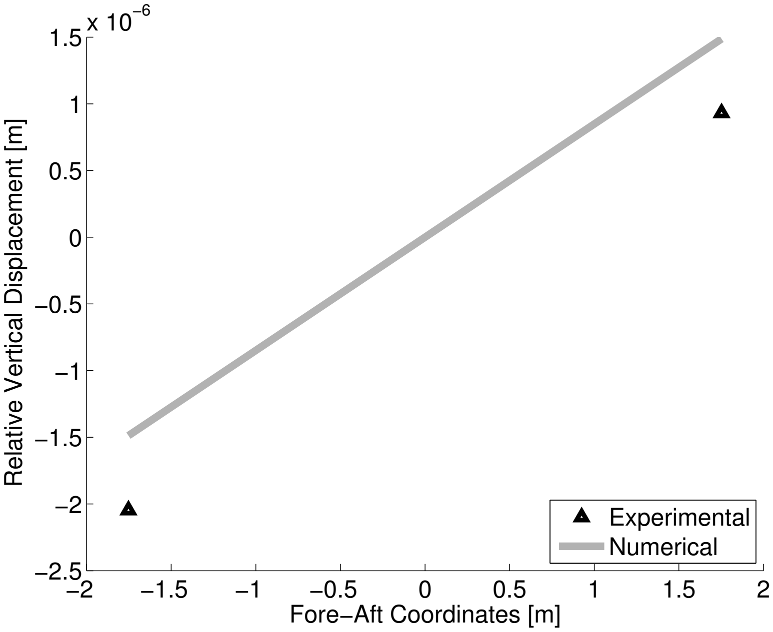

Figure 4.6: Diagram comparing the base orientation for the 3rd fore-aft mode (forced-harmonic data set).

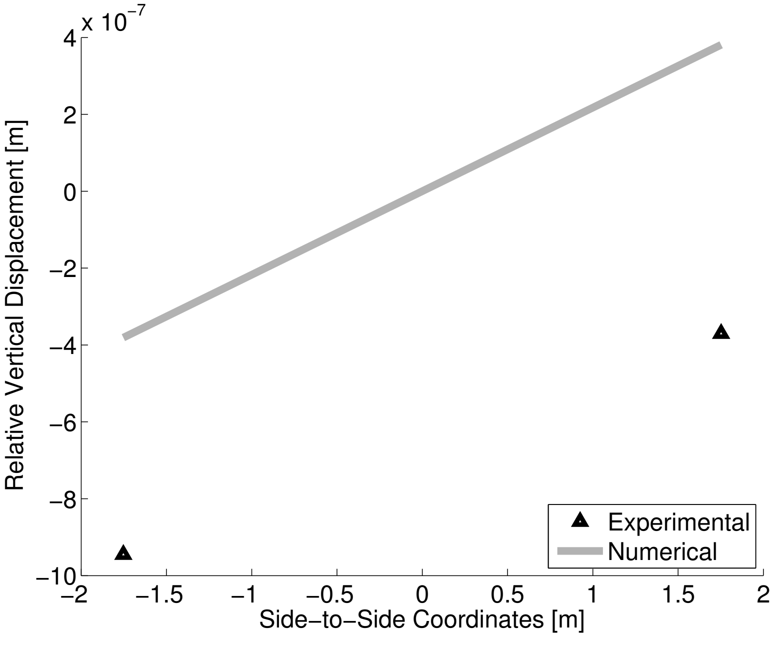

Figure 4.7: Diagram comparing the base orientation for the 3rd side-to-side mode (forced-harmonic data set).

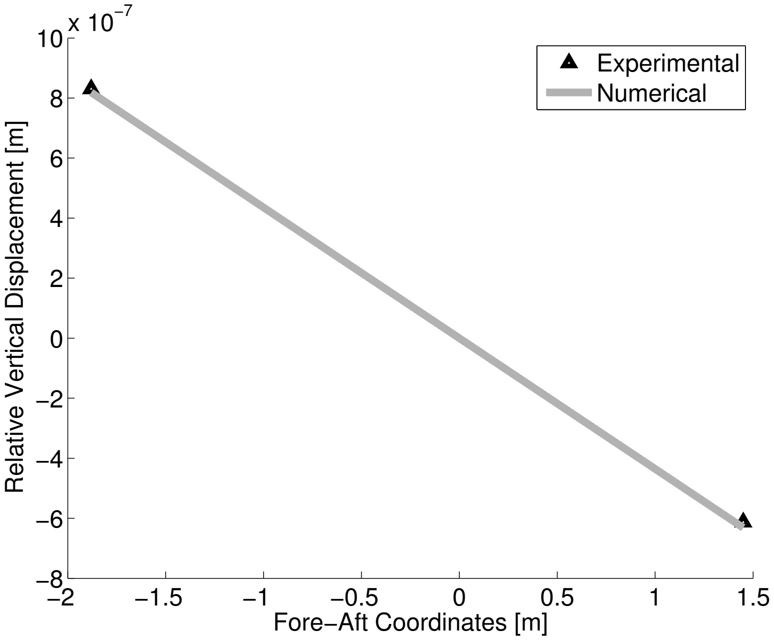

Figure 4.8: Diagram comparing the base orientation for the 1st fore-aft mode (free-vibration data set).

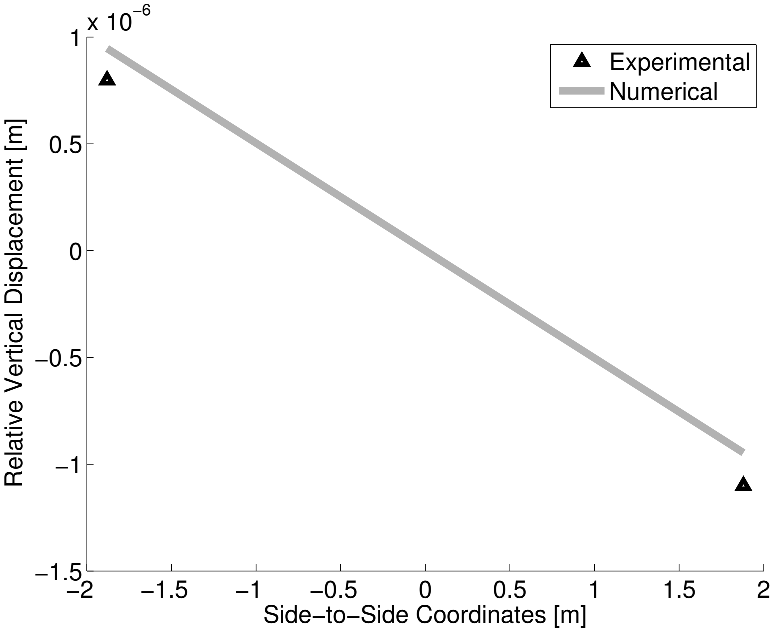

Figure 4.9: Diagram comparing the base orientation for the 1st side-to-side mode (free-vibration data set).

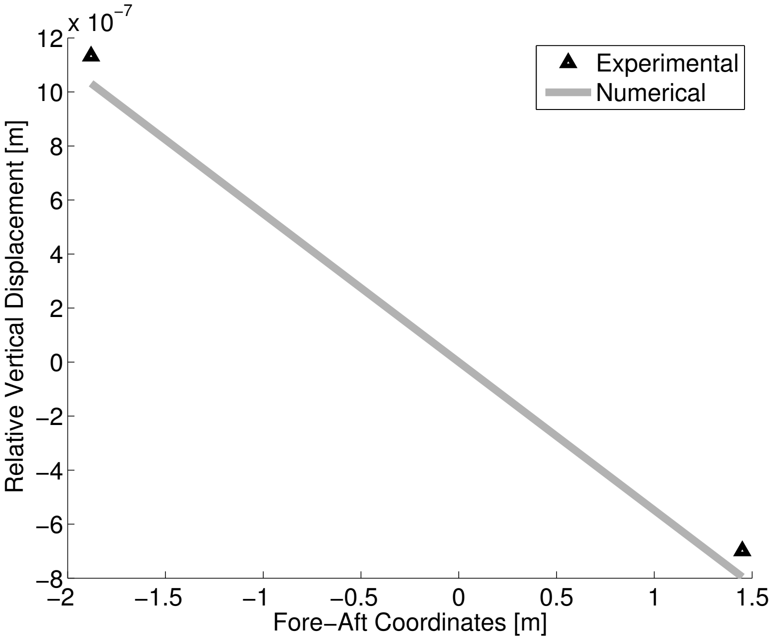

Figure 4.10: Diagram comparing the base orientation for the 2$^{\text{nd}}$ fore-aft mode (free-vibration data set).

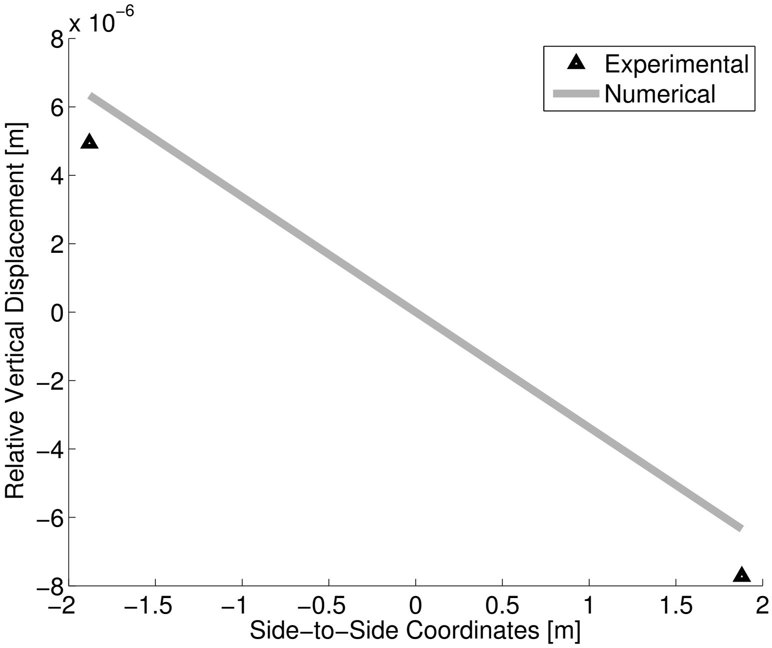

Figure 4.11: Diagram comparing the base orientation for the 2$^{\text{nd}}$ side-to-side mode (free-vibration data set).

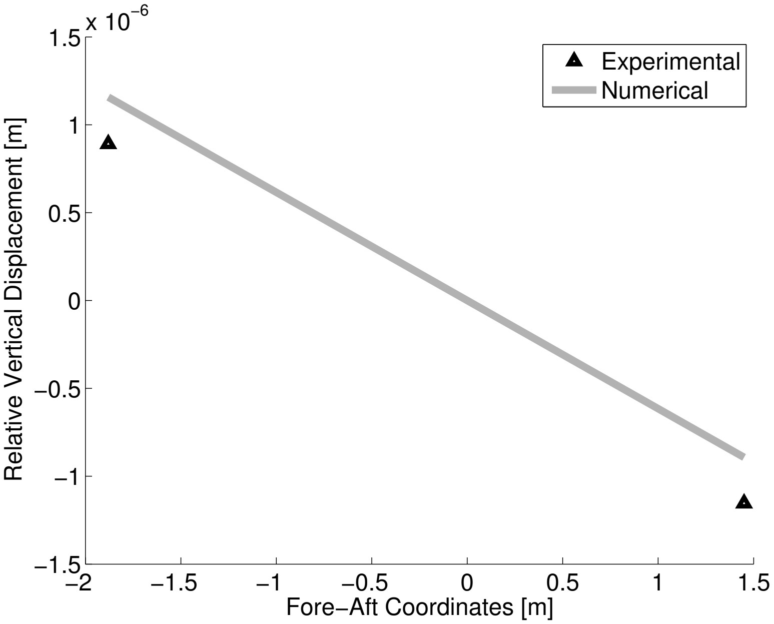

Figure 4.12: Diagram comparing the base orientation for the 3$^{\text{rd}}$ fore-aft mode (free-vibration data set).

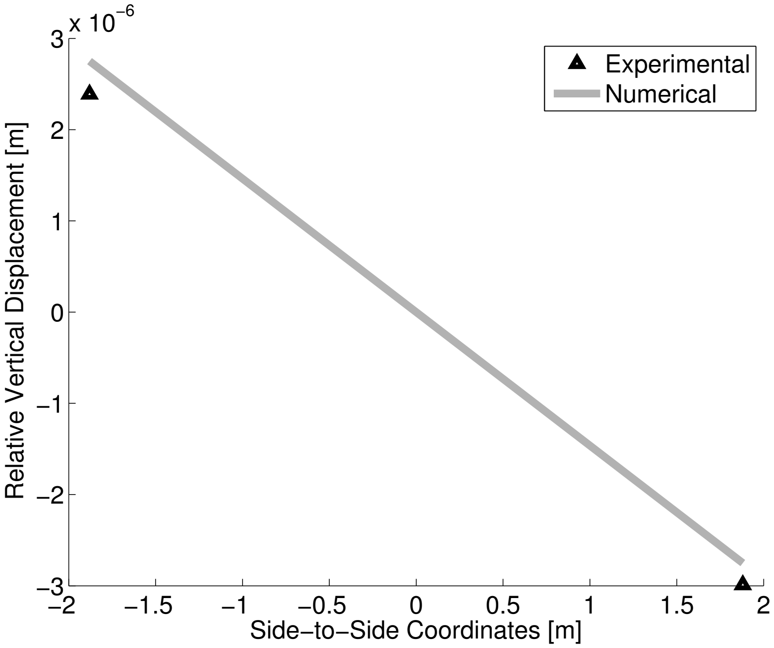

Figure 4.13: Diagram comparing the base orientation for the 3$^{\text{rd}}$ side-to-side mode (free-vibration data set).

Table 4.3: The approximate soil stiffness constants using the free-vibration data.

	Fore-Aft		Side-to-Side	
Bending Mode	k_x $\left[\frac{\text{kN}}{\text{m}}\right]$	k_{θ_y} $\left[\frac{\text{kN}\cdot\text{m}}{\text{rad}}\right]$	k_y $\left[\frac{\text{kN}}{\text{m}}\right]$	k_{θ_x} $\left[\frac{\text{kN}\cdot\text{m}}{\text{rad}}\right]$
1	1.30×10^7	3.00×10^8	1.47×10^7	3.00×10^8
2	8.35×10^6	2.15×10^8	1.18×10^7	2.60×10^8
3	6.80×10^6	1.72×10^8	5.80×10^6	1.50×10^8

discrete model as in finite element analysis and using the equilibrium of forces,

$$k_x u_0 = -\sum_{j\in\{j\}} m_j \ddot{u}_j \tag{4.6}$$

Likewise, the equilibrium of moments would dictate

$$k_{\theta_x}\theta_{x0} = -\sum_{j\in\{j\}} j m_j \ddot{u}_j \tag{4.7}$$

As in Chapter 2, the index j spans the elevations for which there are measurements of acceleration. Obviously, k_x and k_{θ_x} are the spring constants that are to be calculated, x_0 and θ_{x0} are the displacement and the rotation at the base, respectively, and m_j is the mass at elevation j. Evidently, the left hand side of the above 2 expressions represent the forces and moments due to the springs.

Regarding the calculation of the mass to use per elevation, the wind turbine was divided into sections by elevation. The finite element nodes closest to the elevations where the measurements were taken were used as the center of these sections. The mass was summed for each section and assigned as the mass at that elevation. Hence this method conserves the mass of the system. These values are displayed in Tables 4.4 and 4.5 for reference. Please note that the mass of the nacelle, rotor, and blades is lumped at the top.

Equations (4.6) and (4.7) were applied to both fore-aft and side-to-side modes and used to calculate the spring constants k_x and k_{θ_x}. Since accelerations were the measured quantities and the displacements were inferred using Equation (4.3), this equation was to be substituted in Equation (4.6). In Equation (4.7), θ_{x0} was already calculated as seen in Figures 4.2- 4.7. Applying these changes,

$$k_x = \frac{\omega^2}{\ddot{x}_1} \sum_{j\in\{j\}} m_j \ddot{u}_j \tag{4.8}$$

$$k_{\theta_x} = -\frac{1}{\theta_{x0}} \sum_{j \in \{j\}} j m_j \ddot{u}_j \tag{4.9}$$

The results of these calculations are displayed in Table 4.6.

Table 4.4: Summary of the mass and fore-aft acceleration used for each elevation in the equilibrium approach.

Elevation [m]	Mass [tonnes]	Fore-Aft Acceleration [g]		
		Mode		
		1	2	3
0.00	7.33	0.002×10^{-3}	0.016×10^{-2}	-0.231×10^{-2}
7.00	12.00	0.036×10^{-3}	0.178×10^{-2}	-1.084×10^{-2}
13.00	13.31	0.091×10^{-3}	0.422×10^{-2}	-1.953×10^{-2}
22.00	13.16	0.244×10^{-3}	0.899×10^{-2}	-2.410×10^{-2}
32.00	12.14	0.498×10^{-3}	1.288×10^{-2}	-1.339×10^{-2}
42.00	6.63	0.988×10^{-3}	1.044×10^{-2}	2.704×10^{-2}
52.00	43.55	1.474×10^{-3}	0.042×10^{-2}	2.070×10^{-2}

Table 4.5: Summary of the mass and side-to-side acceleration used for each elevation in the equilibrium approach.

Elevation [m]	Mass [tonnes]	Side-to-side Acceleration [g]		
		Mode		
		1	2	3
0.00	7.33	0.003×10^{-3}	0.099×10^{-2}	-0.013×10^{-1}
7.00	12.00	0.046×10^{-3}	1.205×10^{-2}	-0.023×10^{-1}
13.00	13.31	0.120×10^{-3}	2.758×10^{-2}	0.100×10^{-1}
22.00	13.16	0.328×10^{-3}	5.933×10^{-2}	0.663×10^{-1}
32.00	12.14	0.663×10^{-3}	8.609×10^{-2}	0.046×10^{-1}
42.00	6.63	1.301×10^{-3}	7.280×10^{-2}	-1.835×10^{-1}
52.00	43.55	1.927×10^{-3}	0.803×10^{-2}	-0.107×10^{-1}

4.4 Rigid-Body Contribution Due to Base Motion

Since the effort was already expended to construct and calculate $\mathbf{B}^{max}$ and $\mathbf{U}^{max}$ from the experimental acceleration values (Equations (4.4) and (4.5)), the

Table 4.6: The soil stiffness calculated using the equilibrium approach.

	Fore-Aft		Side-to-Side	
Bending Mode	k_x $\left[\frac{\text{kN}}{\text{m}}\right]$	k_{θ_y} $\left[\frac{\text{kN}\cdot\text{m}}{\text{rad}}\right]$	k_y $\left[\frac{\text{kN}}{\text{m}}\right]$	k_{θ_x} $\left[\frac{\text{kN}\cdot\text{m}}{\text{rad}}\right]$
1	3.56×10^5	9.26×10^7	4.12×10^5	8.42×10^7
2	1.69×10^6	2.46×10^8	1.93×10^6	2.47×10^8
3	2.54×10^5	4.38×10^8	2.43×10^6	3.16×10^9

author feels that is appropriate to also display a measure of how much $\mathbf{U}^{max}$ is affected by $\mathbf{B}^{max}$. Recalling Equation (2.2), if $\ddot{U}_{mnp}$ is the absolute maximum entry in the response array, then U_{mnp} is the absolute maximum of its respective array. If the base is treated as a rigid body, then a net translation of $\mathbf{B}^{max}$, as well as a slope, can be obtained. Graphically speaking, this was done for each figure in the set of Figures 4.2-4.7, and accomplished by calculating the midpoint, x^{mid}, at the base, and the slope, $\frac{dy}{dx}$, between of the two points labeled "Experimental" on these figures. Note that the references to x and y here denote directions as seen on the graphs and are not related to the global coordinate system of the experiment introduced in Chapter 2. The rotation is then given by

$$\theta = \tan^{-1} \frac{dy}{dx}$$

Now that the quantities x^{mid} and θ are defined, the percentage influence of the base on the maximum of the response array through rigid body motion is defined as

$$\Phi_{rigid} = \frac{x^{mid} - n \sin\theta}{U_{mnp}} \times 100 \tag{4.10}$$

Clearly the numerator is meant to account for the rigid body motion as it includes mean translation through x^{mid} and rotation through $n \sin\theta$ because $n \in \{j\}$. As usual, the indices m, n, and p are defined though Equation (2.2).

These definitions were used to construct Table 4.7. Please note that a negative sign indicates that the net result of mean translational plus rotational effects is opposite to the actual displacement.

While the negative signs in the 3rd bending modes do slightly obscure some of the results, one observation evident in Table 4.7 is that the participation of soil-structure interaction is considerably more important in the 2nd bending modes

Table 4.7: Rigid body contribution to maximal displacement

	Rigid Body Contribution [%]	
Mode	Fore-aft	Side-to-side
1	1.91	1.99
2	8.94	9.71
3	-49.08	-2.26

compared to the 1st modes. This is at least consistent with the results noted by Bazeos et al. (2002), where they noted that higher bending modes tend to be more affected when elastic soil is taken into account. Also, since the natural frequencies for the 2nd bending modes fall in the realm of about 4 Hz, while those for the 1st bending modes are about 0.6 Hz, there may be situations in which the earthquake motion excites the 2nd modes more than any others, further suggesting that understanding soil-structure interaction could potentially reap benefits as it concerns designing structures to be placed on soft soils.

4.5 Results and Conclusions

A comparison of Tables 4.2, 4.3, and 4.6 reveals a somewhat limited agreement. Comparing only Tables 4.2 and 4.3, it is observed that the translational spring constants have little agreement, and that the values often differ by factors of 10. While this is noticeable, the rotational spring constants agree slightly better. Here they frequently have the same magnitude, and the actual values sometimes do not differ too much, especially in the second bending modes. Possible explanations for the observed differences include the possibility that deflection magnitudes were different during the particular employed data segments (i.e. a level of amplitude dependant nonlinear response).

By contrast, comparing Table 4.2 with Table 4.6 demonstrates almost no agreement across all modes. Only in the cases of the second modes was there fair agreement in the values of the springs. It appears that using the equilibrium approach typically results in softer spring constants compared to the other method used in this chapter. Evidently some more effort is needed in this area to explain this difference. This lack of congruity might be explained by the fact that the entire rotor mass was used when calculating the force applied to the top. It may be that the not all the rotor mass contributes, or that sections of the blades contribute in an out-of-phase manner. Perhaps some further investigation using the finite element model (where the blades, rotor, and nacelle connections to the turbine tower are more faithfully represented) might advance some knowledge on the subject. In addition, the possibility of having experimental data measuring the blades' acceleration would be invaluable, though they were not recorded as part of the investigation introduced in Chapter 2.

It should also be stated that a direct comparison between Tables 4.2 and 4.1 would not be valid because of the substantially different properties between the two wind turbine systems and their foundation types. The inclusion of the results seen in Bazeos et al. (2002) was merely to give the reader some context for the results of this thesis.

Bibliography

Apsel, R. J. and Luco, J. E. (1987). "Impedance Functions for Foundations Embedded in a Layered Medium: An Integral Equation Approach". *Earthquake Engineering & Structural Dynamics*, 15(2):213–231.

Bazeos, N., Hatzigeorgiou, G. D., Hondros, I. D., Karamaneas, H., Karabalis, D. L., and Beskos, D. E. (2002). "Static, seismic and stability analyses of a prototype wind turbine steel tower". *Engineering Structures*, 24(8):1015–1025.

Luco, J. E. (1986). "On the relation between radiation and scattering problems for foundations embedded in an elastic half-space". *Soil Dynamics and Earthquake Engineering*, 5(2):97–101.

Prowell, I. (2010). *An Experimental and Numerical Study of Wind Turbine Seismic Behavior*. PhD thesis, University of California, San Diego.

Vierck, R. K. (1979). *Harmonically Forced Vibrations for Single-Degree-of-Freedom Systems*, chapter 4, pages 90–147. Vibration Analysis. Harper and Row, New York, N.Y., second edition.

Zhao, X. and Maißer, P. (2006). “Seismic response analysis of wind turbine towers including soil-structure interaction”. *Proceedings of the Institution of Mechanical Engineers Part K-Journal of Multi-Body Dynamics*, 220(1):53–61.

Chapter 5

Simulations of Wind Turbine Dynamics Including Soil-Structure Interaction

A more formal approach to soil-structure interaction is taken in this chapter. New software is presented allowing a soil domain to be modeled by finite-elements and placed at the base of a wind turbine-like model. The dimensions and physical properties of this soil domain are given in the text with ground flexibility modeled through the use of a variable shear wave velocity. Earthquake motions are then applied to this extended wind turbine/soil domain model and the results are displayed for comparison. Using this approach, earthquake excitation is imparted with soil-structure interaction dictated by the foundation configuration and the surrounding soil stiffness.

5.1 Related Earlier Research

The author wishes to open this chapter with some discussion about two earlier studies involving finite element simulation of soil-structure interaction effects. It will soon become obvious to the reader that the author of this thesis took a similar approach to this line of modeling.

The reader should take note of the work in Prowell et al. (2009). The mode shapes and natural frequencies obtained for a 900 kW wind turbine are compared to a finite element model consisting of both a discretized structure and supporting soil domain. Agreement with the experimental modal properties was shown to occur for stiff soil properties. This result was then used to extrapolate that this numerical model might more closely capture the wind turbine behavior if the soil characteristics were altered to simulate traits present in softer soils.

Again in Prowell et al. (2010), a finite element wind turbine model was placed atop a linear elastic soil domain. This time, Prowell et al. (2010) was attempting to infer the behavior of a proposed design for a 5 MW wind turbine subject to soil-structure interaction. The author shows that this modeling approach returns similar fixed-base natural frequencies as other accepted programs and then subjects the model to an earthquake motion three times, while varying the soil stiffness each time. The work concludes with an examination of the bending moment and transverse shear demand, demonstrating that softer soil considerations could change the expected distribution of these two quantities and hence alter design methods.

5.2 Modeling in BridgePBEE

For this chapter, the author has decided to introduce some new software in hopes of facilitating the simulation of the dynamics of wind turbines. The author has employed a modified version of OpenSees **Bridge P**erformance-**B**ased **E**arthquake **E**ngineering, heretofore referred to as BridgePBEE (Lu et al., 2011). The BridgePBEE web page (`http://peer.berkeley.edu/bridgepbee/`) describes the program as thus:

> **BridgePBEE** is a PC-based graphical pre- and post-processor (user-interface) for conducting Performance-Based Earthquake Engineering (PBEE) studies for bridge-ground systems (2-span single column). The three-dimensional (3D) finite element computations are conducted using **OpenSees** developed by the Pacific Earthquake Engineering Research Center (PEER). The analysis options available in BridgePBEE include: 1) Pushover Analysis, 2) Base Input Acceleration Analysis, and 3) Full Performance-Based Earthquake Engineering (PBEE) Analysis.

Although BridgePBEE has the performance-based earthquake engineering functionality, this type of analysis was not used in this study. The author's main interest in the program related to its simple to use modeling capabilities, the ability to apply multiple successive earthquake motions on a system, and its post processing environment which displays many useful measures.

5.2.1 Modeling the Wind Turbine

BridgePBEE is, first and foremost, a tool to analyze a bridge structure. The author concedes that in order to take advantage of the many features offered by BridgePBEE it was necessary to make some modifications so that it may analyze a model that would represent a wind turbine. The author chose to use BridgePBEE to create a lumped mass model of a wind turbine similar to Bazeos et al. (2002). While this model is simpler than those used in Chapters 3 and 4, Prowell et al. (2009), and Prowell et al. (2010), at a minimum the results should be similar to those obtained with the guidelines provided in Risø (2002).

For the analysis of a bridge structure, the diameter of the column (the central vertical member in Figure 5.1) is typically assumed to be much less than the length of the bridge deck (the long horizontal member seen in Figure 5.1). To create a lumped mass model to represent a wind turbine, the deck length was selected to approach the column diameter.

Next there was the matter of the abutment (the triangular sections on either side of the bridge in Figure 5.1). Since a wind turbine has no such supporting structure, these sections had to be removed from the column and the bridge deck. This was accomplished by using a special, modified version of BridgePBEE that allowed this to be removed entirely.

The rest of the model was built to emulate the standard OpenSees model used in Chapters 3 and 4. A table of physical properties and their numerical values for the BridgePBEE model is included (see Table 5.1). Many of these values were chosen as such to correspond as close as possible to the OpenSees model seen in Chapters 3 and 4. These include the length above grade, the number of column elements, and Young's Modulus. The value for the lumped mass was

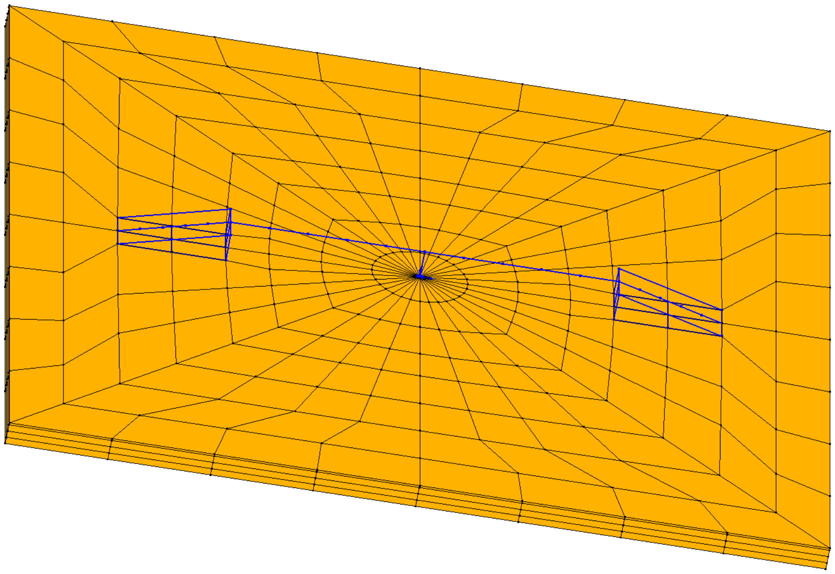

Figure 5.1: The default geometric configuration for BridgePBEE. (i.e. a bridge)

determined by a special mode in the OpenSees model that uses a lumped mass instead of a distributed mass for the nacelle and rotor. Since the OpenSees model was created with a diameter tapering with elevation, the diameter was chosen as an intermediate value between those at the top and base. The column mass density was chosen to match the sum of all tower nodal masses in the OpenSees model divided by the area (using the chosen diameter), and divided again by the length above grade. The method by which the second moments of area were selected will discussed later.

Table 5.1 as lists the values used for the mass and stiffness proportional viscous damping coefficients. A detail worthy of mention is that these values correspond to the damping used in the wind turbine model from Prowell (2010), which analyzed only the structural response. Due to the limitations of BridgePBEE as of the time of this writing, damping parameters could not be assigned separately for the soil. This is unfortunate since soil damping is typically significantly larger that its structural counterpart. Hence the results from this section of the investigation will have to be viewed with this in mind.

A significant change that needed to be made to the BridgePBEE model

Table 5.1: Properties of BridgePBEE numerical model

Property	Value
Column Diameter	2.66 m
Column Length Above Grade	56.3994 m
Column Mass Density	0.2305 $\frac{\text{ton}}{\text{m}^3}$
Number of Column Elements	53
Foundation Diameter	2.66 m
Foundation Length	9.144 m
Number of Foundation Elements	4
Young's Modulus	200×10^6 kPa
2^{nd} Moment of Area @ Transverse Axis	0.13 m^4
2^{nd} Moment of Area @ Longitudinal Axis	0.13 m^4
Column Top Mass	39.4535 ton
Mass Proportional Viscous Damping Coefficient	2.3165×10^{-2}
Stiffness Proportional Viscous Damping Coefficient	4.0943×10^{-3}

compared to the OpenSees model involved extending the tower deeper into the soil as though supported by an embedded foundation. This was necessary because the theory of soil-structure-foundation interaction asserts that the dynamics of such a situation is a function of the embedment ratio, which is the ratio of how deep a foundation is buried within the soil compared to its height (Luco, 1986). In accordance with engineering documents that are available in reference to the NEG Micon 53.6 meter tower model, the foundation was taken to have a length of 9.144 meters. Its diameter was taken to be the same as that of the tower, 2.66 meters.

The second moment of area was treated as a free parameter that would be modified so that the results from BridgePBEE would have the "best" fit when compared to the OpenSees model. For the purposes of this study, the best fit was defined as having the natural frequencies for the first three fixed-base bending modes have as small an error as possible when compared to the model of Chapters 3 and 4. The value 0.13 m^4 satisfied this criteria. Table 5.2 has been provided to show the reader the fixed-base natural frequencies that result with the BridgePBEE model for theses values of the properties discussed in this section. Note that the BridgePBEE model is essentially axially symmetric and as such, it is not necessary to make a distinction between fore-aft and side-to-side bending. Despite the limitations of the tower, these results display a reasonable amount of error

Table 5.2: BridgePBEE model (fixed-base) natural frequencies

Bending Mode	Frequency [Hz]
1st	0.44096
2nd	3.78707
3rd	11.62440

when compared to Table 3.2 in the first and second bending modes.

Since new, admittedly experimental software was to be used for the purposes of this thesis, it was necessary to verify it is equivalent to existing, more popular packages. This necessity is underscored by the fact that BridgePBEE had to be significantly modified to analyze a numerical model that represents a wind turbine. This validation is provided by Figure 5.2. It displays the absolute acceleration response due to the same earthquake of the two models on top and the input earthquake on the bottom. The thick, grey lines represent the result of an identical model constructed using standard OpenSees environment compiled by Berkeley (`http://opensees.berkeley.edu`) and the thin, black lines are the response from the BridgePBEE model. Both models assume a fixed-base structure for simplicity. The responses are the same as expected.

5.2.2 Soil Domain Geometry and Properties

In general, the soil domain has been set to behave linearly elastic, with the stiffness controlled by the shear wave velocity. The Poisson's Ratio of the soil was fixed at 0.2. At any depth within the soil domain, all lateral boundary nodes are constrained to move together, thus emulating the conventional shear-deformable beam soil amplification condition. The soil base boundary conditions are also such that the nodes at the very bottom of the domain are constrained from motion in all degrees of freedom. These support nodes are therefore the set of nodes in which the earthquake excitation will be prescribed later (i.e. a moving support).

As can be seen in Figure 5.3, the approach was to choose the soil domain boundaries to be very large compared to the diameter of the column in hopes of minimizing edge effects. It was desired to have the soil be modeled as a box with

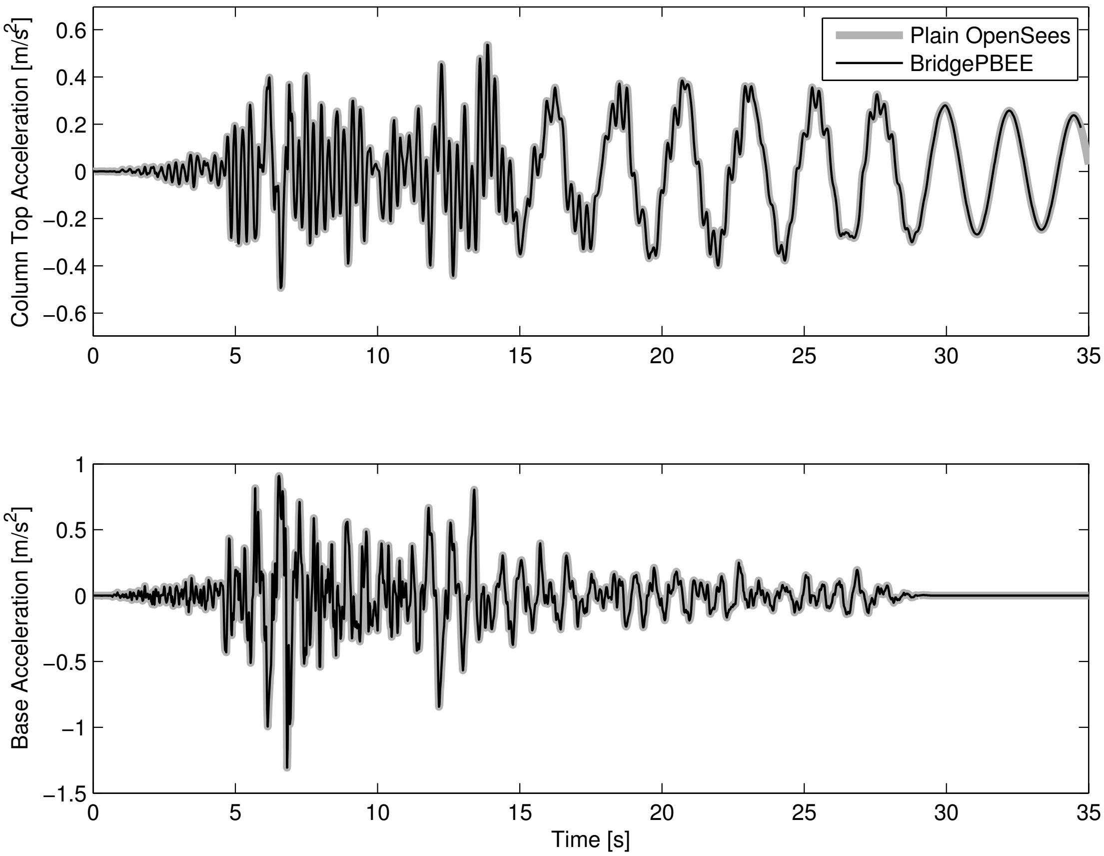

Figure 5.2: Comparison of the response of a modified fixed-base BridgePBEE model versus the equivalent model done in the standard OpenSees package.

dimensions of (at least) 100 m x 100 m x 20 m. The actual dimensions turned out to be a little bit larger horizontally ($103\frac{1}{3}$ m x $103\frac{1}{3}$ m x 20 m) because of mesh effects caused by removing the embankments, but since they are already very far away from the column, the end result should not change.

A reader familiar with the works of Prowell et al. (2009) and Prowell et al. (2010) will notice that the soil boundaries implemented in this chapter are significantly smaller than those used in the aforementioned publications. That reader should also notice the finer mesh used here for the soil domain, which is the principle agent accounting for computational cost. In fact, this mesh was already quite taxing to local computational resources for just a single earthquake simulation. Further exacerbating the problem is that this author wished to apply multiple

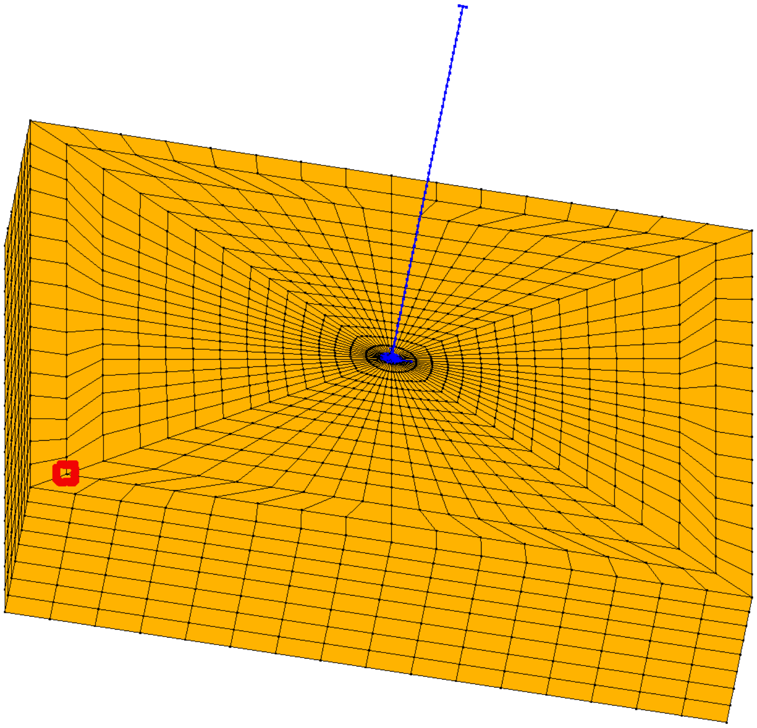

Figure 5.3: A "wind turbine" built in a modified version of BridgePBEE Lu et al. (2011).

earthquake simulations to observe general trends. This level of mesh refinement with these boundaries is justified. Indeed, when performing numerical calculations on situations involving soil-structure interaction, the frequency resolution in the soil domain is limited by the size of the largest element present in the mesh. This characteristic size will be denoted as l_e. Varun et al. (2009) suggested that in these kinds of wave propagation problems, at least six elements per wavelength should be used to accurately resolve the minimum wavelength, λ_{min}, in the soil mesh. More formally,

$$\frac{1}{6}\lambda_{min} \geq l_e \tag{5.1}$$

This result is slightly more instructive if it is put in terms of frequency instead of wavelength. From basic physics,

$$v_s = \lambda f \tag{5.2}$$

where v_s is the wave velocity and is taken to be a constant. Given the context, it corresponds to the shear wave velocity and f is then the wave linear frequency.

After substitution and rearranging Formulae 5.1 and 5.2,

$$f \leq \frac{v_s}{6l_e} \tag{5.3}$$

Equation (5.3) allows for an estimation of what frequencies this mesh was able to accurately represent. For the elastic case, v_s was chosen as 200 m/s, and l_e can be obtained from the mesh. From Figure 5.3, we observe that the mesh grew coarser as the horizontal distance from the structure increased. Figure 5.4 was provided to give an accurate detailing of how the mesh is constructed. Notice that Mesh Layer #8 is the coarsest layer, being of length 15 m with only 3 sub-layers. Assuming that the layers' distance are divided evenly by the number of sub-layers, the horizontal distance of this sublayer is around 5 m. For a 5 m x 5 m element, and assuming waves propagating only in the horizontal plane, the worst case scenario would be that a wave propagates hypothetically along the diagonal of the element. If this is true, $l_e = 5\sqrt{2}$ m. For these numbers, Formula 5.3 returns $f \leq 4.71$ Hz. This cutoff frequency was considered acceptable because the first and second fixed-base natural frequencies were found to fall in this range (see Table 5.2).

5.3 Motion Terminology in this Chapter

An accompanying discussion to help distinguish the types of motion subsequently used in the following section is prudent at this time. To begin, there is the input motion acceleration and this is the motion imposed at the very bottom of the soil in the model. Next there is the base acceleration, which is the response at the intersection of the top of the ground surface and the bottom of the tower while still remaining above grade. This could be thought of as the turbine base acceleration. There is also the free-field acceleration, which is the acceleration response at a point "far away" from the tower. This point has been boxed in red in Figure 5.3. Lastly there is the nacelle acceleration, where the name is self-explanatory.

For the remainder of the analysis, I have assumed that since the free-field acceleration measurement is taken to be "far away," it is equivalent to what would be measured by instrumentation if an earthquake were to occur and the device is

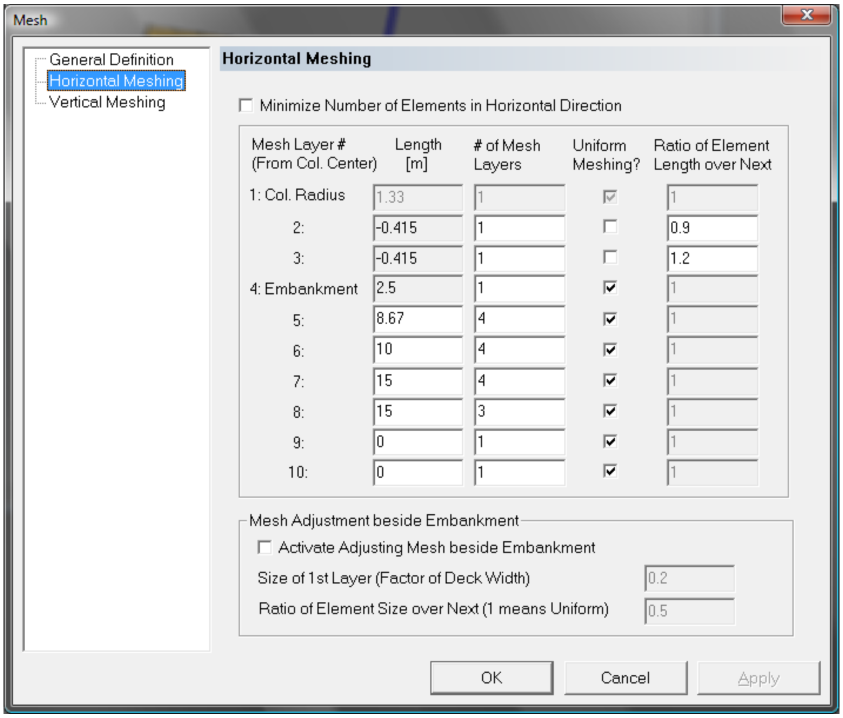

Horizontal Meshing

☐ Minimize Number of Elements in Horizontal Direction

Mesh Layer # (From Col. Center)	Length [m]	# of Mesh Layers	Uniform Meshing?	Ratio of Element Length over Next
1: Col. Radius	1.33	1	☑	1
2:	-0.415	1	☐	0.9
3:	-0.415	1	☐	1.2
4: Embankment	2.5	1	☑	1
5:	8.67	4	☑	1
6:	10	4	☑	1
7:	15	4	☑	1
8:	15	3	☑	1
9:	0	1	☑	1
10:	0	1	☑	1

Mesh Adjustment beside Embankment

☐ Activate Adjusting Mesh beside Embankment

Size of 1st Layer (Factor of Deck Width) 0.2

Ratio of Element Size over Next (1 means Uniform) 0.5

Figure 5.4: Horizontal meshing scheme for the PBEE model.

not too close to the wind turbine. This assumption will be important in a later section.

5.4 Transfer Functions and the Soil Domain

The objective of this study was to apply a set of earthquake motions to a wind turbine-like model with soil-structure interaction for two different cases of soil stiffness and compare the results. The soil profiles included effectively rigid soil (fixed-base), as well as elastic soil achieved by setting the shear wave velocity to $v_s = 200$ m/s.

Given this type of setup where the elasticity of the soil is variable and the earthquake motions are imposed at the supports, then the same input acceleration will cause different free-field responses for different soil profiles. Such a situation would invite questions of dynamic equivalence between the two models. With the reasoning that physical measurements of earthquake acceleration are taken far away from a structure, it makes more sense that dynamic equivalence should impose that the free-field acceleration, not the acceleration at the supports, be identical between the two soil profiles. In order to obtain the same free-field ground acceleration for each earthquake, the author took advantage of the linearity of the system and used a transfer function in the frequency domain. That is, an input acceleration time series $\vec{a}_0(t)$, used to stand in for the motion that would be recorded by an accelerometer at this particular depth, was applied to the soil model base, then the resulting free-field acceleration $\vec{a}_f(t)$ was extracted. Both these signals were then converted to the frequency domain using a Discrete Fourier Transform, returning $\vec{A}_0(\omega)$ and $\vec{A}_f(\omega)$, respectively, and used to construct a transfer function matrix $\mathbf{T}(\omega)$ for the system for each direction. For the purposes of this study, the matrix was taken to have the entries

$$\mathbf{T}(\omega) \equiv \begin{bmatrix} \frac{A_{f1}(\omega)}{A_{01}(\omega)} & 0 & 0 \\ 0 & \frac{A_{f2}(\omega)}{A_{02}(\omega)} & 0 \\ 0 & 0 & \frac{A_{f3}(\omega)}{A_{03}(\omega)} \end{bmatrix} \tag{5.4}$$

Since the transfer function is a property of the system, and in the frequency domain the relation is multiplicative, it can easily be used to calculate the input acceleration that should be used to produce the desired free-field motion(s). Given a particular free-field earthquake acceleration, $\vec{x}_f(t)$, the input acceleration $\vec{x}_0(t)$ that would produce it is given by

$$\vec{X}_0(\omega) = \mathbf{T}^{-1}(\omega)\vec{X}_f(\omega) \tag{5.5}$$

Where as before, $\vec{X}_0(\omega)$ and $\vec{X}_f(\omega)$ are the Discrete Fourier Transforms of $\vec{x}_0(t)$ and $\vec{x}_f(t)$, respectively. Note though, that this transfer function is, in general, different for each soil profile, and it is taken to be equal to 1 for all frequencies and indices in the case of rigid soil.

The author will now simply describe what signals he used to create the transfer function. To create $\vec{a}_0(t)$ the author used an algorithm that generated random numbers between ± 0.1. Because the author did not wish to complicate his transfer function algorithm unnecessarily, it was decided that the signal would be isotropic for any given time and that it would be imposed at the same sampling rate as that of the preselected earthquake motions, 50 Hz (they were all sampled at this rate). This signal was also chosen to have 5,300 data points because this made $\vec{a}_0(t)$ longer than any of the earthquake motions. Naturally $\vec{a}_f(t)$ is the free-field signal that results after imposing $\vec{a}_0(t)$ at the bottom of the soil domain of the BridgePBEE model when v_s is set to 200 m/s. This is sufficient to create $\mathbf{T}(\omega)$. In the rigid case, the free-field motion $\vec{x}_f(t)$ is the same as the input motion, so this is already known. At this point, the author used Equation (5.5) to get the appropriate input motion that should return the correct free-field motion. This process was evidently repeated for every earthquake motion. For more specific information regarding the employed earthquake ground motions and examples of this algorithm's ability to reproduce free-field ground motions, please see Appendix C.

The author wishes to state a detail of importance as it relates to building the transfer function. When $\vec{a}_0(t)$ was applied to the soil to obtain $\vec{a}_f(t)$ and construct $\mathbf{T}(\omega)$, the tower structure was still embedded in the ground. This is stated for clarity because there are alternative approaches that involve calculating the transfer function for a soil domain in the absence of a structure.

5.5 Results and Conclusions

Figures 5.5-5.11 display the results with regard to the two soil profiles separately. When done this was, the outcomes are more traditional and easier to read. They should be used more for reference than anything else. Please also note that all figures discussed in this section, have their horizontal axes calculated with respect to the SRSS of the listed component. This is a common abbreviation. It stands for the **S**quare **R**oot of the **S**um of **S**quares and it refers to the fact that the horizontal components of the measurement in question have been combined in this manner. Also note that although the results are given with respect to SRSS values, the applied shaking was three-dimensional.

A technicality that should be noted in reference to Figures 5.5 and 5.6 is that the maximum shear forces and moments are displayed in these figures, regardless of elevation. However, a side-by-side comparison of these quantities with their respective counterpart measures at the base reveals that in many cases, they are the same and when they are not, the difference is usually negligible. As a result, the same figures done so as to display Figures 5.5 and 5.6 with measures taken at the base would appear very much the same.

Of further interest in Figure 5.6 is the direct comparison with results found in Prowell (2010). Prowell (2010) subjected a wind turbine model to several earthquakes records drawn from Mackie and Stojadinović (2005) using the FAST software (Jonkman and Buhl, 2005). Since the author used records from the same set (see Appendix C), and applies them to a model emulating a 900 kW wind turbine, the bending moment results should be comparable. For the case of the parked wind turbine in Prowell (2010), it is observed that the simple lumped mass model used in this thesis indeed reaches a similar upper bound for the base bending moment at around 40,000 kN-m even though the FAST model is more complicated. For further clarity, the maximum bending moments have been plotted in Figure 5.7 against the free-field peak acceleration. This figure allows an easier comparison with the work of Prowell (2010) because the acceleration values are also displayed. Here it is also observed that the peak accelerations are consistent with Prowell (2010). The largest values fall around the range of 1.0 g.

In contrast to some of the previously described figures, it is much easier to contrast Figures 5.12-5.14 between the 2 soil profiles. In these figures, the results for both soil profiles are plotted together, with corresponding points connected by an arrow. The pointed end of the arrow signifies that the results belongs to the set of data where the shear wave velocity is $v_s = 200$ m/s.

Figures 5.12 and 5.13 display a similar trend. Both the maximum transverse shear and the maximum bending moment tended to increase for the case of flexible soil with $v_s = 200$ m/s. This trend is observed for all types of applied motions, though it is more pronounced for motions in the Near bin. This is somewhat counterintuitive since it is generally believed that a flexible base would displace in such a way that would minimize deflections in the tower, thus inferring less internal forces and moments in the structure.

The information used to create Figure 5.14 is drawn from the same data used to create 5.12 and 5.13. The maximum bending moment is divided by the maximum shear force and this quantity is argued to act as an effective lever arm due to the fact that these maxima typically occur at the base of the structure.

$$r_i^{eff} \equiv \frac{M^{max}}{V^{max}} \tag{5.6}$$

Here, i = rigid or 200 to denote a rigid soil profile or the elastic profile used where $v_s = 200$ m/s. The author justifies the validity of this quantity because, as stated above, M^{max} and V^{max} are approximately equal to the maximum values of shear and moment at the base of the tower. This effective lever arm can act as a guide, demonstrating when the response of the structure is mostly captured by a first bending mode approximation. The reader should recall that the tower length above grade used in these simulations was about 56.4 meters. For data points which have effective lever arms very close to this value, the response is said to emulate the first mode response very well. The reader should be aware, however, that the maximum shear and the maximum bending moments did not generally occur at the same time, which the author admits does diminish some of the credence of this quantity.

The trend in Figure 5.14 decidedly shows that in the change to a softer soil stiffness, the data shifts towards shorter lever arms (in some cases, quite dramatically). This implies that the percentage change in the maximum shear is greater than that of the maximum moment, which appears to agree with what is observed in Figures 5.12 and 5.13. This observation supports the notion that including soil-structure interaction increases the relative contribution of higher modes in structural response.

Figures 5.15 - 5.20 have been included to supplement Figure 5.14. These figures show the distribution of the percentage decrease in effective lever arm that results from lowering the stiffness of the soil. The percentage decrease uses Equation (5.6) and is calculated as

$$\%\text{ decrease in lever arm} = -\frac{r_{200}^{eff} - r_{rigid}^{eff}}{r_{rigid}^{eff}} \tag{5.7}$$

Figure 5.15 includes this data for all the motions described in Appendix C while Figures 5.16 - 5.20 demonstrate the breakdown of this information by earthquake bin (LMSR, LMLR, SMSR, SMLR, and Near, respectively). Note that the earthquakes have been sorted into bins with a width of 5% for this set of graphs.

In Figure 5.15, it is observable that about 22 out of 65 records saw a modest change (within ±5%) in their effective lever arm after decreasing the shear wave velocity. Just as many cases have report a change between 5% and 15%. For the former set of records, the dominant mode has likely not changed. The latter set though is far more likely to have very distinct frequency content. For the overwhelming majority of records, the lever arm has decreased (in some cases significantly). There is one incidence of a lever arm increase of 10% or more. This motion can be seen in Figure 5.16 indicating that it is contained within the LMSR bin.

Also interesting was that records in the SMLR, SMSR, and Near bins seemed to display larger changes in the lever arm more consistently, as can be seen in Figures 5.18, 5.19, and 5.20.

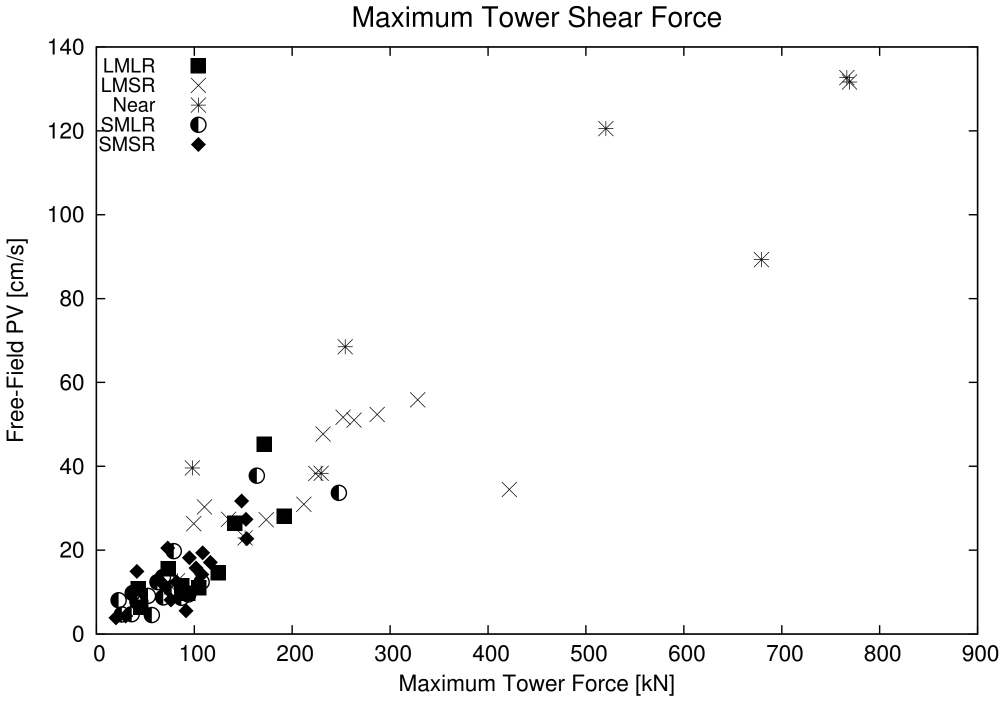

(a) rigid case

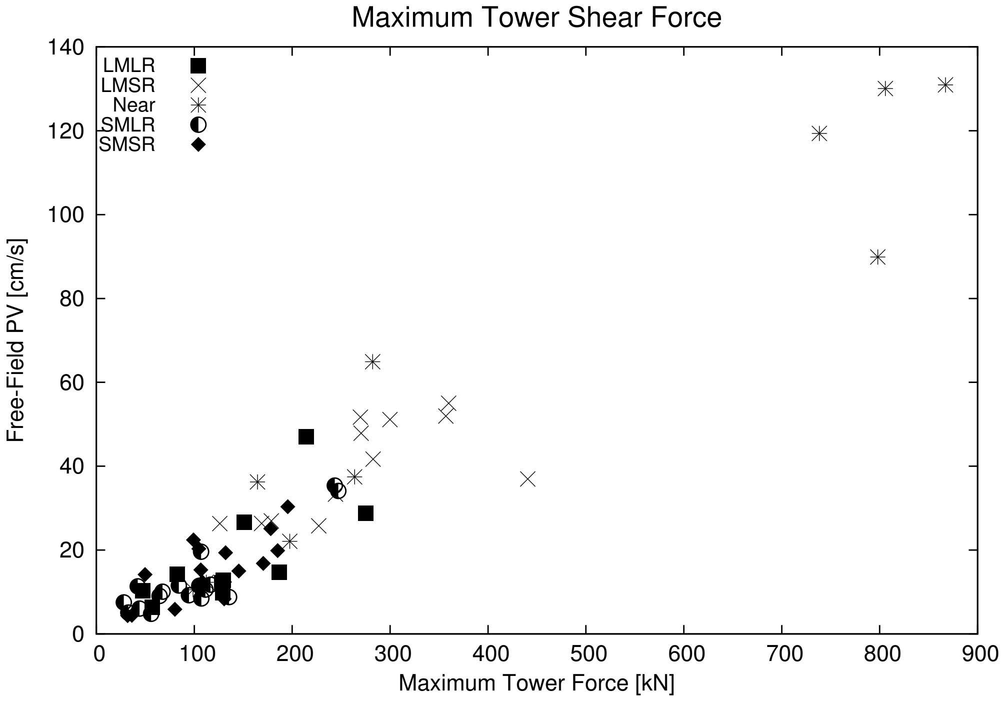

(b) $v_s = 200$ m/s case

Figure 5.5: Shear force demand plots.

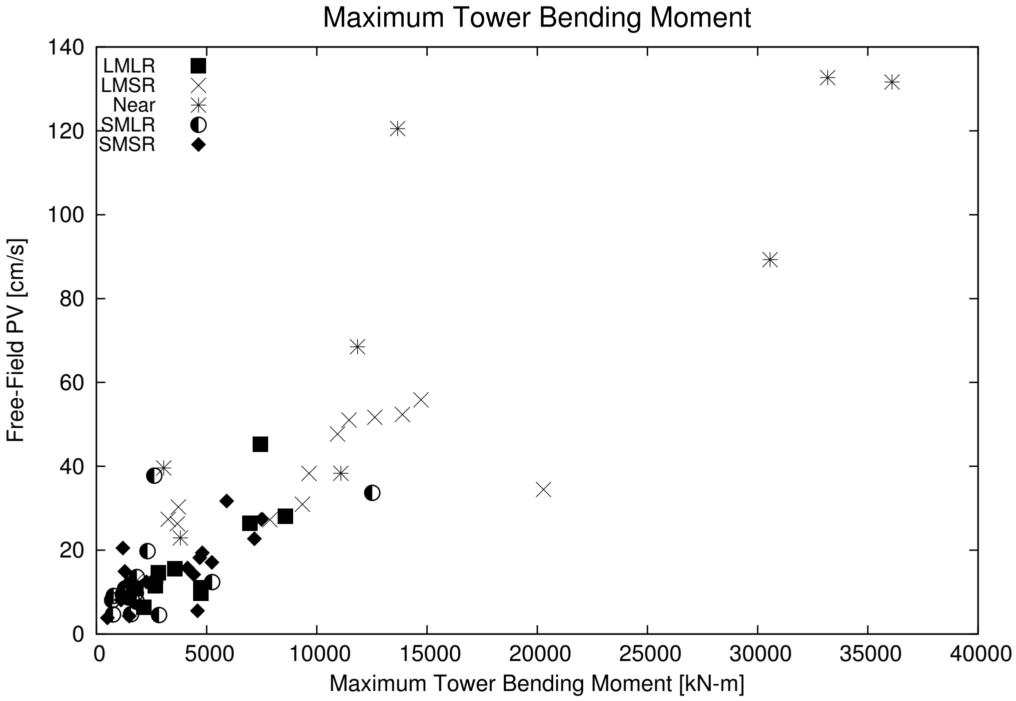

(a) rigid case

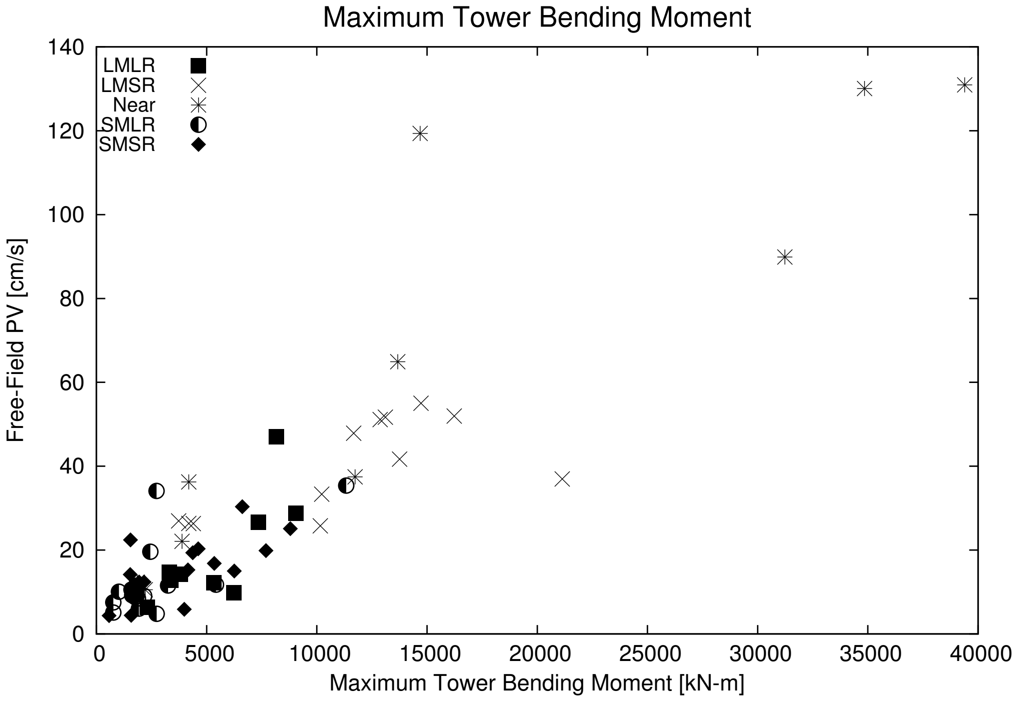

(b) $v_s = 200$ m/s case

Figure 5.6: Moment demand plots.

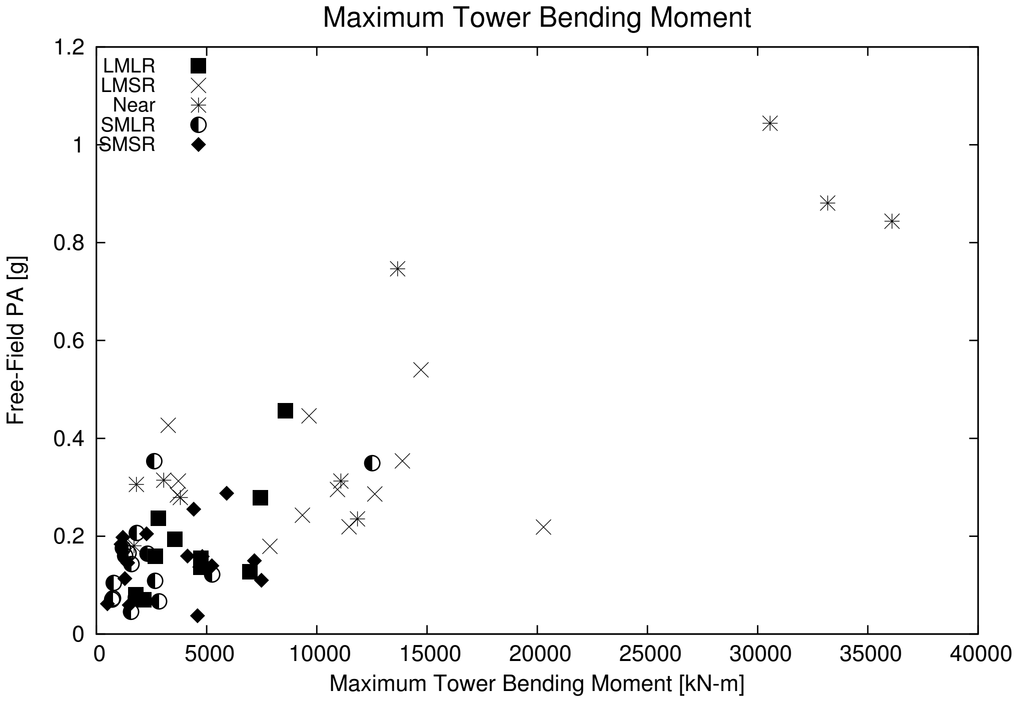

(a) rigid case

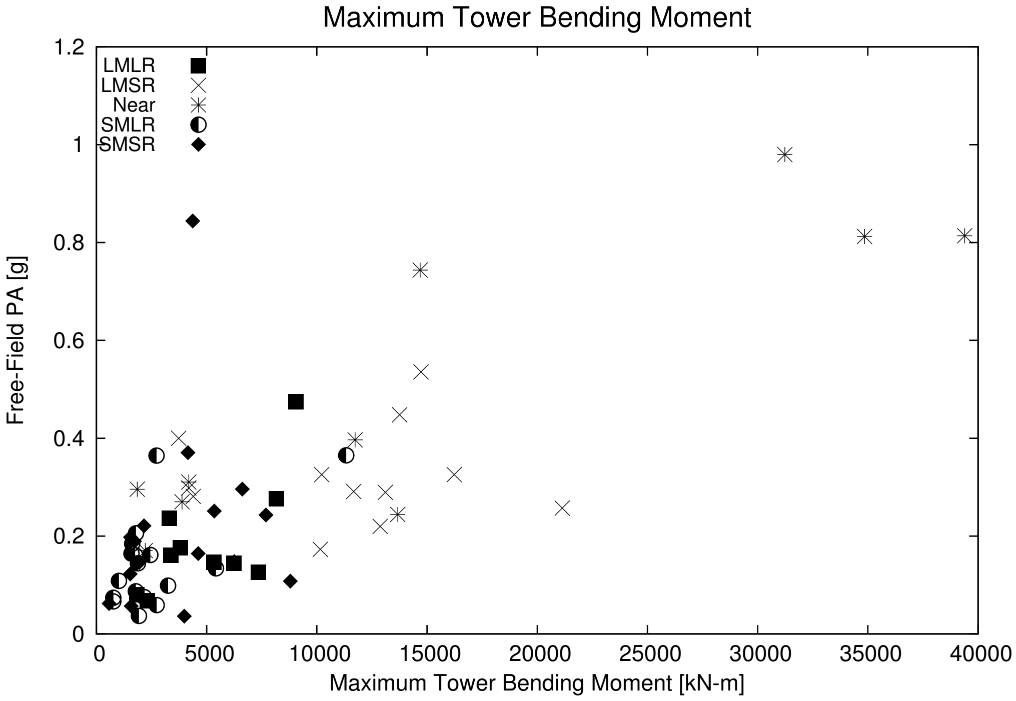

(b) $v_s = 200$ m/s case

Figure 5.7: Moment demand plots (plotted against free-field peak acceleration).

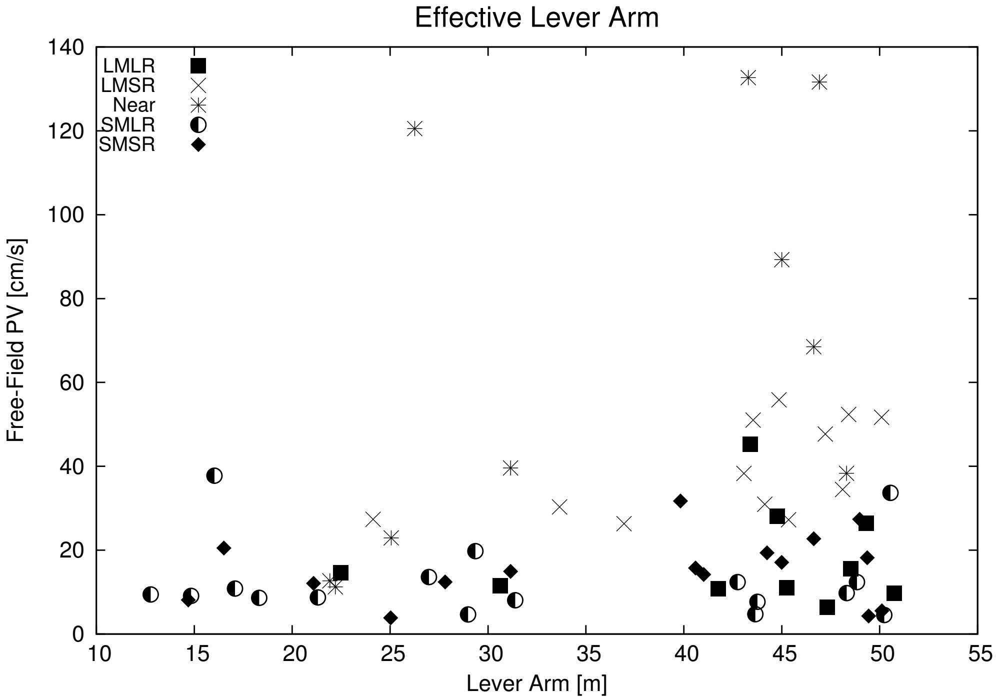

(a) rigid case

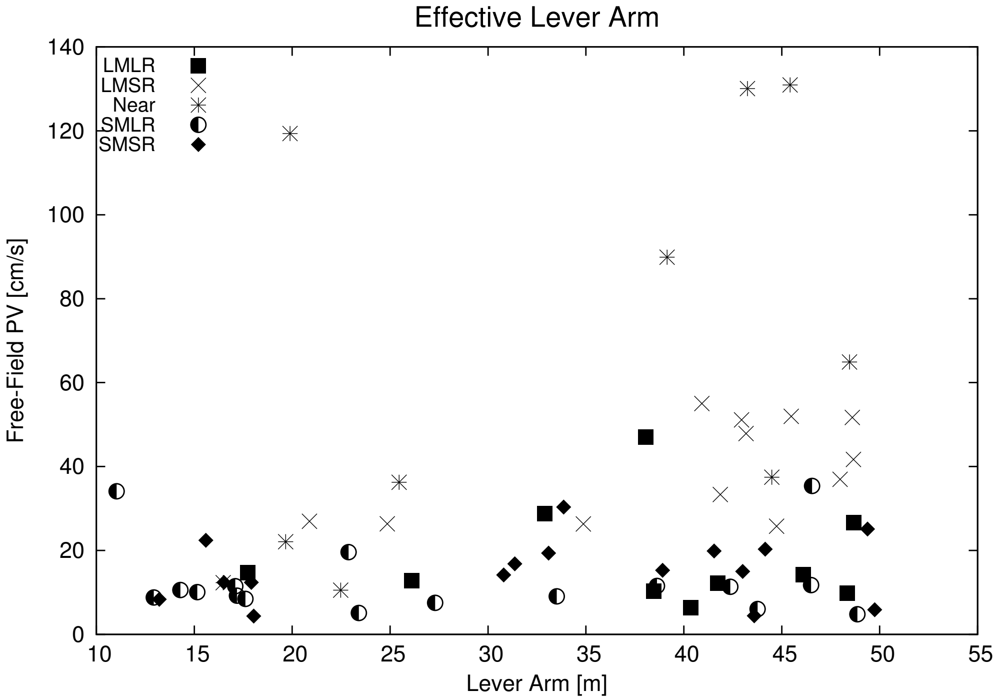

(b) $v_s = 200$ m/s case

Figure 5.8: Effective lever arm plots.

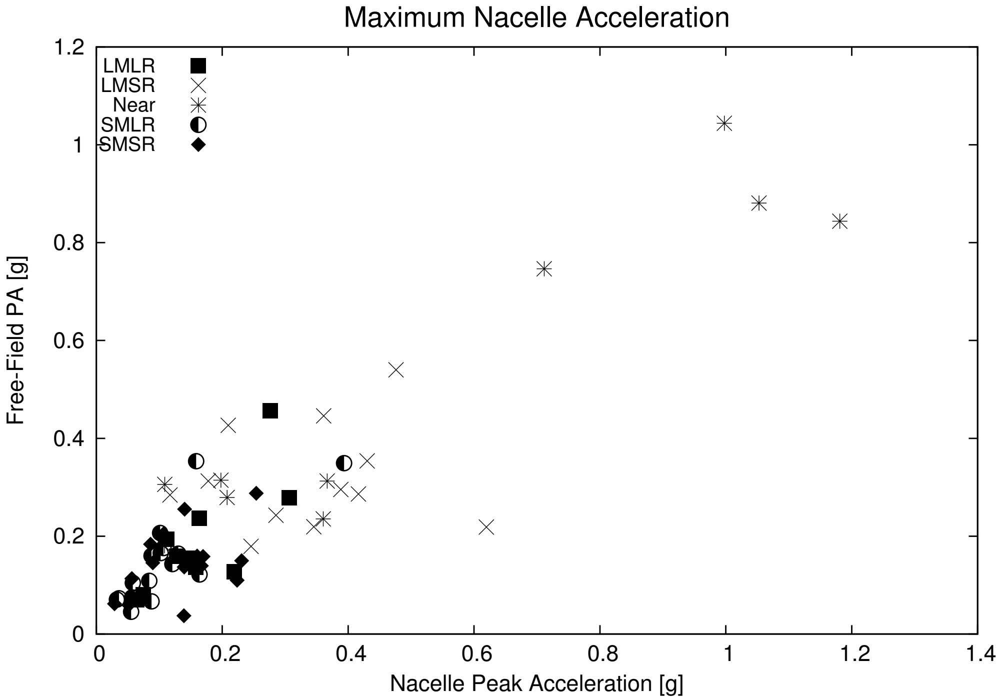

(a) rigid case

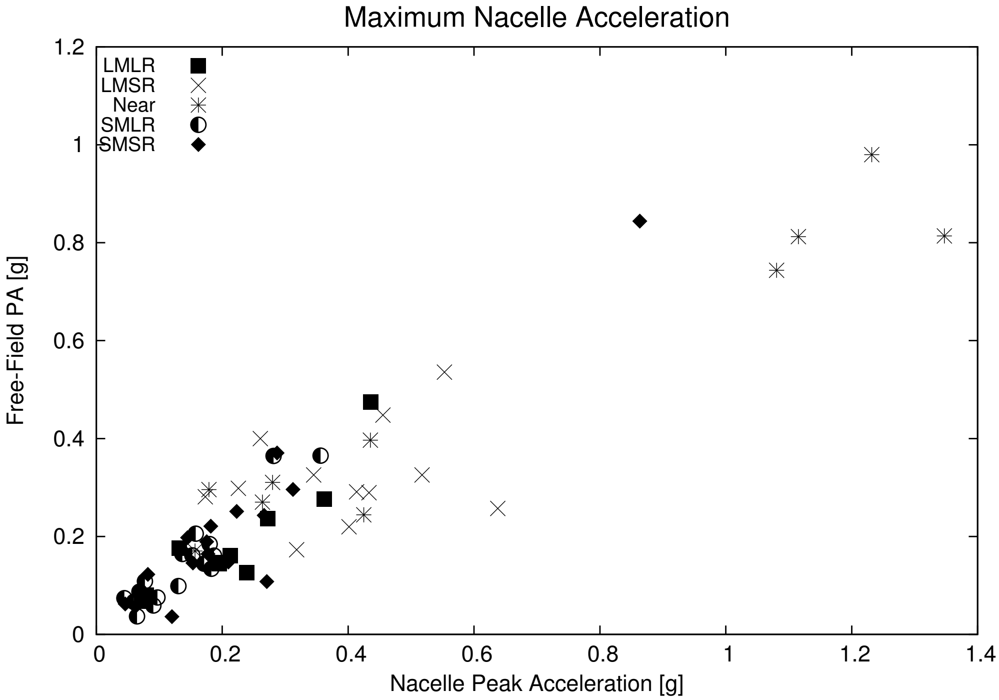

(b) $v_s = 200$ m/s case

Figure 5.9: Nacelle acceleration plots.

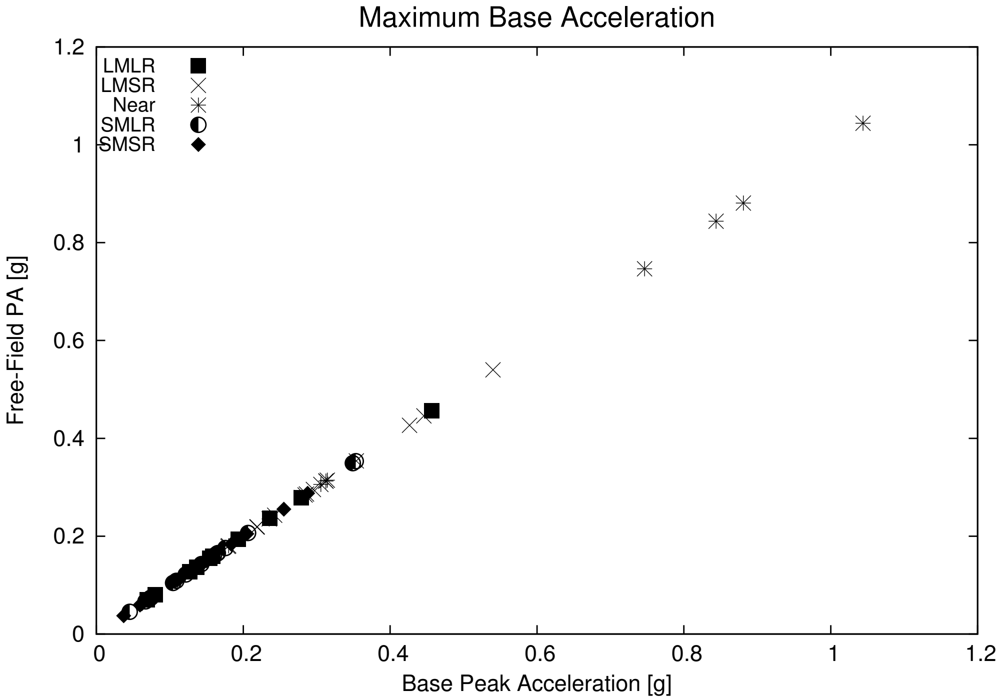

(a) rigid case

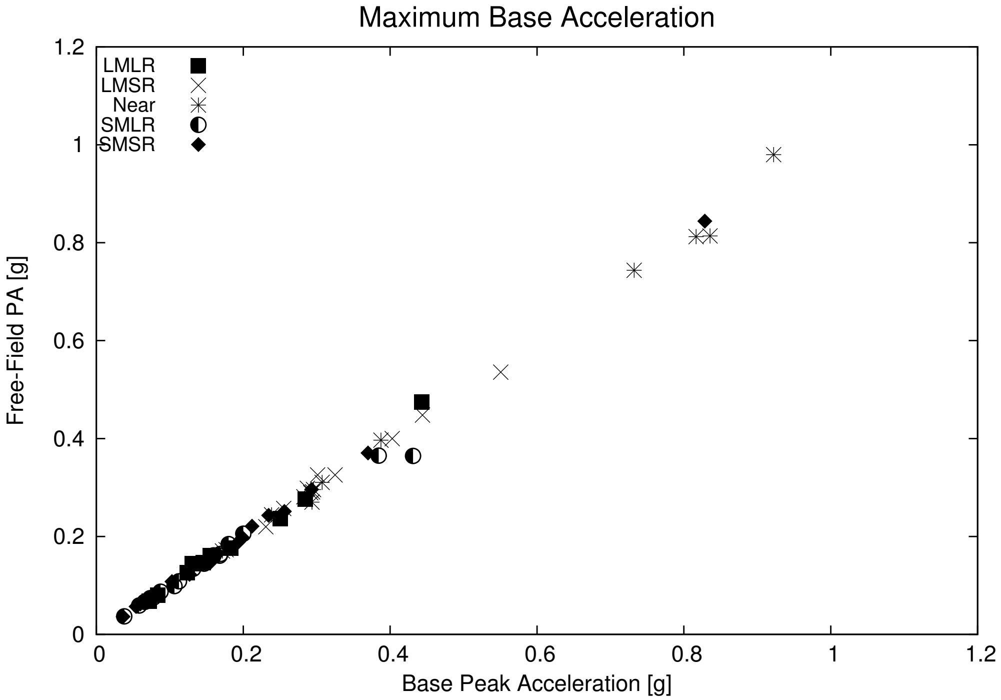

(b) $v_s = 200$ m/s case

Figure 5.10: Base acceleration plots.

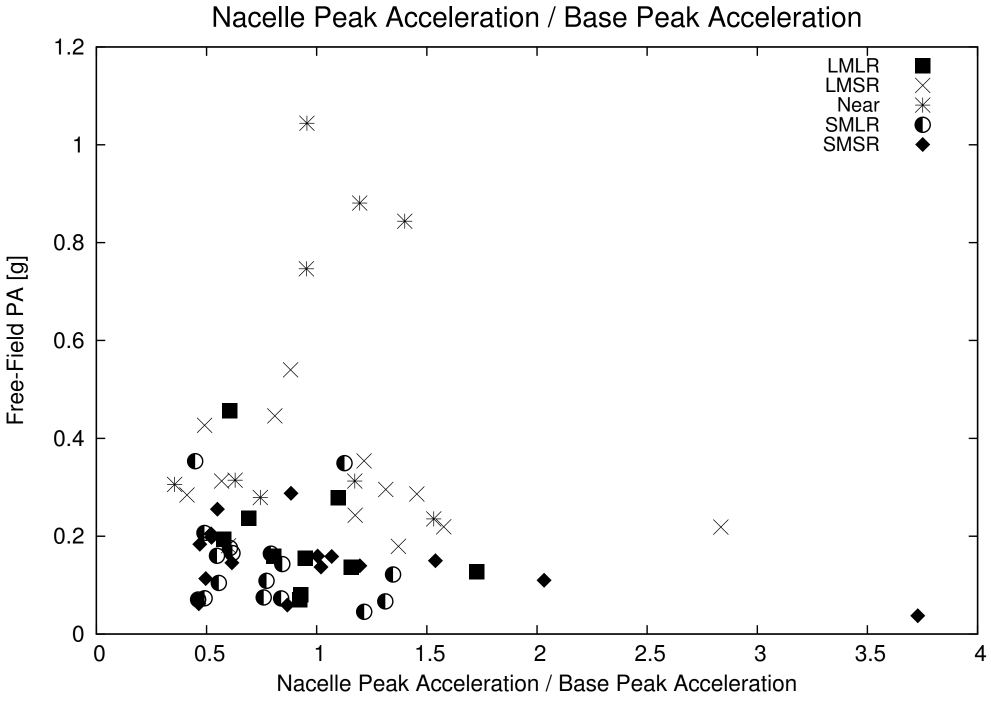

(a) rigid case

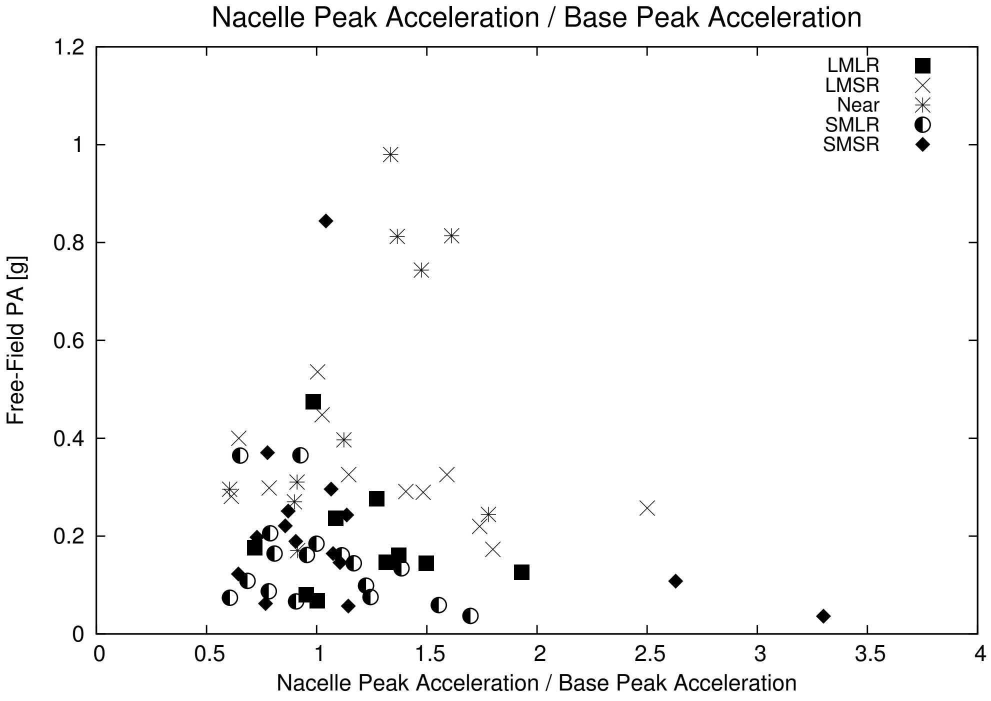

(b) $v_s = 200$ m/s case

Figure 5.11: Ratio of nacelle acceleration to base acceleration plots.

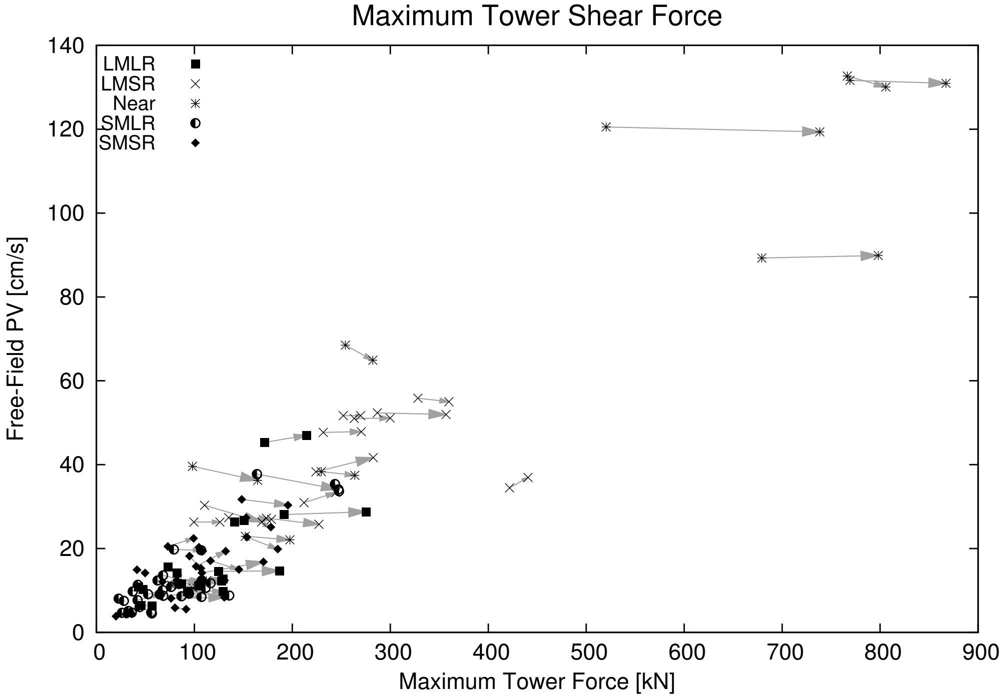

Figure 5.12: Change in peak shear force due to ground flexibility.

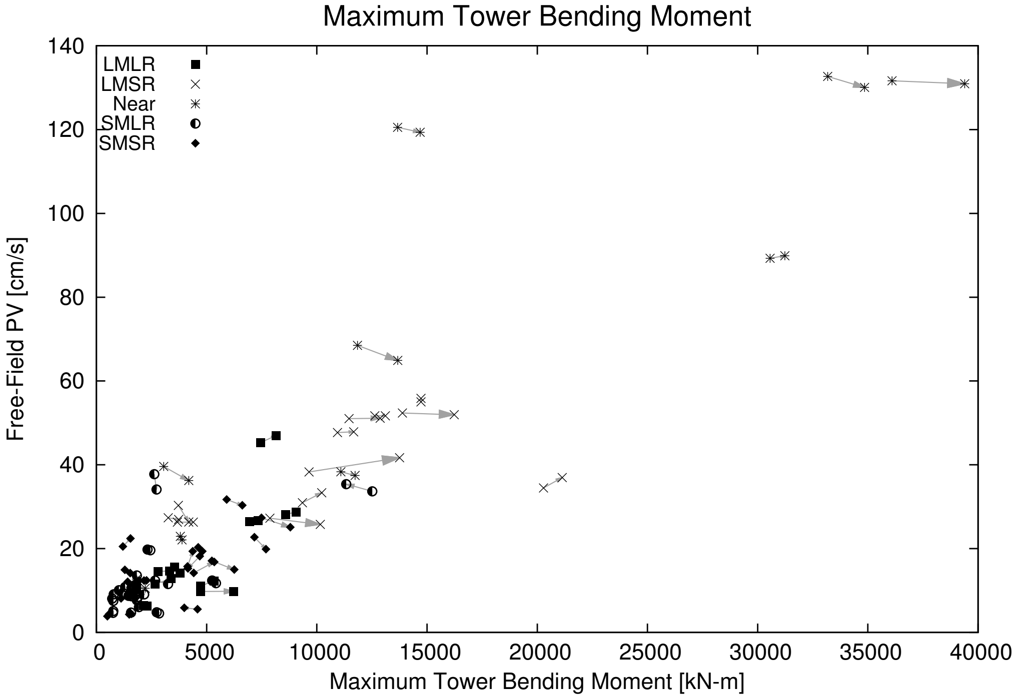

Figure 5.13: Change in peak bending moment due to ground flexibility.

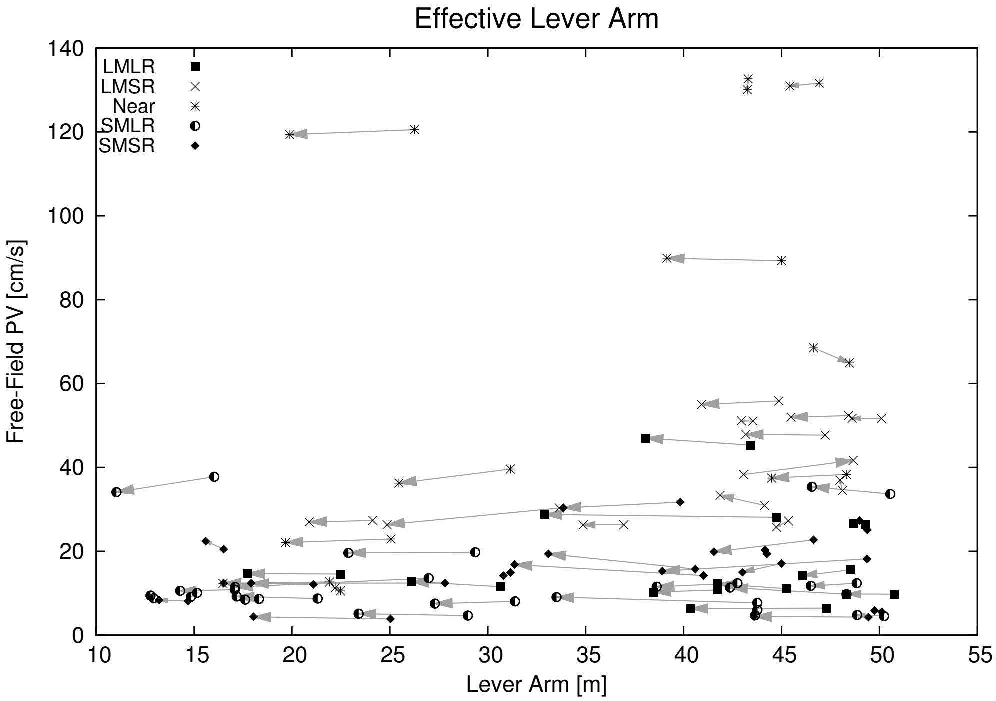

Figure 5.14: Change in effective lever arm due to ground flexibility.

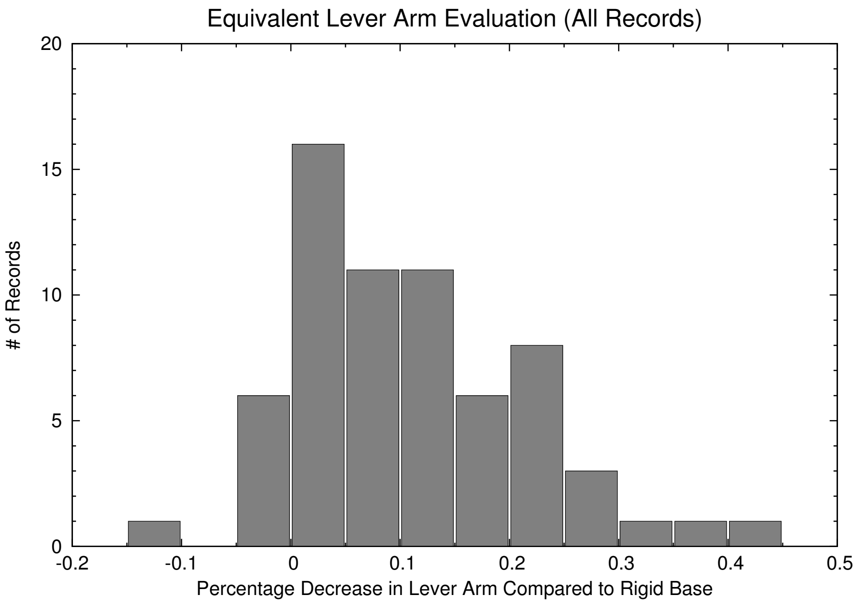

Figure 5.15: A histogram displaying the distribution of records as a function of percentage decrease in the effective lever arm due to lowering the shear wave velocity to $v_s = 200$ m/s (all motions).

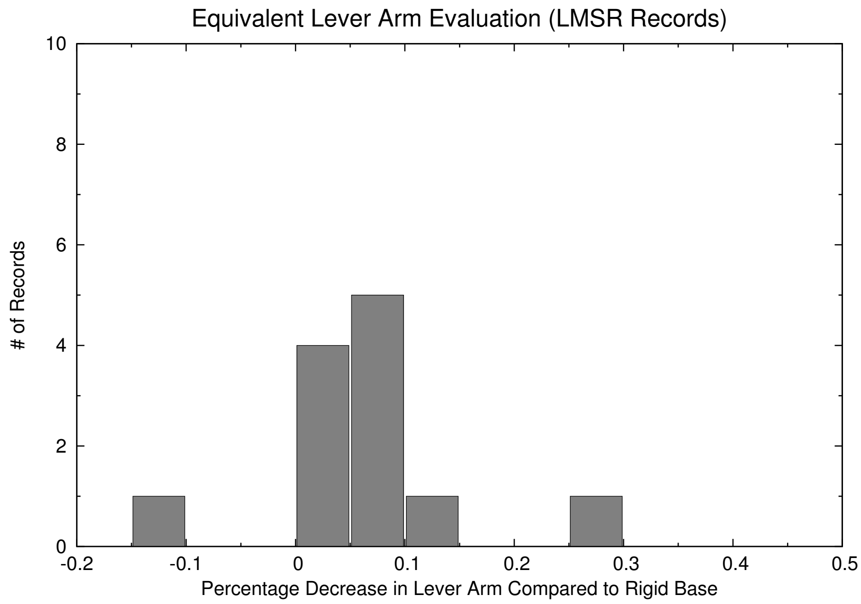

Figure 5.16: A histogram displaying the distribution of records as a function of percentage decrease in the effective lever arm due to lowering the shear wave velocity to $v_s = 200$ m/s (LMSR motions).

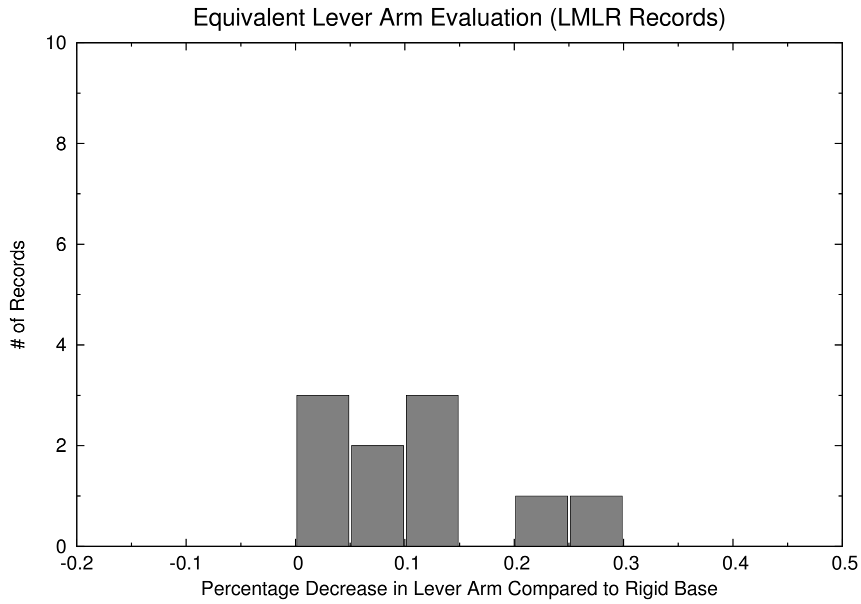

Figure 5.17: A histogram displaying the distribution of records as a function of percentage decrease in the effective lever arm due to lowering the shear wave velocity to $v_s = 200$ m/s (LMLR motions).

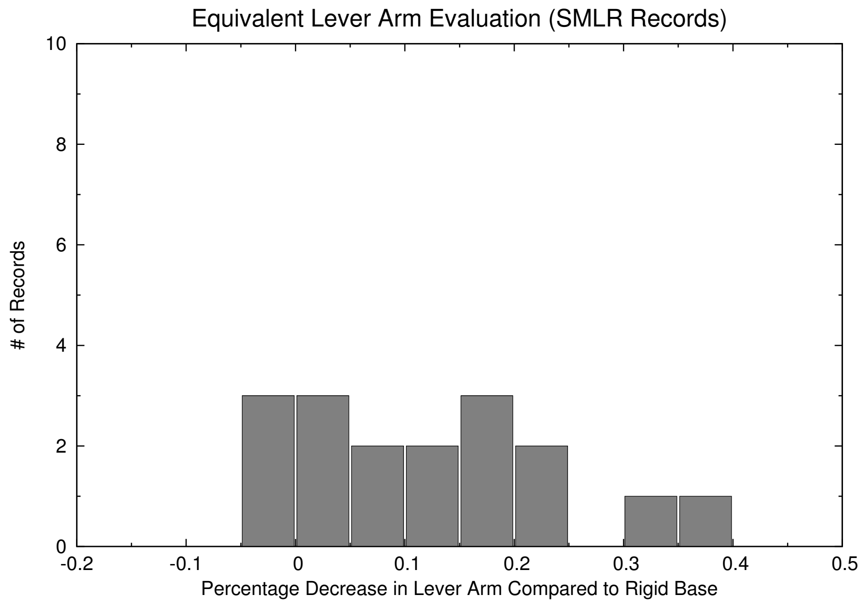

Figure 5.18: A histogram displaying the distribution of records as a function of percentage decrease in the effective lever arm due to lowering the shear wave velocity to $v_s = 200$ m/s (SMLR motions).

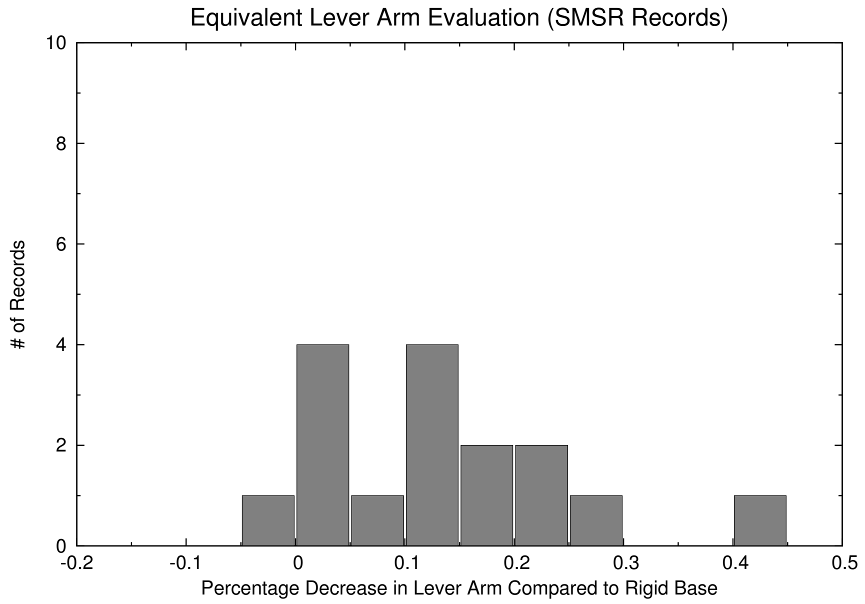

Figure 5.19: A histogram displaying the distribution of records as a function of percentage decrease in the effective lever arm due to lowering the shear wave velocity to $v_s = 200$ m/s (SMSR motions).

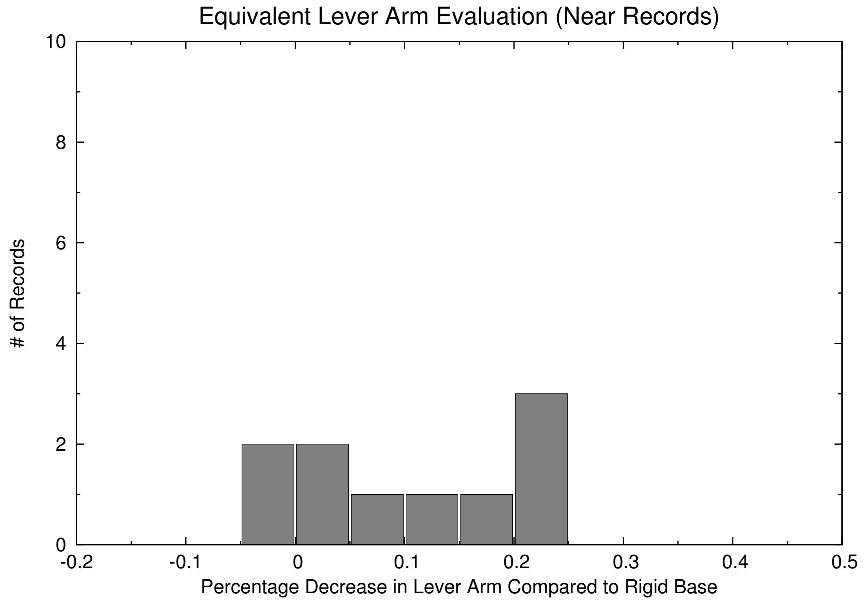

Figure 5.20: A histogram displaying the distribution of records as a function of percentage decrease in the effective lever arm due to lowering the shear wave velocity to $v_s = 200$ m/s (Near motions).

Bibliography

Bazeos, N., Hatzigeorgiou, G. D., Hondros, I. D., Karamaneas, H., Karabalis, D. L., and Beskos, D. E. (2002). "Static, seismic and stability analyses of a prototype wind turbine steel tower". *Engineering Structures*, 24(8):1015–1025.

Jonkman, J. M. and Buhl, Jr., M. L. (2005). "FAST User's Guide". Technical Report NREL/EL-500-38230, National Renewable Energy Laboratory.

Lu, J., Mackie, K., and Elgamal, A. (2011). *BridgePBEE Graphical User Interface OpenSees 3D Pushover and Earthquake Analysis of Single-Column 2-span Bridges, User Manual, Beta 1.0.* Pacific Earthquake Engineering Research Center, Berkeley, California, United States.

Luco, J. E. (1986). "On the relation between radiation and scattering problems for foundations embedded in an elastic half-space". *Soil Dynamics and Earthquake Engineering*, 5(2):97–101.

Mackie, K. R. and Stojadinović, B. (2005). “Fragility Basis for California Highway Overpass Bridge Seismic Decision Making”. Technical Report 2005/02, Pacific Earthquake Engineering Research Center.

Prowell, I. (2010). *An Experimental and Numerical Study of Wind Turbine Seismic Behavior*. PhD thesis, University of California, San Diego.

Prowell, I., Elgamal, A., and Lu, J. (2010). “Modeling the Influence of Soil Structure Interaction on the Seismic Response of a 5 MW Wind Turbine”. In *Fifth International Conference on Recent Advances in Geotechnical Earthquake Engineering and Soil Dynamics ans Symposium in Honor of Professor I.M. Idriss*, San Diego, CA.

Prowell, I., Elgamal, A., Lu, J., and Luco, J. E. (2009). “Modal properties of a modern wind turbine including SSI”. In *17th International Conference on Soil Mechanics & Geotechnical Engineering*, Alexandria, Egypt.

Risø (2002). *Guidelines of Design of Wind Turbines*. Det Norsk Veritas, Copenhagen and Wind Energy Department, Risø National Laboratory, Copenhagen, Denmark.

Varun, Assimaki, D., and Gazetas, G. (2009). “A simplified model for lateral response of large diameter caisson foundations-Linear elastic formulation”. *Soil Dynamics and Earthquake Engineering*, 29(2):268–291.

Chapter 6

Overall Summary and Conclusions

A study focused on data from harmonic excitation was undertaken. The effort aimed at assessment of the dynamic characteristics of a 900 kW wind turbine including soil-structure-interaction mechanisms. Among the main conclusions of this study are:

1. The recorded data was useful for the identification of resonant mode frequencies and mode shapes.
2. Limited insights were gleaned as relates to the involved damping mechanisms. Additional experimentation would be of value for this aspect of dynamic response.
3. Base translational and rotational springs were identified from the experimental data. It was shown that the significance of this base stiffness mechanism increases for higher bending modes of the turbine tower.
4. A study of influence of soil-structure interaction during seismic excitation for a soil of medium stiffness scenario indicated that the effective lateral force typically increased under softer soil conditions. This finding may have some implications regarding load demands on the wind turbine tower structure.

Additional numerical and experimental are needed to further quantify the involved mechanisms.

Appendix A

Filtering Algorithm

Some images of the raw data are displayed in this appendix as a way to explain the motivation for filtering. Furthermore, this appendix also describes in detail the algorithm used to filter the response histories that eventually led to the time histories seen in Chapter 2.

A.1 Details of Zero-Padded Tapered Acausal Filtering

In order to understand the motivation behind subjecting to data records to a filtering algorithm, raw time series data has been graphed and are displayed in Figures A.1-A.6. Please note that how these time histories were determined to be representations of the normal modes is explained in Chapter 2. Furthermore, using the terminology introduced in Chapter 2, all the data records shown in these graphs are made from dwell tests.

Not surprisingly, many of these records (especially towards the top of the tower) displayed a vigorous, palpable signal that resembled a sinusoid, though some signals were more greatly distorted. At first glance, it would seem that the lower modes appear to contain a large amount of of noise content when compared to the higher modes. More scientifically, the signal-to-noise ratio is on the order of 1 for the lower modes, while on the higher mode shapes, the signal is much greater than the noise. Since the shaker was known to be sending harmonic signals, the conjecture was that the strongest harmonic visible on the record was likely the manifestation of the shaker's influence as it propagated through the tower while the large amount of noise could have been due to any number of factors, including ambient wind induced vibrations. Since it was the desire of the author to perform an egalitarian analysis across all modes, it was decided that these lower harmonics would need to be enhanced in a manner that would place them approximately equal in clarity to the higher modes. Hence it was decided to filter these data records. As a self-check, filtered data records for the higher modes would validate the filtering algorithm as one that is neither causing any new distortion nor introducing new information if they did not appear to change very much from the original unprocessed data.

It is well known from the theory of filtering that filters may have the effect of introducing phase shifts between frequencies in the frequency domain. In practice, the introduced phase appears as a temporal shift for the signal in the time domain, as was the case with the signals used in this paper. The crests and troughs did not, in general, correspond with the unfiltered motions. Relying on such signals for information extraction seemed somewhat artificial since it was felt that the filtering should simply accentuate the background sinusoid instead of introducing any new information. The filter's effect would then have only exchanged one type of distortion (noise) for another (temporal) and would also impede correlating the data with notes taken on what was occurring during the experiment at that the moment in time. Therefore, an acausal (that is, zero-phase) filtering scheme was used. This technique is employed by first running the series through the filter as done previously in the (causal) case that resulted in the phase distortion. For illustrative purposes, let this unfiltered time series be represented by $S(t_k)$ where t_k is discretized time and $k = 1, 2, 3, \ldots, n$. The series is then transformed in such a way that the elements of the series are backwards, $\tilde{k} = n, n-1, n-2, \ldots, 1$ (the first entry becomes the last, the second becomes the penultimate, and so on) and this transformed signal is then run through the same filter. Then the series is transformed back into its original order. A simple schematic of this process is also

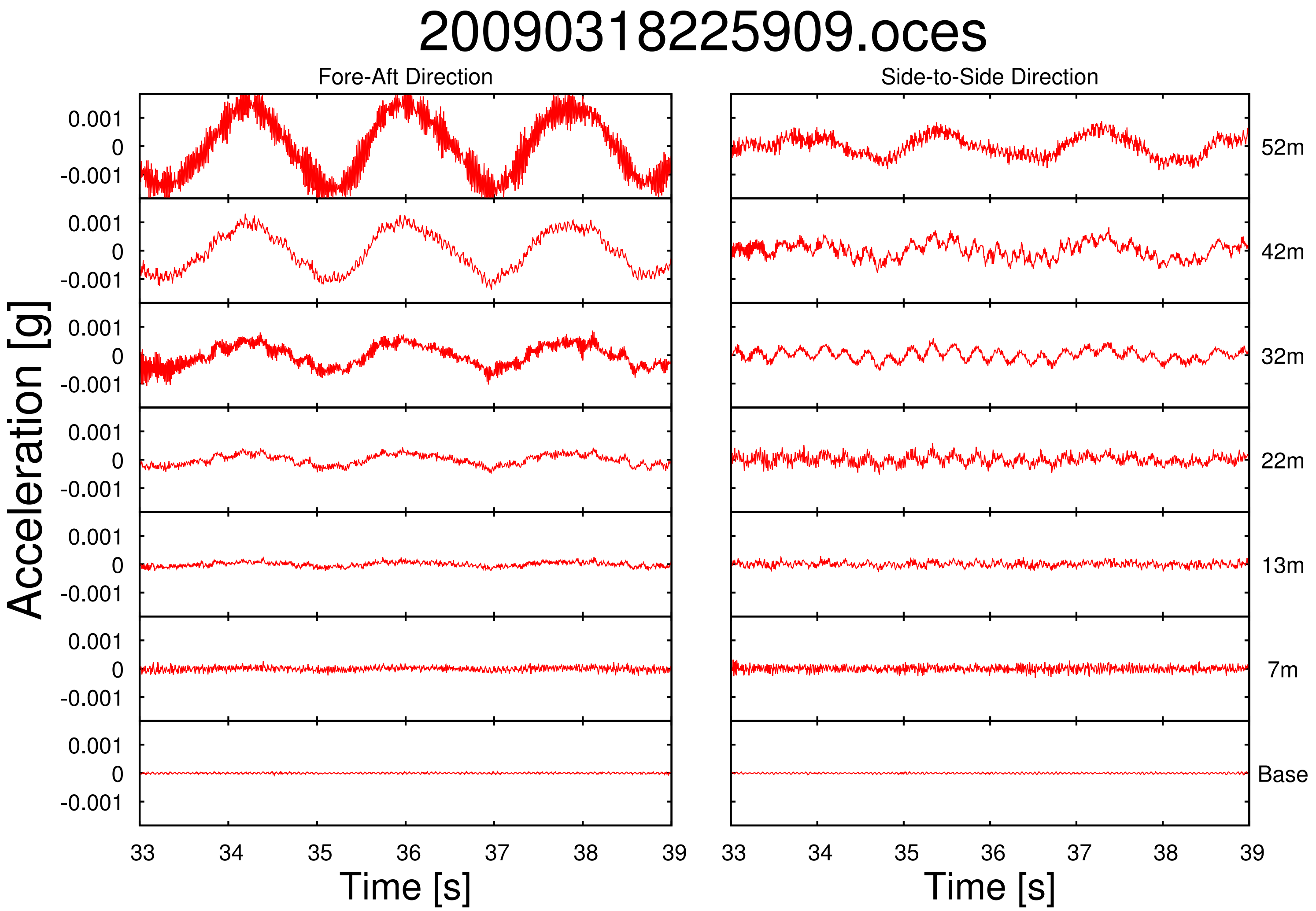

Figure A.1: First fore-aft mode, unfiltered time series.

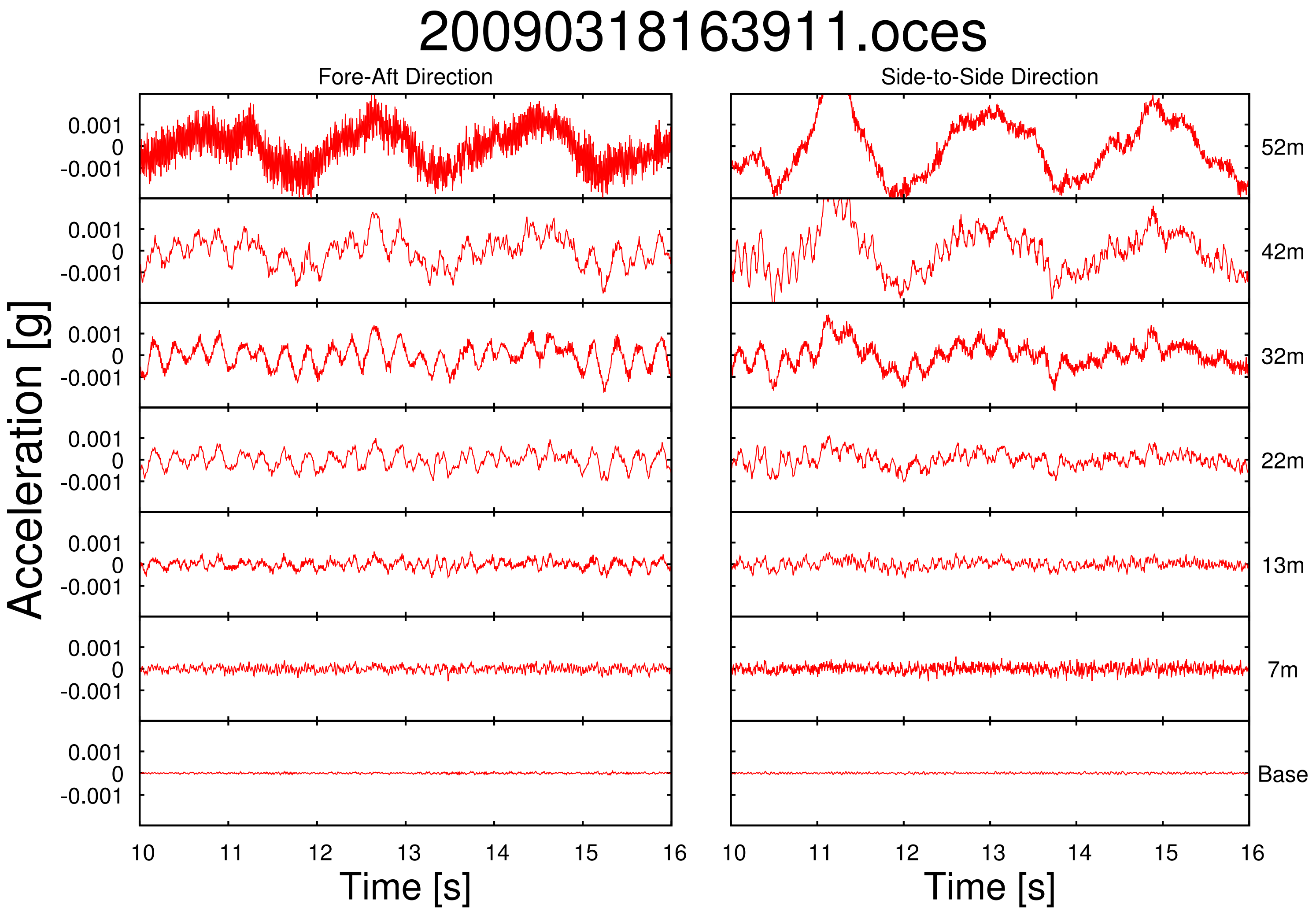

Figure A.2: First side-to-side mode, unfiltered time series.

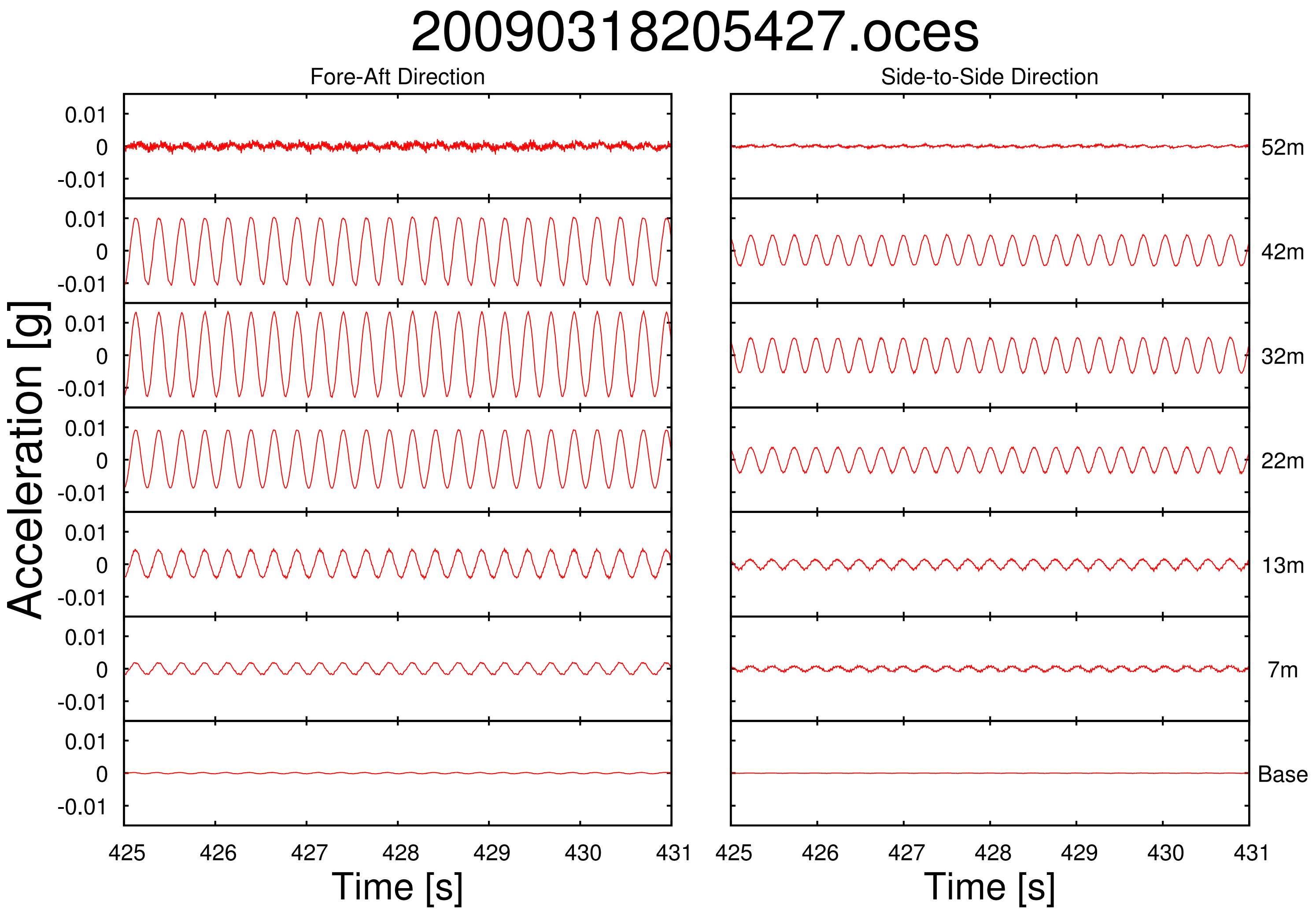

Figure A.3: Second fore-aft mode, unfiltered time series.

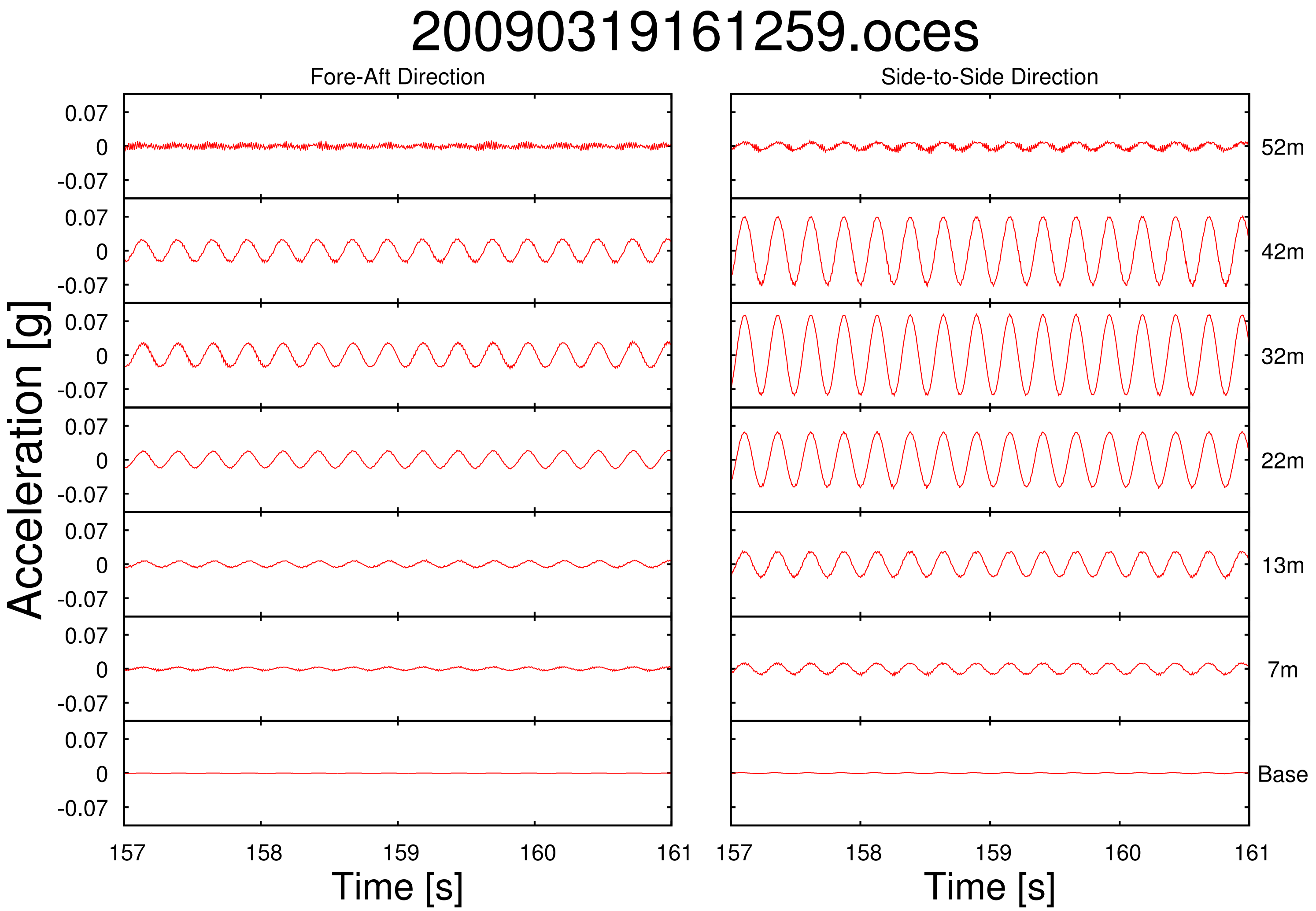

Figure A.4: Second side-to-side mode, unfiltered time series.

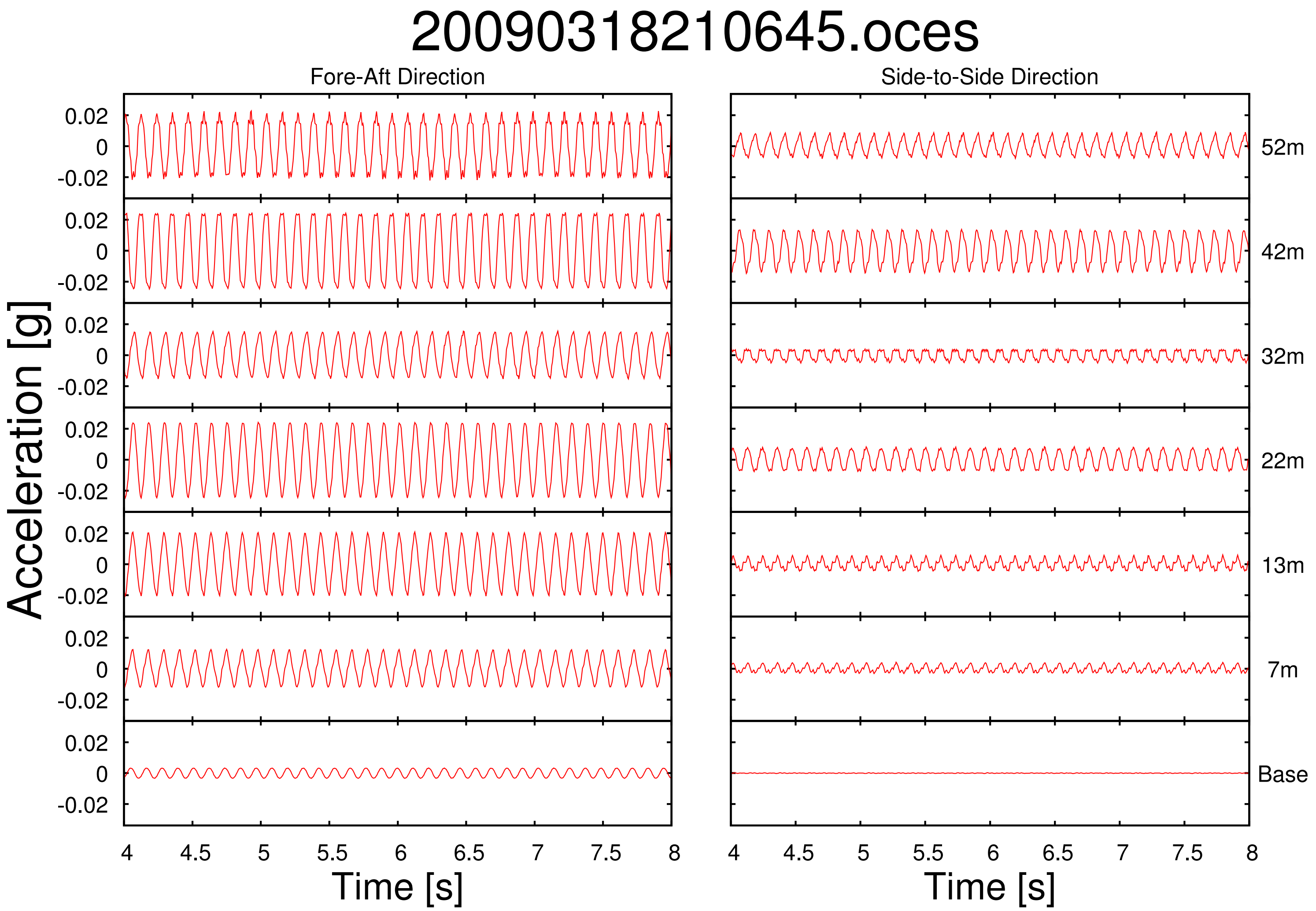

Figure A.5: Third fore-aft mode, unfiltered time series.

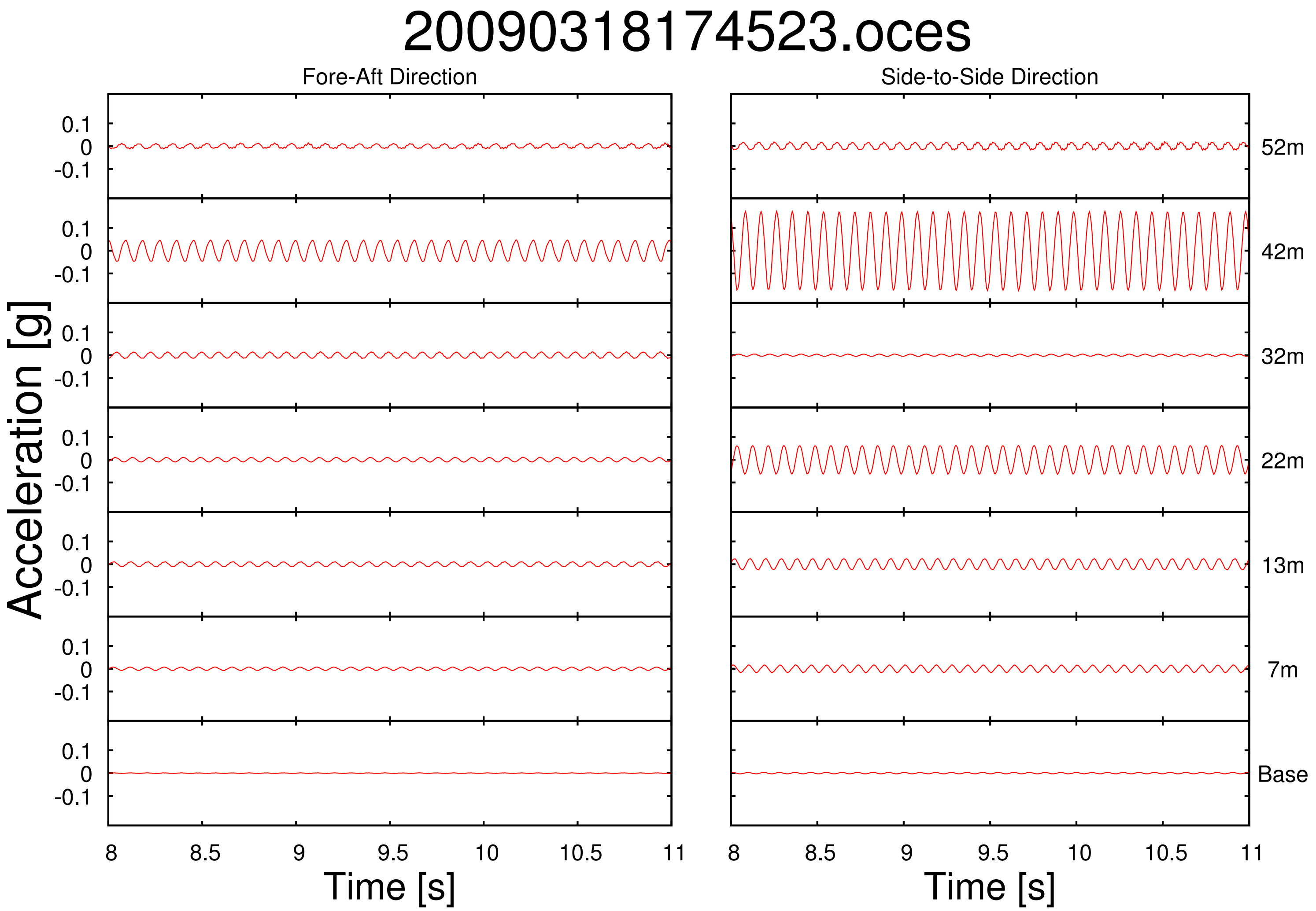

Figure A.6: Third side-to-side mode, unfiltered time series.

demonstrated in Figure A.7. This algorithm has the effect of cancelling the phase introduced in the first run and attenuating undesired frequencies more sharply (Converse and Brady, 1992).

A few more details were added to the algorithm to be consistent with similar acausal filtering schemes currently used in strong-motion signal processing. Implicitly or otherwise, all filtering procedures make assumptions about the time series at times before and after the given data record. The assumption implemented in the procedure for this report taken from Converse and Brady (1992) and Boore and Akkar (2003) wherein the time series was prepended and appended with a series of zeros. The term used to refer to such prepending and appending is "zero-padding." While a fair lower bound formula for the length of these zero vectors was suggested by Converse and Brady (1992), their report also indicates that small oscillations caused as a result of the zero-padding decrease with the length of the pads themselves. The length of the pads used in the filtering scheme was half that of the impulse length of the filters themselves. This value is on the same order of magnitude as the time series themselves, making padding somewhat overdone for our purposes (Boore, 2005; Boore and Akkar, 2003).

Secondly, the zero-padding necessitated what has been termed in the Converse and Brady (1992) article as "tapering." Tapering simply means that at the beginning of the time series, the first few data points are replaced zeros until the first zero crossing is reached. The same is done backwards from the end of the time history. This has the effect of smoothing the time series so that there are neither discontinuities nor sharp edges, which could introduce high frequency content into the signal (Boore, 2005).

To marginalize the presence of noise on the data records, a bandpass filtering scheme was applied to the available data records. Although in principle, a low-pass filter might have sufficed for imaging purposes, the data taken close to the base of the tower still displayed considerable low frequency activity when a Discrete Fourier transform was applied. The application of a bandpass filter was chosen so that the input signal would show better agreement with those along the higher portions of the tower.

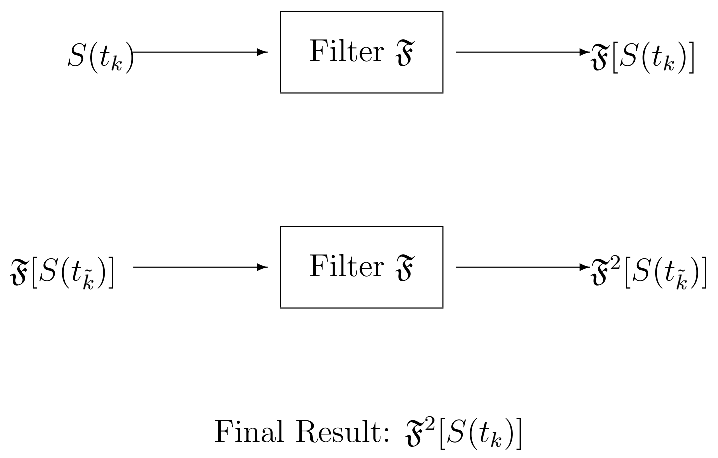

Figure A.7: Filtering algorithm schematic.

The specifications of the bandpass filter varied with each mode that was attempted to be imaged, and in one case, the geometry of the wind turbine also determined the filter design. From both the previous ambient vibration tests of Prowell (2010) and several plots of tower transfer functions from the forced vibration data, an approximate idea of the location of the resonant frequencies was obtained. These approximations served as a guide to in the selection of the passband frequencies (sometimes referred to as the cutoff frequencies) of the bandpass filters. It was also determined that the 1st natural frequency in the Fore-aft direction was sufficiently close to corresponding frequency in the Side-to-side direction that, for the purposes of the bandpass filter, there was no need to use different filter specifications for each direction in this mode. The same held true for the second natural frequency. Only in the third mode was there a sufficient distinction between the approximate natural frequencies in each direction that there was a necessity to apply a separate filter. Partially in homage to the methods used by PEER and partially because of their steep passband to stopband transition (Zaré and Bard, 2002), the filters were designed as Butterworth Infinite Impulse Response (IIR) filters, and were allowed a passband ripple of 0.1 decibels (dB). Table A.1 has been provided below with more characteristics detailing the construction of each of the filters. Figures A.8-A.11 has also been provided to complement Table A.1 and to further the understanding of these parameters. The magnitude of the signal attenuation as a function of frequency has been plotted for each filter. Notice that when each subfigure is compared to its respective specifications located on Table A.1, it is evident that the frequencies between the passband frequencies pass through unattenuated while and those outside the specified stopband frequencies have been reduced in magnitude by at least 80 dB as expected.

Having described the filtering algorithm at length, the author will now simply state that the algorithm was applied at each direction $i = 1, 2$ and for each elevation $j \in \{j\}$ of the response array.

Table A.1: Filter specifications used for processing the response signals.

Filter	Mode(s) Imaged	1st Stopband Frequency (Hz)	1st Passband Frequency (Hz)	Attenuation (dB)	2nd Passband Frequency (Hz)	2nd Stopband Frequency (Hz)	Attenuation (dB)
1	1st Fore-aft, 1st Side-to-side	0.20	0.40	80	0.65	0.95	80
2	2nd Fore-aft, 2nd Side-to-side	3.40	3.70	80	4.30	4.60	80
3	3rd Fore-aft	8.40	8.70	80	9.30	9.60	80
4	3rd Side-to-side	10.40	10.70	80	11.30	11.60	80

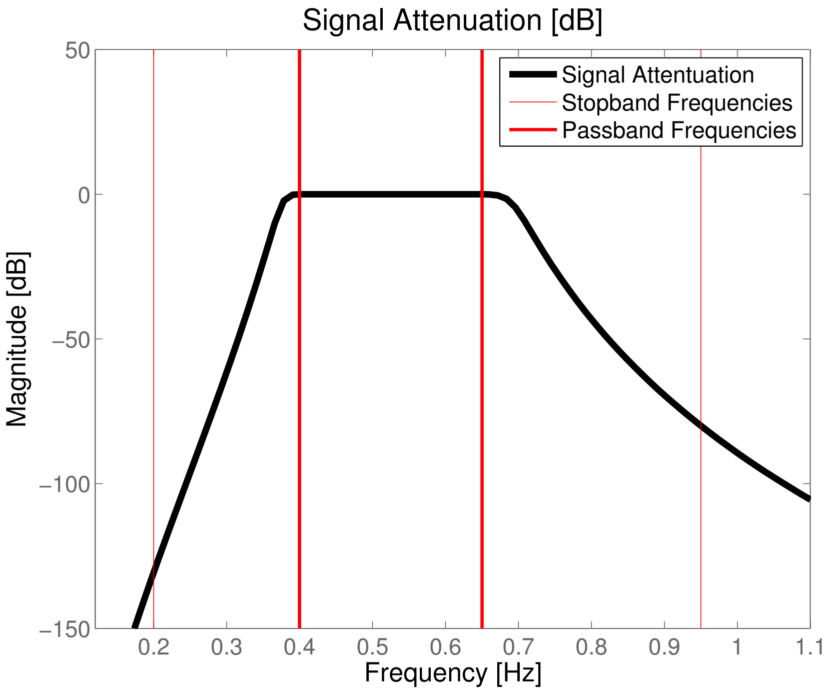

Figure A.8: Signal attenuation as a function of frequency for Filter 1.

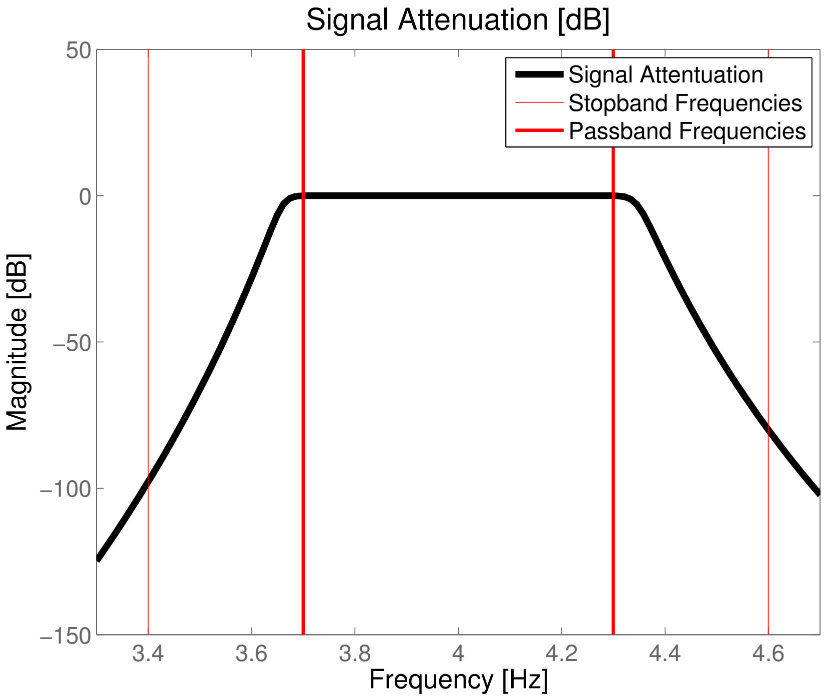

Figure A.9: Signal attenuation as a function of frequency for Filter 2.

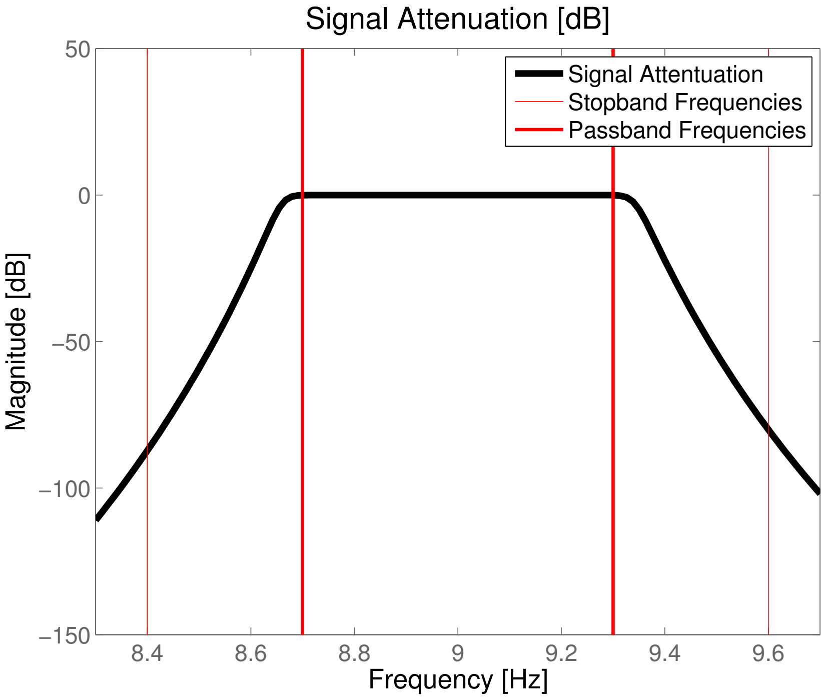

Figure A.10: Signal attenuation as a function of frequency for Filter 3.

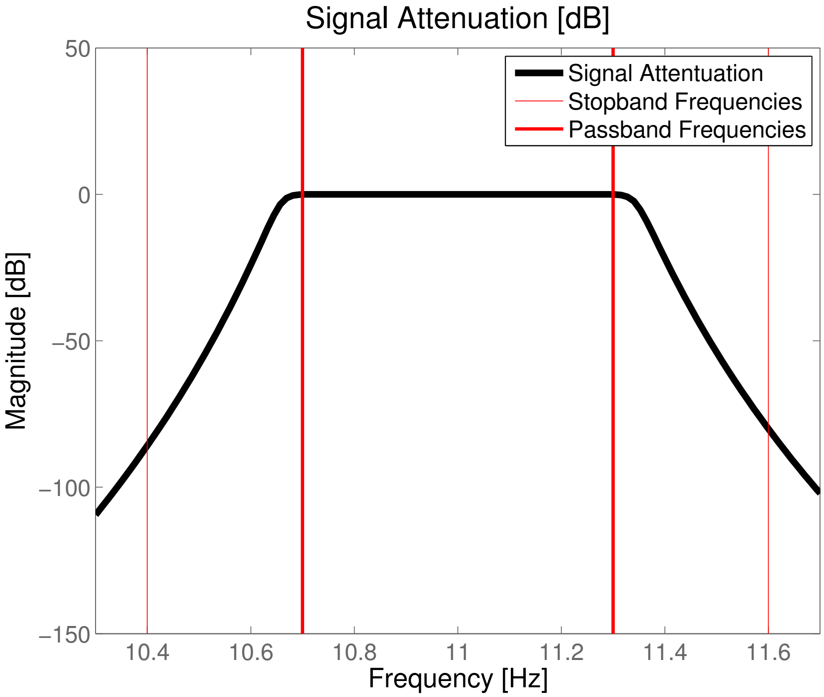

Figure A.11: Signal attenuation as a function of frequency for Filter 4.

Bibliography

Boore, D. M. (2005). "On Pads and Filters: Processing Strong-Motion Data". *Bulletin of the Seismological Society of America*, 95(2):745–750.

Boore, D. M. and Akkar, S. (2003). "Effect of causal and acausal filters on elastic and inelastic response spectra". *Earthquake Engineering & Structural Dynamics*, 32(11):1729–1748.

Converse, A. M. and Brady, A. G. (1992). "BAP: Basic Strong-Motion Accelerogram Processing Software; Version 1.0". Technical Report Open File report 92-296A, U.S. Geological Survey.

Lidierth, M. (2007). filtfilthd.m. `www.mathworks.com/matlabcentral/fileexchange/17061-filtfilthd`. MATLAB script.

Prowell, I. (2010). *An Experimental and Numerical Study of Wind Turbine Seismic Behavior*. PhD thesis, University of California, San Diego.

Zaré, M. and Bard, P. Y. (2002). "Strong motion dataset of Turkey: data processing and site classification". *Soil Dynamics and Earthquake Engineering*, 22(8):703–718.

Appendix B

Motions that Represent the First Bending Modes

This appendix provides additional commentary on the motions that were selected as representative of the first fore-aft and the first side-to-side bending modes. This discussion is meant to supplement that of the results section found in Chapter 3 to offer explanations as to why it was difficult to obtain accurate damping estimates with the method used in this thesis. Furthermore, this chapter provides a brief look into alternate motions that had base excitation at the first bending mode natural frequencies.

B.1 Discussion

The author has shown in Chapter 3 his method for estimating modal damping worked poorly for the first fore-aft and the first side-to-side bending modes. To further aid the reader in understanding possible sources of error for this method, Figures B.1 and B.2 have been provided.

Although it was the author's intention to use data records that dwelled on the natural frequency for an extended amount of time, this was not always possible. The amount of data records were limited, and for a variety of reasons (limited or odd data records), it was felt that these data records best represented the behavior at resonance for their respective modes. Figure B.1 shows that this record spent

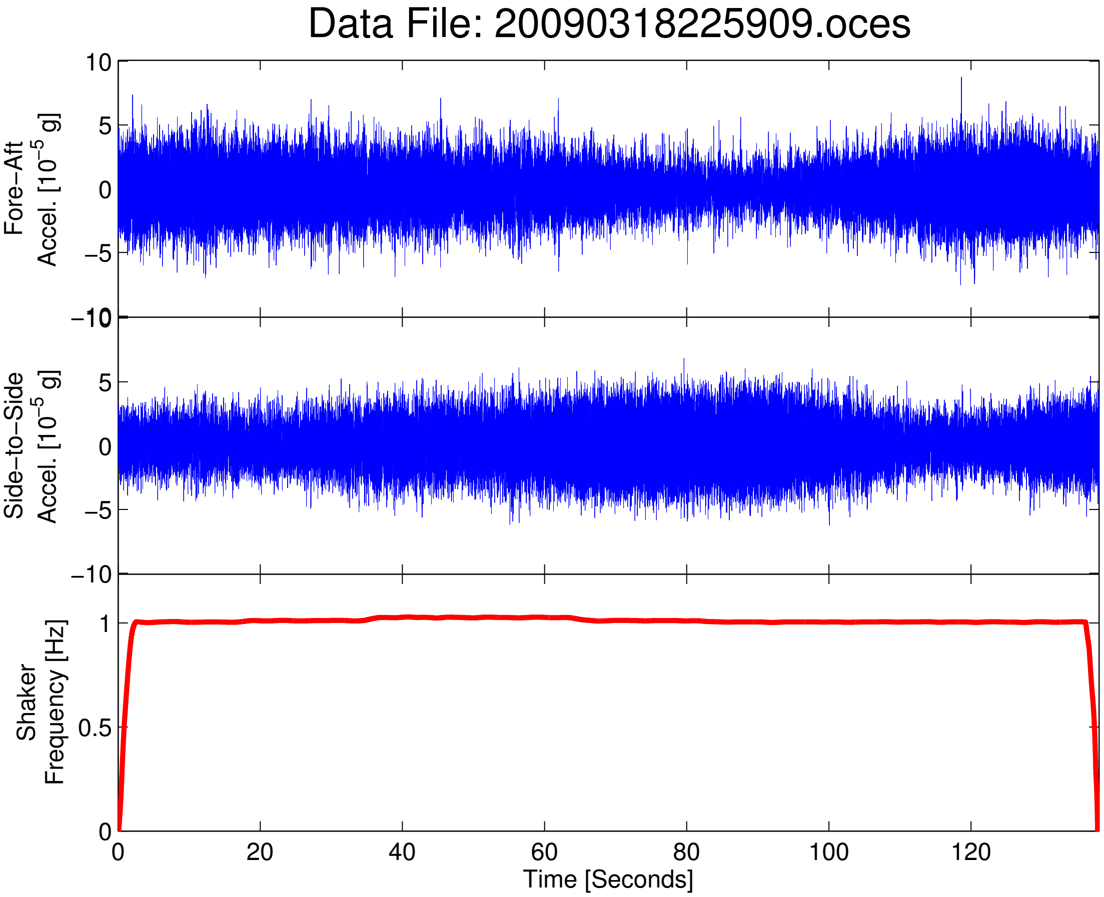

Figure B.1: A plot of the frequency and horizontal base acceleration as a function of time for the time history that represents the 1st fore-aft bending mode.

a large amount of time shaking, though not at a frequency of 0.55 Hz, which was decided as the first natural frequency of the first bending mode. Figure B.2 did spend some time shaking at around a frequency of 0.54 Hz, though it is difficult to claim that enough cycles passed in those 8 to 9 seconds of shaking to achieve a representative steady state response.

As it was stated in Chapter 3, it is believed that the sources error in the modal damping was due to the input excitation being mostly noise and ambient vibration instead of the shaker forcing. These graphs further reinforce that claim because they demonstrate that the actual input forcing largely did not correlate to the reported natural frequencies. In effect, any forcing that did appear in the records was largely filtered out as described in Chapter 2.

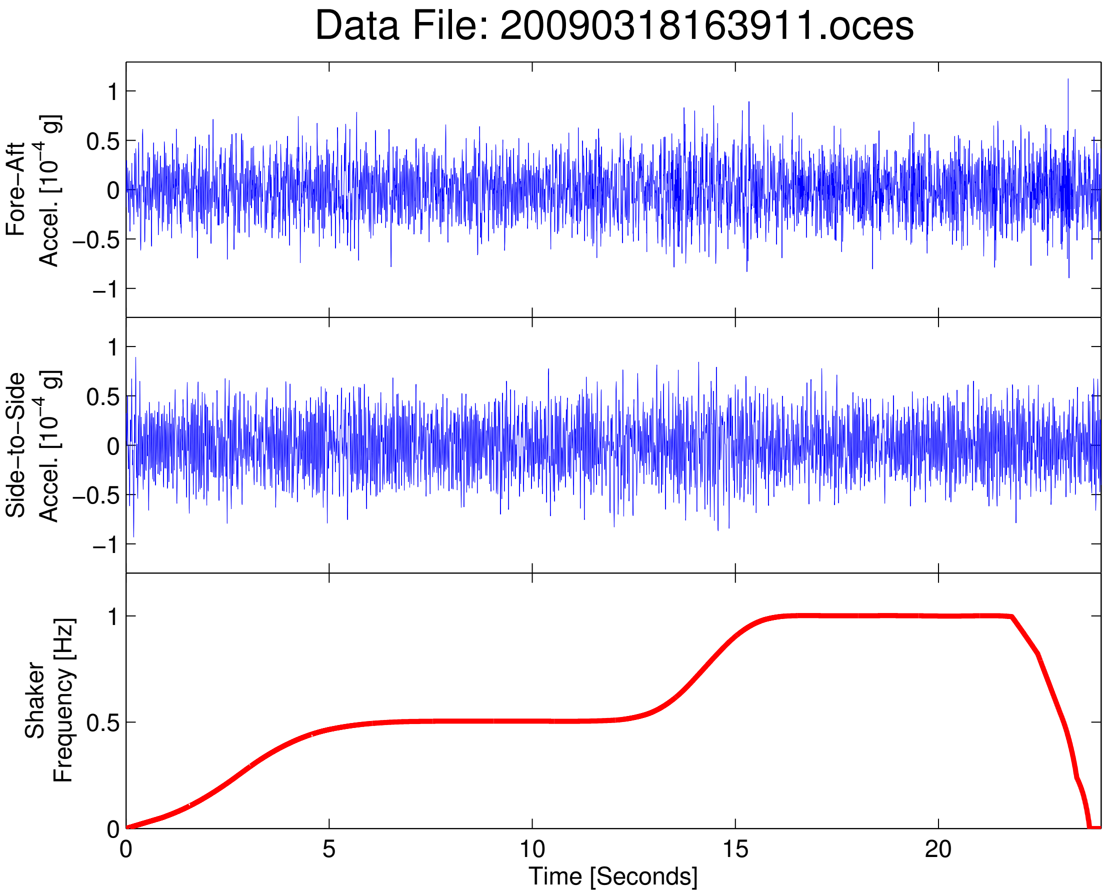

Figure B.2: A plot of the frequency and horizontal base acceleration as a function of time for the time history that represents the 1st side-to-side bending mode.

One lesson that can be gathered from this study is that good estimates for the natural frequencies and the mode shapes can be obtained by using these methods (they concur those found in Prowell, 2010), regardless of whether or not the forcing is close to natural frequency. This is certainly not the case with the damping ratios.

B.2 Alternate First Modes

The reader will recall that Chapter 2 included a brief description about selecting records that were felt to be representative of the bending modes. The reader was also exposed to discussion on how the records representing the first bending modes did not lend themselves to calculating reasonable estimates of the damping ratios. These records, while not ideal, were chosen over other records for various reasons. This section's inclusion in the thesis is meant to present alternative records that have captured motion at the first bending modes, provide an explanation as to why they were not selected for further analysis in this study, and attempt to discover some more general trends among the low frequency records.

The first record that will be discussed is the one shown in Figure B.3. It should be noted that the best records of the experimentation specify that this was a dwell with an intermediate amount of time spent shaking at the appropiate frequency range and that the shaker was oriented in the fore-aft direction during this trial. It is not difficult to see that the response in the side-to-side direction is actually greater! It was because of this that the author was hesitant to subject the record to further investigation. The record does highlight that at these low frequencies there exists a potential to have other agents of excitation, for instance, wind-induced excitation, create a response that may exceed that of the shaker.

The second record, shown in Figure B.4, was taken from a dwell with the shaker oriented in the side-to-side direction (again at the appropriate frequency range). In this case, the author chose to use a different record to represent the first side-to-side mode because the amplitudes displayed in this figure are very small. Indeed, the record analyzed in Chapter 2 had amplitudes that were about 100 times larger. If anything, this record reinforces what has already been seen above and argued in Chapters 2 and 3 concerning the shaker's inability to to provide much excitation at low frequencies.

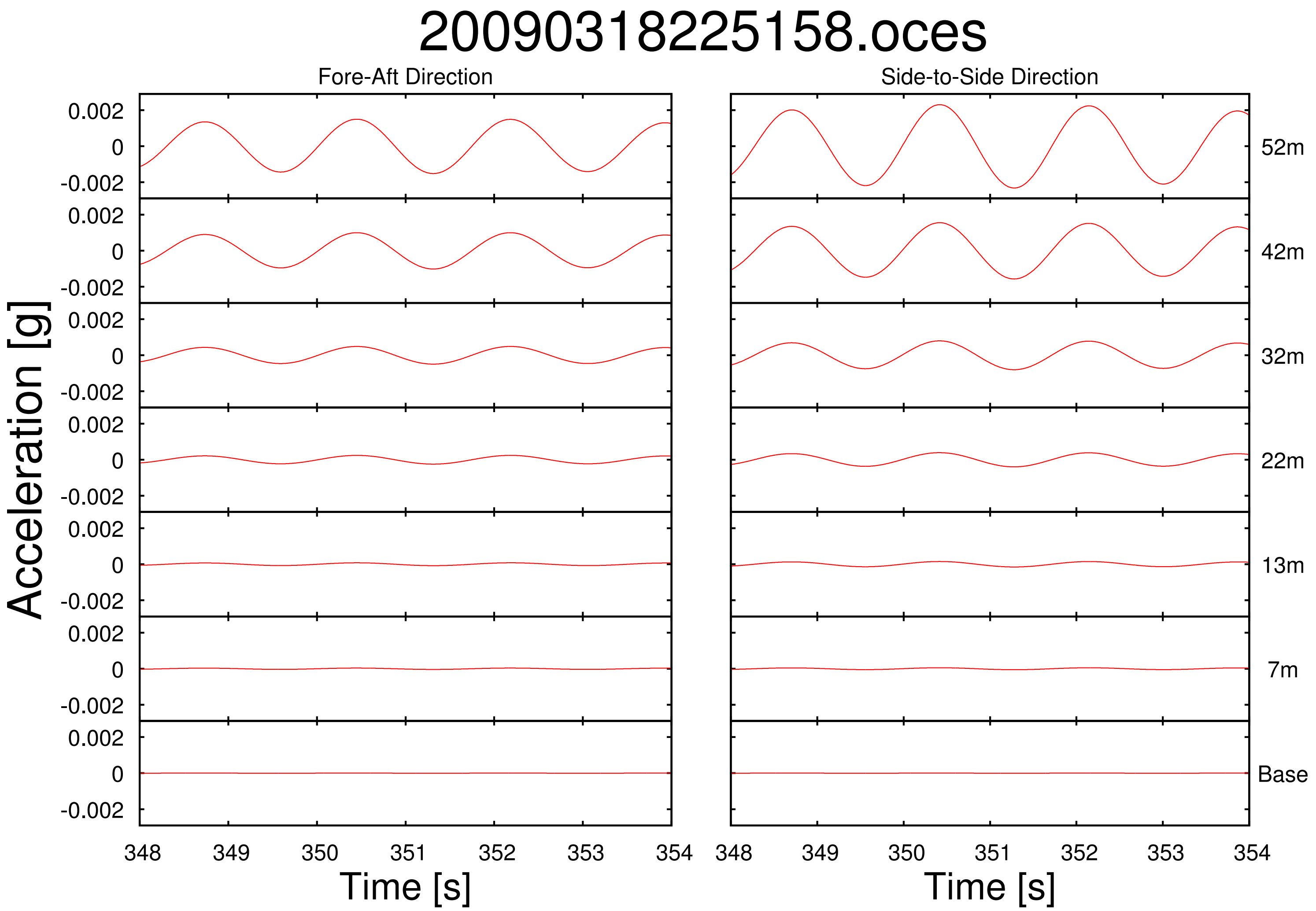

Figure B.3: Alternate first fore-aft, filtered time series. Observed frequency: 0.58 Hz.

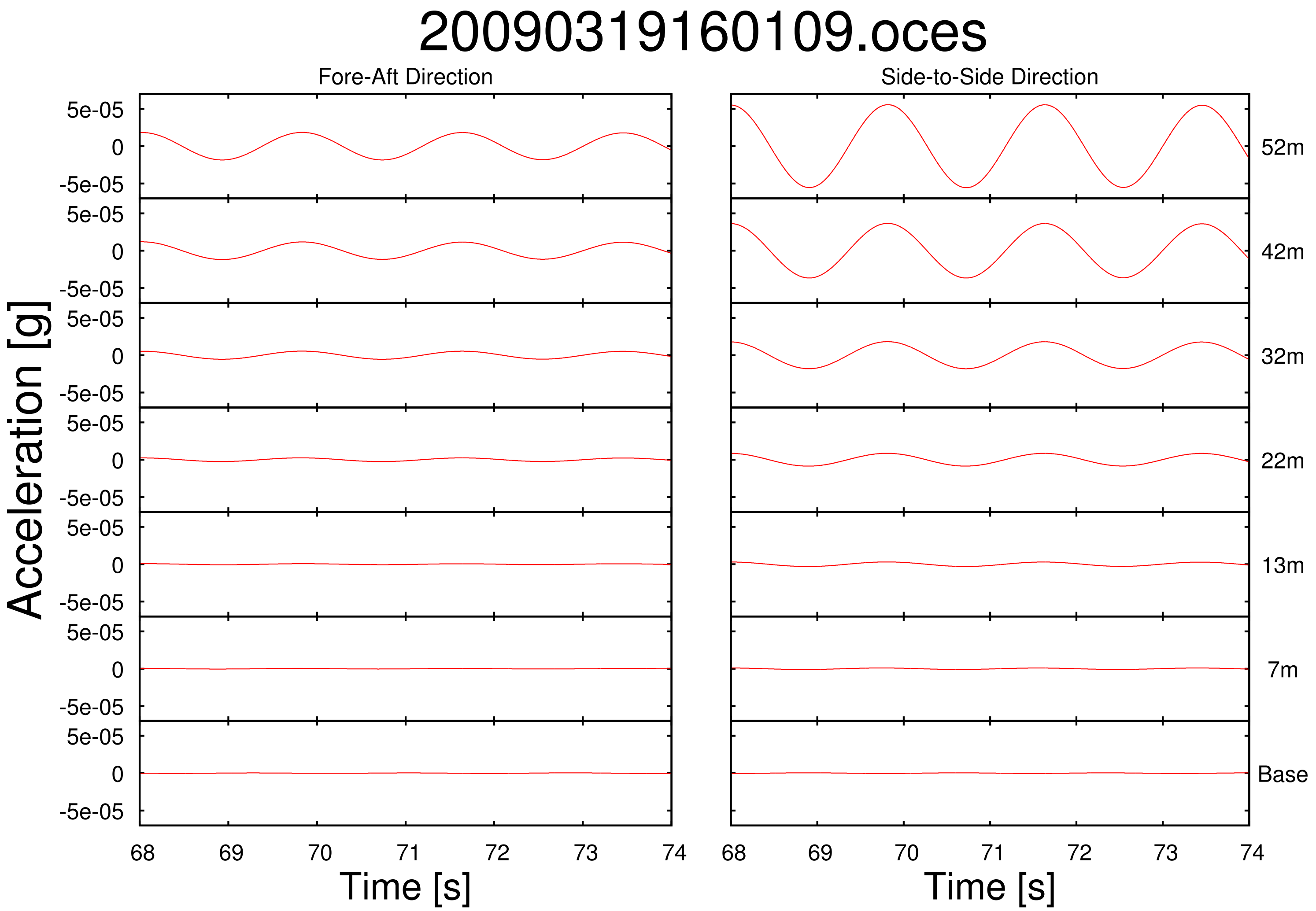

Figure B.4: Alternate first side-to-side, filtered time series. Observed frequency: 0.55 Hz.

Bibliography

Prowell, I. (2010). *An Experimental and Numerical Study of Wind Turbine Seismic Behavior*. PhD thesis, University of California, San Diego.

Appendix C

BridgePBEE Ground Motions

Appendix C is meant to work in tandem with Chapter 5. A table is included to give the reader more information regarding the 65 earthquake motions used in the earthquake excitation with soil study. A few graphics are also presented to show the agreement between the free-field motions in the two soil domains.

C.1 Data Concerning the Simulated Earthquakes

Table C.1 has been provided to give the reader more information about the earthquake records provided and used by BridgePBEE in Chapter 5 for the computer simulations that included soil structure interaction.

Much of this table has been shown before by Mackie and Stojadinović (2005). The content is not identical, however because as stated on the BridgePBEE website, the data records have been resampled from the PEER NGA database, and as such, the PGA quantities do not agree with those reported by Mackie and Stojadinović, in general.

All motions are from California earthquakes. The individual motions themselves are classified into five separate bins based on moment magnitude (Mw) and distance (which labeled as R in Mackie and Stojadinović (2005)). "SM" refers to a small magnitude ($5.8 \leq \mathrm{Mw} \leq 6.5$) while a large magnitude, "LM," is considered to be in the range $6.5 < \mathrm{Mw} \leq 7.2$. Similarly, a small distance "SR" is taken to be $15\,\mathrm{km} \leq \mathrm{R} \leq 30\,\mathrm{km}$, while a large distance, "LR," is taken to be

$30\,\text{km} < \text{R} \leq 60\,\text{km}$. The “Near” bin is composed of records in which the motion was measured at $\text{R} < 15\,\text{km}$.

There are two additional notes that the reader should be aware of. The first is that the convention used in Table C.1 is to use “longit.”, “trans.”, and “vert.” to mean longitudinal, transverse, and vertical, respectively. This has been adopted to because BridgePBEE uses this naming convention to specify the euclidean spatial directions. The same directions were then used in specifying each component of motion. For more information, consult the BridgePBEE user documentation in Lu et al. (2011).

Table C.1: BridgePBEE Earthquake Motions

Record ID	Event	Year	Moment Mag.	Class.	PGA [g]			
					long.	trans.	SRSS	vert.
PHN	Point Mugu	1973	5.8	SMSR	0.112	0.078	0.113	0.045
H-E12	Imperial Valley	1979	6.5	SMSR	0.143	0.112	0.150	0.062
H-CAL	Imperial Valley	1979	6.5	SMSR	0.128	0.078	0.137	0.055
H-E01	Imperial Valley	1979	6.5	SMSR	0.139	0.137	0.159	0.041
H-E13	Imperial Valley	1979	6.5	SMSR	0.112	0.138	0.139	0.041
H-WSM	Imperial Valley	1979	6.5	SMSR	0.074	0.109	0.110	0.085
H-CHI	Imperial Valley	1979	6.5	SMSR	0.269	0.256	0.288	0.210
A-SRM	Livermore	1980	5.8	SMSR	0.058	0.039	0.059	0.016
A-KOD	Livermore	1980	5.8	SMSR	0.154	0.076	0.159	0.038
Z-AGW	Morgan Hill	1984	6.2	SMSR	0.032	0.031	0.037	0.015
Z-GMR	Morgan Hill	1984	6.2	SMSR	0.184	0.112	0.184	0.410
Z-G02	Morgan Hill	1984	6.2	SMSR	0.155	0.201	0.205	0.566
Z-G03	Morgan Hill	1984	6.2	SMSR	0.194	0.200	0.255	0.367
A-WAT	Whittier Narrows	1987	6.0	SMSR	0.104	0.133	0.146	0.046
A-CAT	Whittier Narrows	1987	6.0	SMSR	0.042	0.059	0.062	0.037
A-W70	Whittier Narrows	1987	6.0	SMSR	0.198	0.151	0.198	0.077

Continued on the Next Page . . .

Table C.1 –Continued

Record ID	Event	Year	Moment Mag.	Class.	PGA [g]			
					long.	trans.	SRSS	vert.
B-ELC	Borrego	1942	6.5	SMLR	0.067	0.043	0.067	0.033
H-DLT	Imperial Valley	1979	6.5	SMLR	0.221	0.349	0.349	0.134
H-CC4	Imperial Valley	1979	6.5	SMLR	0.115	0.128	0.164	0.038
H-NIL	Imperial Valley	1979	6.5	SMLR	0.108	0.068	0.109	0.034
H-CMP	Imperial Valley	1979	6.5	SMLR	0.183	0.144	0.207	0.065
H-VCT	Imperial Valley	1979	6.5	SMLR	0.116	0.160	0.165	0.051
A-STP	Livermore	1980	5.8	SMLR	0.049	0.073	0.073	0.021
H-C08	Coalinga	1983	6.4	SMLR	0.097	0.100	0.104	0.024
H-C05	Coalinga	1983	6.4	SMLR	0.147	0.130	0.160	0.033
Z-HCH	Morgan Hill	1984	6.2	SMLR	0.070	0.070	0.075	0.119
SJB	Morgan Hill	1984	6.2	SMLR	0.044	0.036	0.045	0.052
Z-CAP	Morgan Hill	1984	6.2	SMLR	0.099	0.141	0.143	0.043
INO	N. Palm Springs	1986	6.0	SMLR	0.062	0.112	0.122	0.081
H06	N. Palm Springs	1986	6.0	SMLR	0.068	0.060	0.073	0.048
A-STC	Whittier Narrows	1987	6.0	SMLR	0.161	0.118	0.176	0.084
A-HAR	Whittier Narrows	1987	6.0	SMLR	0.058	0.070	0.071	0.025
A-BIR	Whittier Narrows	1987	6.0	SMLR	0.243	0.299	0.353	0.230

Continued on the Next Page . . .

Table C.1 –Continued

Record ID	Event	Year	Moment Mag.	Class.	PGA [g]			
					long.	trans.	SRSS	vert.
B-IVW	Superstition Hills	1987	6.7	LMSR	0.158	0.205	0.219	0.297
B-ICC	Superstition Hills	1987	6.7	LMSR	0.353	0.250	0.354	0.119
B-WSM	Superstition Hills	1987	6.7	LMSR	0.168	0.212	0.243	0.190
AGW	Loma Prieta	1989	6.9	LMSR	0.168	0.159	0.179	0.083
HCH	Loma Prieta	1989	6.9	LMSR	0.246	0.214	0.286	0.212
HDA	Loma Prieta	1989	6.9	LMSR	0.269	0.279	0.296	0.153
SVL	Loma Prieta	1989	6.9	LMSR	0.199	0.206	0.219	0.096
FLE	Northridge	1994	6.7	LMSR	0.160	0.237	0.284	0.108
LOS	Northridge	1994	6.7	LMSR	0.411	0.477	0.540	0.320
PEL	Northridge	1994	6.7	LMSR	0.231	0.358	0.427	0.139
FAR	Northridge	1994	6.7	LMSR	0.273	0.243	0.313	0.184
RO3	Northridge	1994	6.7	LMSR	0.284	0.441	0.446	0.312
A-ELC	Borrego Mtn.	1968	6.8	LMLR	0.127	0.057	0.127	0.030
SLC	Loma Prieta	1989	6.9	LMLR	0.189	0.277	0.279	0.090
CEN	Northridge	1994	6.7	LMLR	0.455	0.321	0.457	0.108
DWN	Northridge	1994	6.7	LMLR	0.158	0.230	0.236	0.132
PIC	Northridge	1994	6.7	LMLR	0.103	0.182	0.193	0.064

Continued on the Next Page . . .

Table C.1 –Continued

Record ID	Event	Year	Moment Mag.	Class.	PGA [g]			
					long.	trans.	SRSS	vert.
PHP	Northridge	1994	6.7	LMLR	0.062	0.066	0.080	0.039
LOA	Northridge	1994	6.7	LMLR	0.086	0.152	0.154	0.054
DEL	Northridge	1994	6.7	LMLR	0.136	0.122	0.137	0.056
VER	Northridge	1994	6.7	LMLR	0.119	0.150	0.159	0.063
SOR	Northridge	1994	6.7	LMLR	0.063	0.067	0.070	0.051
I-ELC	Imperial Valley	1940	7.0	Near	0.309	0.215	0.313	0.188
C08	Parkfield	1966	6.1	Near	0.226	0.259	0.306	0.101
H-ECC	Imperial Valley	1979	6.5	Near	0.211	0.234	0.235	0.223
H-CXO	Imperial Valley	1979	6.5	Near	0.269	0.200	0.279	0.176
Z-HVR	Morgan Hill	1984	6.2	Near	0.155	0.305	0.314	0.109
A-SOR	Whittier Narrows	1987	6.0	Near	0.137	0.179	0.180	0.131
JEN	Northridge	1994	6.7	Near	0.570	0.982	1.044	0.675
NWH	Northridge	1994	6.7	Near	0.583	0.590	0.747	0.548
SYL	Northridge	1994	6.7	Near	0.604	0.843	0.844	0.535
SCS	Northridge	1994	6.7	Near	0.612	0.865	0.881	0.550

C.2 Free-Field Motion Comparisons

As was discussed in Chapter 5, synthetic motions were input at the base of the BridgePBEE model in such a manner that the same free-field motion would be produced in both the elastic and rigid soil cases. Figures C.1 and C.2 are displayed to show some of the results that are possible with this method that utilizes the transfer function of the soil.

Of note to a reader who may wish to replicate a similar process to that taken in this document is the fact that there are occasions where very weak acceleration, as in the case of the first few and last few seconds of an earthquake motion, are at times difficult to reproduce. Indeed some numerical experimentation with this method would likely benefit not just earthquake simulation, but the field of vibrations as a whole.

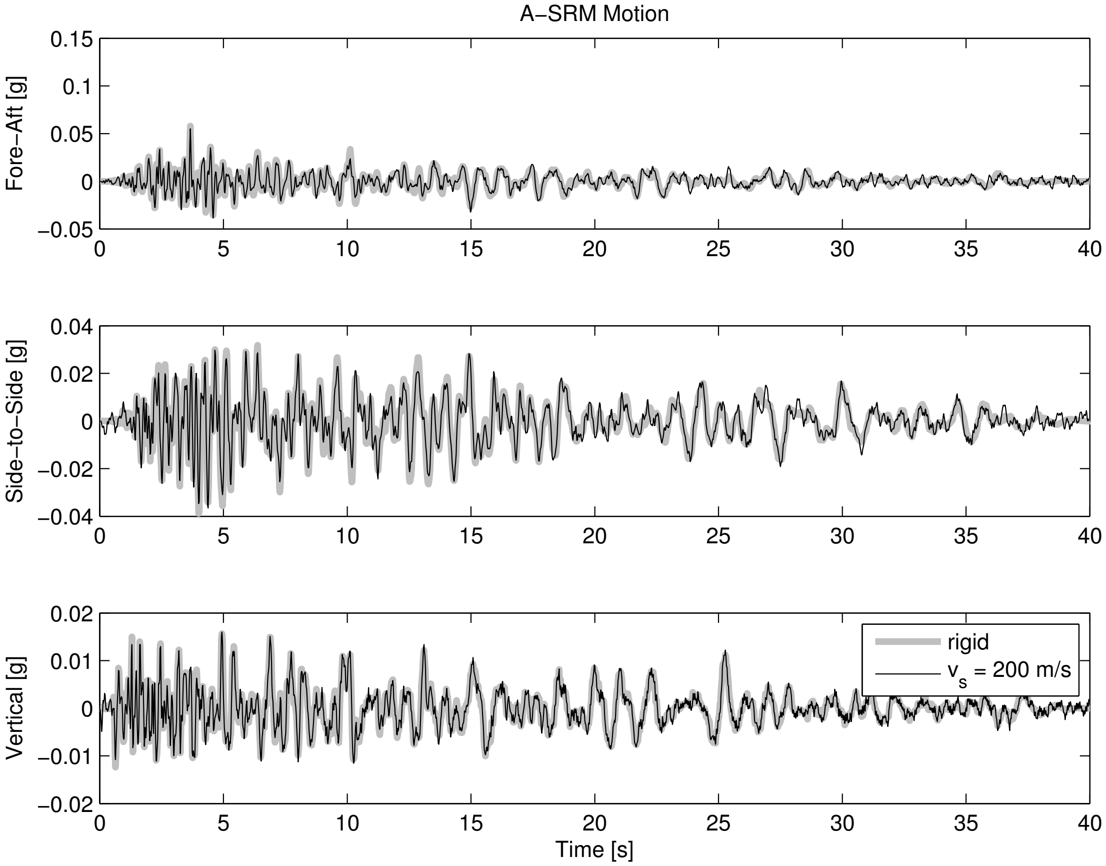

Figure C.1: SMSR comparison of free-field motion.

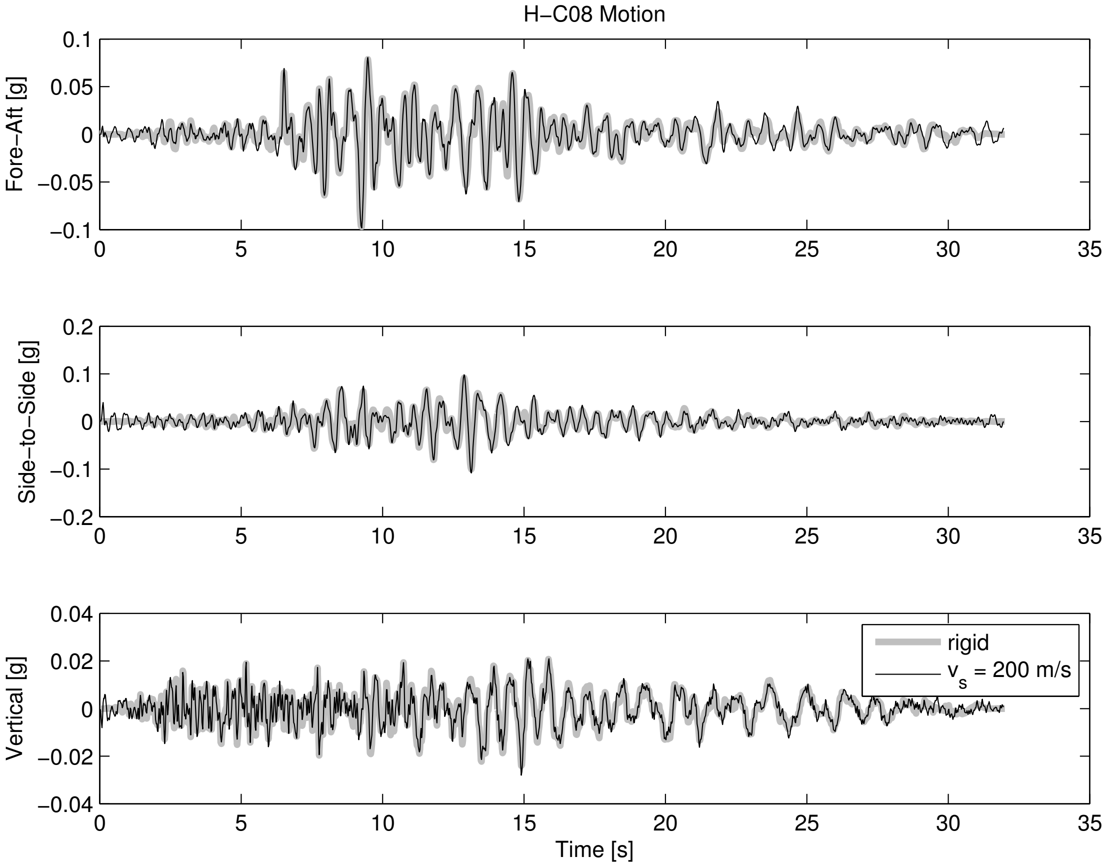

Figure C.2: SMLR comparison of free-field motion.

C.3 Input Motions

C.3.1 A Note About Simulated Motions

In Chapter 5, the reader was informed that a transfer function was used to create synthetic motions to apply at the base of the soil domain so that a particular free-field motion would be obtained. This free-field motion was supposed to correspond to the free-field motion that results when the original earthquake record is applied to a rigid soil domain.

One of the details that was noticed with this approach was that the synthesized input motion appeared to have a large amount of high frequency content. A case of this can observed in the grey motions seen in the bottom half of Figure C.3. For those interested, the motion seen in the graph is one of the horizontal compo-

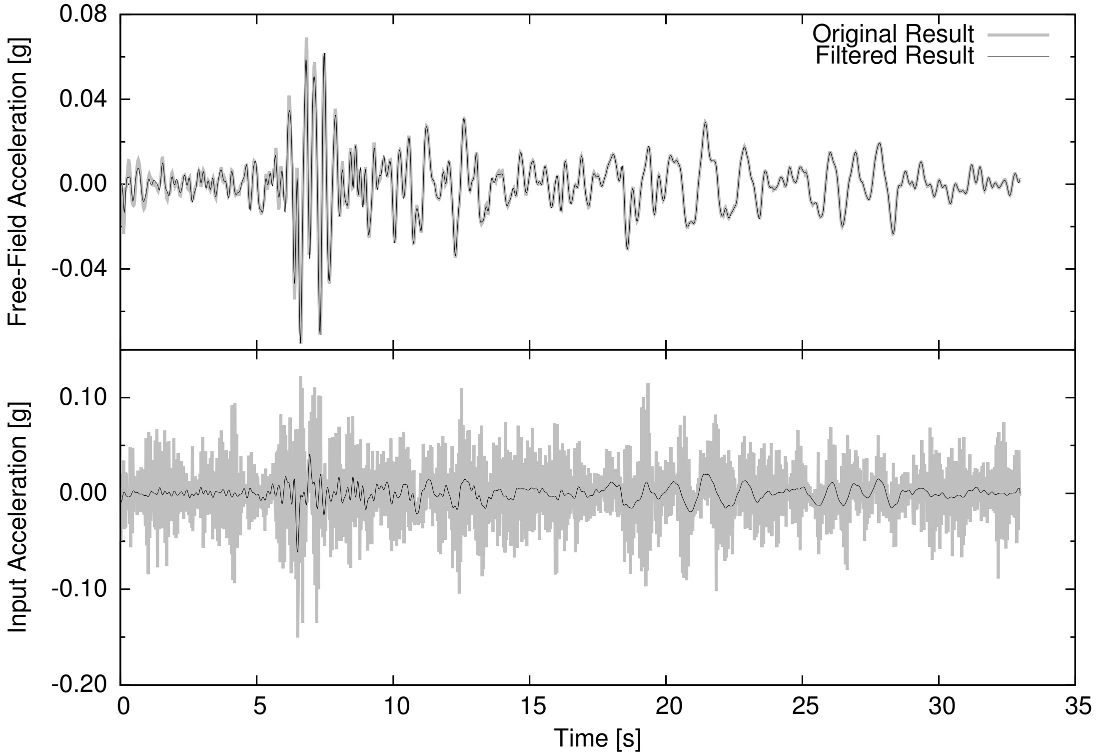

Figure C.3: Comparison of results with the original and a filtered input.

nents of the A-STP earthquake in the SMLR bin. The grey line in the top half of the figure corresponds to the free-field motion observed in the soil domain with this noisy signal. Certainly a case might be made that the accompanying input does not resemble a physical seismic event due to such high frequencies present.

Also presented in Figure C.3 is a thin, black line on the bottom half. This is what is left of the noisy input signal after a low-pass filter is applied. This filter was a butterworth filter and it had a passband frequency of 6.0 Hz, a stopband frequency of 6.5 Hz, and 80 dB of attenuation between the two. After applying the motion to the finite-element model, a very similar free-field motion was observed in the soil domain (black line in the top half of Figure C.3). The example of this figure is insightful in that it demonstrates that underneath the large amount of noise, the frequency amplitudes at the low end of the spectrum are sufficient to match the activity at the free-field level. Such a finding validates the transfer function algorithm that was used to create the input motions.

C.3.2 A Note About Discarded Motions

It was the original intention of the author to perform more earthquake event simulations on the BridgePBEE model. Originally, 100 earthquakes were slated to contribute to this investigation. It was found, however, that the input motion created by the transfer function did not always result in the desired free-field motion. An example of this is displayed in Figure C.4. Here, it is evident to the reader that a few excess frequencies were observed for the motion in the horizontal directions. For the analysis described in Chapter 5, the author removed earthquake events like this where the free-field motion observed was significantly different from what was desired and concentrated on the results where the transfer function performed well. This still left 65 motions, or about two-thirds from the original pool of motions. It was felt that this amount of earthquake events provided sufficient diversity for analyzing the structural behavior of this model.

For the reader interested in applying a similar approach for a different system, the author recommends that if unwanted frequency contents persists for a motion that absolutely must be included as part of the analysis, the algorithm might benefit from filtering the input motion that results from the transfer function. This filtered motion should then be applied to the system.

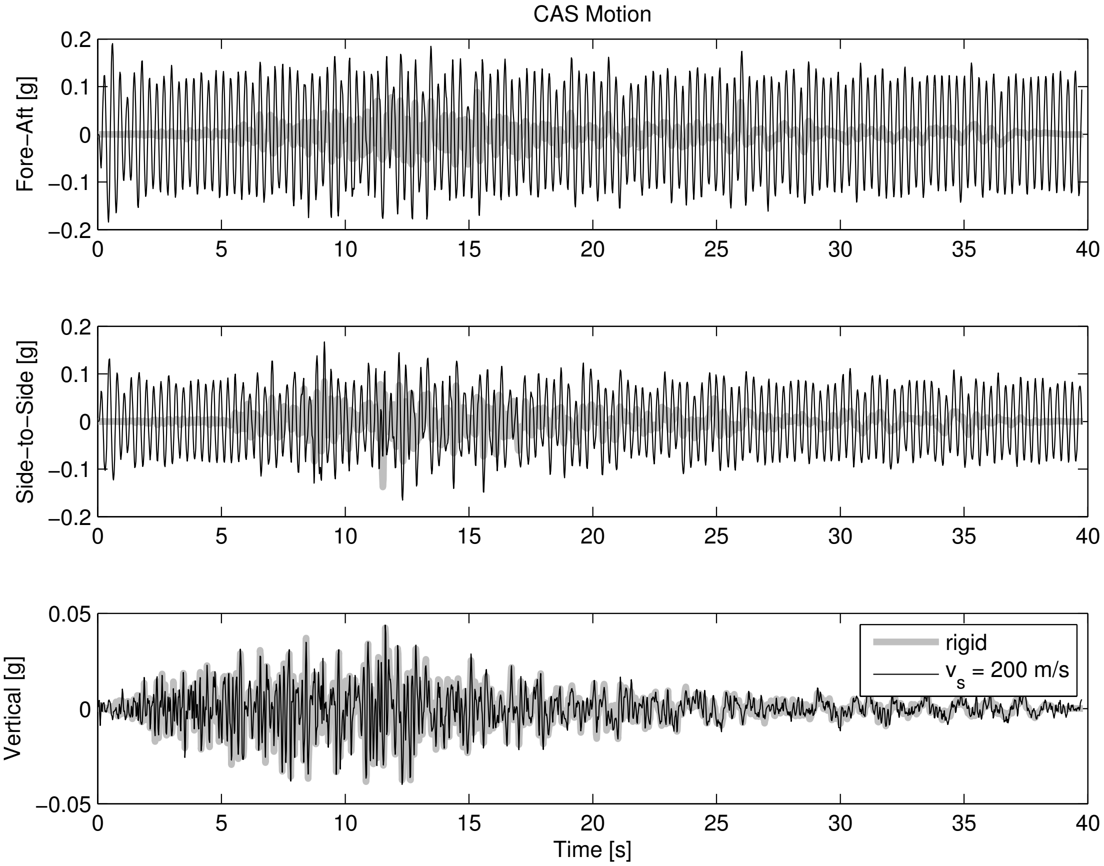

Figure C.4: An unfavorable result from the transfer function algorithm.

Bibliography

Lu, J. (2011). "BridgePBEE". `peer.berkeley.edu/bridgepbee/`. Accessed September 21, 2011.

Lu, J., Mackie, K., and Elgamal, A. (2011). *BridgePBEE Graphical User Interface OpenSees 3D Pushover and Earthquake Analysis of Single-Column 2-span Bridges, User Manual, Beta 1.0*. Pacific Earthquake Engineering Research Center, Berkeley, California, United States.

Mackie, K. R. and Stojadinović, B. (2005). "Fragility Basis for California Highway Overpass Bridge Seismic Decision Making". Technical Report 2005/02, Pacific Earthquake Engineering Research Center.